Probing Dynamic Excitations in Novel Quantum Magnets Using Raman Spectroscopy

by

Siwen Li

A dissertation submitted in partial fulfillment
of the requirements for the degree of
Doctor of Philosophy
(Physics)
in the University of Michigan
2021

Doctoral Committee:

Assistant Professor Liuyan Zhao, Chair
Assistant Professor John Heron
Professor Lu Li
Associate Professor Kai Sun
Professor Vanessa Sih

Siwen Li

lisiwen@umich.edu

ORCID iD: 0000-0002-7084-2815

Acknowledgements

I express my deep gratitude to all the people without whom this thesis would not have been possible. My advisor, Liuyan Zhao, has encouraged me to learn, think and discuss with persevering efforts through times of scientific puzzles. She is also very considerate to satisfy my personal needs, and to guide me towards a long-term goal.

Other professors have also provided great support in the fulfillment of this thesis. Kai Sun has been very helpful in our discussions and extremely patient in walking me, an experimentalist, through the theoretical calculations. Roberto Merlin has also been very thoughtful and knowledgeable in our discussions. I would like to thank our collaborators who have grown or fabricated best-quality samples, Stephen Wilson, Hechang Lei and Adam Tsen, and our collaborators who have been very helpful in data taking, Dmitry Smirnov and Rui He.

I would like to thank the group members, Wencan Jin, Hongchao Xie, Youngjun Ahn, Elizabeth Drueke, Rachel Owen, Xiangpeng Luo, and Xiaoyu Guo, with whom I have spent unforgettable times in the lab. They have worked with me in the same project, taught me on the setup alignment, or provided thoughtful ideas to my experiments. They have also dedicated to maintaining our lab without whom our lab could not have been well-operating.

Last but not least, I would like to thank my physics friends with whom I have shared many delightful memories over the years. I also owe my gratitude to my husband, Zijia, and my parents, for remotely offering help and support at every stage of my doctoral years. Zijia has always helped me through my difficulties with his broad knowledge and motivated me with his diligence.

Table of Contents

List of Tables

List of Figures

Permissions have been acquired for all the figures that are adapted from external sources.

List of Abbreviations

AFM	antiferromagnet
BFM	bulk-FM
CDW	charge density wave
CW	continuous-wave
DM	Dzyaloshinsky-Moriya
DOF	degree of freedom
DOS	density of states
FM	ferromagnet
FWHM	full width at half maximum
GS	ground state
HV	horizontal-vertical
HWP	half-wave plate
IMT	insulator metal transition
LRO	long-range order
MIT	metal insulator transition
MOKE	magneto-optical Kerr effect
MR	magnetoresistance
NA	numerical aperture

NHMFL	National High Magnetic Field Lab
NN	nearest-neighbor
PD	pseudodipolar
PM	paramagnet
QCP	quantum critical point
QPT	quantum phase transition
RIXS	Resonant inelastic X-ray scattering
RP	Ruddlesden-Popper
SAFM	surface-AFM
SC	superconductor
SOC	spin-orbit coupling
TI	topological insulator
TM	transition metal
TMO	transition metal oxide
TRS	time-reversal symmetry
VDW	van der Waals
VV	vertical-vertical
1D	1-dimensional
2D	2-dimensional
3D	3-dimensional

Abstract

Quantum materials are a class of materials where charge, orbit, spin, and lattice degrees of freedoms (DOFs) entangle to give rise to novel phases. A major subset of quantum materials, quantum magnets, span a broad spectrum including quantum dimer magnets hosting singlet ground states, pseudospin magnets with strong spin-orbit coupling (SOC), spin liquid and spin ice magnets where magnetic frustrations lead to absence of magnetic long-range order (LRO) and fractionalized excitations, 2-dimensional (2D) magnets with strong quantum fluctuations, as well as topological magnets whose magnetic order is an essential ingredient in their topological phases.

Using a combination of polarized Raman spectroscopy, an inelastic optical scattering technique, and spin-wave calculations, we study magnetic excitations in two classes of quantum magnets, namely, the bilayer perovskite iridate $Sr_3Ir_2O_7$ with strong SOC and the 2D Ising ferromagnet (FM) CrI_3 which is one of the first 2D magnets discovered.

In $Sr_3Ir_2O_7$, we discovered two sets of two-magnon modes, one of which arises from a pair of Brillouin zone-center optical magnons, and the other one from zone-boundary magnons. In particular, the former type is unconventional as it preserves the full symmetries of the underlying crystal lattice (*i.e.*, A_{1g}). Our findings not only reveal such A_{1g} magnetic excitation, but also show

the magnetic ground state (GS) of $Sr_3Ir_2O_7$ is a conventional antiferromagnet (AFM), which offers insight into the heated debate on the nature of $Sr_3Ir_2O_7$ magnetism.

In CrI_3, which has been thought to be an interlayer AFM in its few-layer form and an interlayer FM in its bulk form, we found that bulk CrI_3 in fact hosts a mixed state with interlayer AFM at its surface and interlayer FM in its deep bulk. By applying an out-of-plane magnetic field, we induced an interlayer AFM to FM phase transition at a critical field of $B_C = 2$ T, and observed a concurrent structural phase transition. Our results unambiguously address the puzzle of how the interlayer magnetism evolves upon decreasing thickness in CrI_3.

In conclusion, we used polarized Raman measurements and spin-wave calculations to study two types of quantum magnets. In the SOC magnet, $Sr_3Ir_2O_7$, we discovered a unique A_{1g} zone-center optical two-magnon excitation and confirmed its conventional AFM GS. In the bulk form of the 2D magnet, CrI_3, we uncovered a coexistence of interlayer AFM and FM, and induced concurrent magnetic and structural phase transitions with external magnetic field.

Chapter 1 Introduction

Quantum materials are a huge class of novel materials where quantum mechanics plays an essential role in their electronic or magnetic properties [1-4], as compared to traditional materials which can be described by classical or semi-classical approaches. The interplay between various DOFs, including orbital, spin, lattice, and electronic interaction, gives rise to a plethora of exotic quantum phases. Although there is no general consensus on the classification of this large material family, three major categories of quantum materials draw considerable interest, namely the strongly correlated materials, for example high-T_C cuprate [5,6] and iron [7-9] superconductors (SC), low-dimensional materials, for example graphene [10-12], and topological materials, for example topological insulators (TI) [13-16], topological semimetals [17-22] and topological magnets [23-28]. Quantum materials hold great promise in applications as they show various unusual responses under external stimulus (*e.g.*, large anomalous Hall effect [29,30] and giant nonlinear optical response [31]) and have much wider tunability than conventional materials. For the above reasons, quantum materials are at the heart of the frontier condensed matter studies in the 21st century.

Quantum magnets are an important subset of quantum materials, including the spin liquid or spin ice magnets where magnetic frustration leads to a large degeneracy in their GS and fractionalized excitations [32], dimerized magnets with entangled spin singlet GS [33,34], unconventional SOC pseudospin magnets [35], topological magnets whose time-reversal symmetry (TRS)-breaking magnetic LRO plays an essential role in their topological phases, as well as low-dimensional

magnets where quantum fluctuations play an important role [36,37]. As the starting point, understanding of the magnetic GS and corresponding low-energy excitations is crucial in further study or even application of quantum magnets. For this reason, in this thesis, we select two interesting types of quantum magnets: the perovskite iridates with SOC pseudospin moments and 2D magnets with exotic thickness-dependence. To solve the magnetic puzzles, we use a combination of Raman spectroscopy and spin-wave theory.

In contrast to the intriguing 3*d* transition metal (TM)-based systems like high-T_C cuprates and iron SC [38,39], where SOC can be treated as a perturbation, compounds with partially filled 4*d* and 5*d* orbitals have a significant SOC comparable to or even exceeding the kinetic energy, crystal field and electronic interactions. Therefore, surprisingly rich electronic and magnetic phases emerge as a result of the combined effect of SOC and electronic correlations [35,40]. For example, correlated TRS-breaking Weyl semimetal and magnetic axion insulator phases are predicted in pyrochlore iridates, such as $R_2Ir_2O_7$ [35,39,40], coexisting with complex noncollinear magnetic orders. Among the large family of heavy TM compounds, the Ruddlesden-Popper (RP) series iridate Sr_2IrO_4 and $Sr_3Ir_2O_7$ with perovskite structure have attracted great attention [41-45], mainly because Sr_2IrO_4 shows a remarkable similarity to high-T_C SC cuprates in terms of its Mott-insulating AFM GS [44,45], and even the Fermi arcs [46] and *d*-wave gap [47] in doped compounds. The strong SOC plays an essential role in the description of both magnetic and electronic GS of RP iridates, where SOC intertwines the spin and orbital DOFs and drives the valence bands into J_{eff} = 1/2 state together with Hubbard repulsion [41,42]. Moreover, distinct anisotropic magnetic exchange interactions have been proposed in perovskite iridates [48], and

novel magnetic orders have indeed been observed in RP iridates including a dimensionality-driven spin-flop transition [49] and a giant magnetic gap in $Sr_3Ir_2O_7$ [50].

To further understand the interesting magnetic excitations and the underlying exchange interactions, we performed polarized Raman spectroscopy on $Sr_3Ir_2O_7$ [51]. Through characterizing the temperature dependence and symmetry properties of the magnetic modes and utilizing spin-wave theory, we discovered an unconventional zone-center optical two-magnon excitation, which is unique to the bilayer system and shares a similar energy with the giant spin gap in RIXS spectra [50]. Our results also showed that $Sr_3Ir_2O_7$ holds a conventional AFM GS.

Magnetic LRO has been recently discovered in several 2D van der Waals (vdW) materials experimentally, including $FePS_3$ [52,53], CrI_3 [37], $Cr_2Ge_2Te_6$ [36], VSe_2 [54] and $MnSe_2$ [55], ranging from semiconducting AFM to itinerant FM. Since their discovery, they have offered an ideal playground for testing well-established theories, such as KBT theory for XY magnets [56], and realizing various exotic phases, for example quantum spin liquids [57], their wide tunability subject to pressure [58], electric field [59], gating [60] and other external stimuli provides also has promising technological and industrial value [61,62].

CrI_3 is one of the first monolayer 2D FMs and attracts great research attention [37,63-66]. In the thin flake limit, each FM layer couples AFM to the neighboring layer below its Neel temperature of 45 K, thus forming an out-of-plane interlayer AFM order [37]. However, CrI_3 shows FM order in the bulk form, with a Curie temperature of 61K [67]. To investigate this interesting thickness-dependent crossover, we use magnetic field- and temperature-dependent circularly polarized

Raman spectroscopy to study the phonon and magnon modes of bulk CrI_3 [68]. Surprisingly, we found that the bulk crystals host a mixed magnetic state with AFM existing in the surface layers and FM order dominating in the deep bulk. Additionally, a magnetic field-induced first order structural phase transition was observed with 2 T external field, accompanied with an AFM to FM transition of the top layers. Our results reveal the intriguing evolution from bulk FM to thin-film AFM and suggest the close interplay between magnetism and structure in CrI_3, opening up new possibilities for realizing new devices based on strong magnetoelastic properties.

In Chapter 2, we will introduce detailed background information on both types of magnets aforementioned. To investigate the magnetic excitations, a combination of polarized Raman spectroscopy and spin-wave calculations is used, which will be introduced in Chapter 3. Our work on the perovskite iridates will be discussed in Chapters 4 and 5, with emphases of experimental results in Chapter 4 and theoretical calculations in Chapter 5. Both the experiment and the calculations, are equally important in revealing the nature of the magnetic excitations and ground state in $Sr_3Ir_2O_7$. In Chapter 6, we will introduce our highly collaborative work on bulk CrI_3. And lastly, chapter 7 is a summary and outlook of our work.

References

[1] C. Broholm *et al.*, Basic Research Needs Workshop on Quantum Materials for Energy Relevant Technology, 2016.

[2] *The rise of quantum materials*, Nature Physics **12**, 105 (2016).

[3] B. Keimer and J. E. Moore, *The physics of quantum materials*, Nature Physics **13**, 1045 (2017).

[4] R. Cava, N. de Leon, and W. Xie, *Introduction: Quantum Materials*, Chem Rev **121**, 2777 (2021).

[5] J. G. Bednorz and K. A. Müller, *Possible high T_c superconductivity in the Ba−La−Cu−O system*, Zeitschrift für Physik B Condensed Matter **64**, 189 (1986).

[6] M.-K. Wu, J. R. Ashburn, C. Torng, P. H. Hor, R. L. Meng, L. Gao, Z. J. Huang, Y. Wang, and a. Chu, *Superconductivity at 93 K in a new mixed-phase Y-Ba-Cu-O compound system at ambient pressure*, Physical review letters **58**, 908 (1987).

[7] X. Chen, T. Wu, G. Wu, R. Liu, H. Chen, and D. Fang, *Superconductivity at 43 K in $SmFeAsO_{1-x}F_x$*, nature **453**, 761 (2008).

[8] Y. Kamihara, H. Hiramatsu, M. Hirano, R. Kawamura, H. Yanagi, T. Kamiya, and H. Hosono, *Iron-based layered superconductor: LaOFeP*, Journal of the American Chemical Society **128**, 10012 (2006).

[9] M. Rotter, M. Tegel, and D. Johrendt, *Superconductivity at 38 K in the iron arsenide $(Ba_{1-x}K_x)Fe_2As_2$*, Physical Review Letters **101**, 107006 (2008).

[10] K. S. Novoselov, A. K. Geim, S. V. Morozov, D. Jiang, Y. Zhang, S. V. Dubonos, I. V. Grigorieva, and A. A. Firsov, *Electric field effect in atomically thin carbon films*, science **306**, 666 (2004).

[11] A. H. Castro Neto, F. Guinea, N. M. R. Peres, K. S. Novoselov, and A. K. Geim, *The electronic properties of graphene*, Reviews of modern physics **81**, 109 (2009).

[12] A. K. Geim and K. S. Novoselov, in *Nanoscience and technology: a collection of reviews from nature journals* (World Scientific, 2010), pp. 11.

[13] D. Hsieh, D. Qian, L. Wray, Y. Xia, Y. S. Hor, R. J. Cava, and M. Z. Hasan, *A topological Dirac insulator in a quantum spin Hall phase*, Nature **452**, 970 (2008).

[14] Y. Chen *et al.*, *Experimental realization of a three-dimensional topological insulator, Bi_2Te_3*, science **325**, 178 (2009).

[15] D. Hsieh *et al.*, *A tunable topological insulator in the spin helical Dirac transport regime*, Nature **460**, 1101 (2009).

[16] S.-Y. Xu *et al.*, *Topological phase transition and texture inversion in a tunable topological insulator*, Science **332**, 560 (2011).

[17] S. Borisenko, Q. Gibson, D. Evtushinsky, V. Zabolotnyy, B. Büchner, and R. J. Cava, *Experimental realization of a three-dimensional Dirac semimetal*, Physical review letters **113**, 027603 (2014).

[18] Z. Liu *et al.*, *Discovery of a three-dimensional topological Dirac semimetal, Na_3Bi*, Science **343**, 864 (2014).

[19] S.-Y. Xu *et al.*, *Observation of Fermi arc surface states in a topological metal*, Science **347**, 294 (2015).

[20] S.-Y. Xu *et al.*, *Discovery of a Weyl fermion semimetal and topological Fermi arcs*, Science **349**, 613 (2015).

[21] B. Lv *et al.*, *Experimental discovery of Weyl semimetal TaAs*, Physical Review X **5**, 031013 (2015).

[22] G. Chang *et al.*, *Topological Chiral Semimetal: Theory and Experiments*, Bulletin of the American Physical Society (2021).

[23] C.-Z. Chang *et al.*, *Experimental observation of the quantum anomalous Hall effect in a magnetic topological insulator*, Science **340**, 167 (2013).

[24] L. Ye *et al.*, *Massive Dirac fermions in a ferromagnetic kagome metal*, Nature **555**, 638 (2018).

[25] D. Liu *et al.*, *Magnetic Weyl semimetal phase in a Kagomé crystal*, Science **365**, 1282 (2019).

[26] I. Belopolski *et al.*, *Discovery of topological Weyl fermion lines and drumhead surface states in a room temperature magnet*, Science **365**, 1278 (2019).

[27] J.-X. Yin *et al.*, *Quantum-limit Chern topological magnetism in* $TbMn_6Sn_6$, Nature **583**, 533 (2020).

[28] Y. Deng, Y. Yu, M. Z. Shi, Z. Guo, Z. Xu, J. Wang, X. H. Chen, and Y. Zhang, *Quantum anomalous Hall effect in intrinsic magnetic topological insulator* $MnBi_2Te_4$, Science **367**, 895 (2020).

[29] E. Liu *et al.*, *Giant anomalous Hall effect in a ferromagnetic kagome-lattice semimetal*, Nature physics **14**, 1125 (2018).

[30] S. Nakatsuji, N. Kiyohara, and T. Higo, *Large anomalous Hall effect in a non-collinear antiferromagnet at room temperature*, Nature **527**, 212 (2015).

[31] L. Wu, S. Patankar, T. Morimoto, N. L. Nair, E. Thewalt, A. Little, J. G. Analytis, J. E. Moore, and J. Orenstein, *Giant anisotropic nonlinear optical response in transition metal monopnictide Weyl semimetals*, Nature Physics **13**, 350 (2017).

[32] L. Balents, *Spin liquids in frustrated magnets*, Nature **464**, 199 (2010).

[33] T. Giamarchi, C. Rüegg, and O. Tchernyshyov, *Bose–Einstein condensation in magnetic insulators*, Nature Physics **4**, 198 (2008).

[34] V. Zapf, M. Jaime, and C. D. Batista, *Bose-Einstein condensation in quantum magnets*, Reviews of Modern Physics **86**, 563 (2014).

[35] J. G. Rau, E. K.-H. Lee, and H.-Y. Kee, *Spin-orbit physics giving rise to novel phases in correlated systems: Iridates and related materials*, Annual Review of Condensed Matter Physics **7**, 195 (2016).

[36] C. Gong *et al.*, *Discovery of intrinsic ferromagnetism in two-dimensional van der Waals crystals*, Nature **546**, 265 (2017).

[37] B. Huang *et al.*, *Layer-dependent ferromagnetism in a van der Waals crystal down to the monolayer limit*, Nature **546**, 270 (2017).

[38] J. A. Sobota, Y. He, and Z.-X. Shen, *Angle-resolved photoemission studies of quantum materials*, Reviews of Modern Physics **93**, 025006 (2021).

[39] A. Damascelli, Z. Hussain, and Z.-X. Shen, *Angle-resolved photoemission studies of the cuprate superconductors*, Reviews of modern physics **75**, 473 (2003).

[40] W. Witczak-Krempa, G. Chen, Y. B. Kim, and L. Balents, *Correlated quantum phenomena in the strong spin-orbit regime*, Annu. Rev. Condens. Matter Phys. **5**, 57 (2014).

[41] B. Kim *et al.*, *Novel J_{eff} = 1/2 Mott state induced by relativistic spin-orbit coupling in Sr_2IrO_4*, Physical review letters **101**, 076402 (2008).

[42] S. Moon *et al.*, *Dimensionality-Controlled Insulator-Metal Transition and Correlated Metallic State in 5d Transition Metal Oxides $Sr_{n+1}Ir_nO_{3n+1}$ (n= 1, 2, and ∞)*, Physical review letters **101**, 226402 (2008).

[43] B. Kim, H. Ohsumi, T. Komesu, S. Sakai, T. Morita, H. Takagi, and T.-h. Arima, *Phase-sensitive observation of a spin-orbital Mott state in Sr_2IrO_4*, Science **323**, 1329 (2009).

[44] S. Fujiyama, H. Ohsumi, T. Komesu, J. Matsuno, B. J. Kim, M. Takata, T. Arima, and H. Takagi, *Two-dimensional Heisenberg behavior of J(eff)=1/2 isospins in the paramagnetic state of the spin-orbital Mott insulator Sr2IrO4*, Phys Rev Lett **108**, 247212 (2012).

[45] J. Kim *et al.*, *Magnetic excitation spectra of Sr_2IrO_4 probed by resonant inelastic x-ray scattering: establishing links to cuprate superconductors*, Phys Rev Lett **108**, 177003 (2012).

[46] Y. K. Kim, O. Krupin, J. Denlinger, A. Bostwick, E. Rotenberg, Q. Zhao, J. Mitchell, J. Allen, and B. Kim, *Fermi arcs in a doped pseudospin-1/2 Heisenberg antiferromagnet*, Science **345**, 187 (2014).

[47] Y. K. Kim, N. Sung, J. Denlinger, and B. Kim, *Observation of ad-wave gap in electron-doped Sr_2IrO_4*, Nature Physics **12**, 37 (2016).

[48] G. Jackeli and G. Khaliullin, *Mott insulators in the strong spin-orbit coupling limit: from Heisenberg to a quantum compass and Kitaev models*, Phys Rev Lett **102**, 017205 (2009).

[49] J. Kim, Y. Choi, J. Kim, J. Mitchell, G. Jackeli, M. Daghofer, J. Van Den Brink, G. Khaliullin, and B. Kim, *Dimensionality driven spin-flop transition in layered iridates*, Physical review letters **109**, 037204 (2012).

[50] J. Kim *et al.*, *Large Spin-Wave Energy Gap in the Bilayer Iridate $Sr_3Ir_2O_7$: Evidence for Enhanced Dipolar Interactions Near the Mott Metal-Insulator Transition*, Physical Review Letters **109** (2012).

[51] S. Li *et al.*, *Symmetry-resolved two-magnon excitations in a strong spin-orbit-coupled bilayer antiferromagnet*, Physical Review Letters **125**, 087202 (2020).

[52] J.-U. Lee, S. Lee, J. H. Ryoo, S. Kang, T. Y. Kim, P. Kim, C.-H. Park, J.-G. Park, and H. Cheong, *Ising-type magnetic ordering in atomically thin $FePS_3$*, Nano letters **16**, 7433 (2016).

[53] X. Wang *et al.*, *Raman spectroscopy of atomically thin two-dimensional magnetic iron phosphorus trisulfide ($FePS_3$) crystals*, 2D Materials **3**, 031009 (2016).

[54] M. Bonilla *et al.*, *Strong room-temperature ferromagnetism in VSe_2 monolayers on van der Waals substrates*, Nature nanotechnology **13**, 289 (2018).

[55] D. J. O'Hara *et al.*, *Room temperature intrinsic ferromagnetism in epitaxial manganese selenide films in the monolayer limit*, Nano letters **18**, 3125 (2018).

[56] J. M. Kosterlitz and D. J. Thouless, *Ordering, metastability and phase transitions in two-dimensional systems*, Journal of Physics C: Solid State Physics **6**, 1181 (1973).

[57] A. Banerjee *et al.*, *Neutron scattering in the proximate quantum spin liquid α-$RuCl_3$*, Science **356**, 1055 (2017).

[58] Z. Lin *et al.*, *Pressure-induced spin reorientation transition in layered ferromagnetic insulator $Cr_2Ge_2Te_6$*, Physical Review Materials **2**, 051004 (2018).

[59] S. Jiang, J. Shan, and K. F. Mak, *Electric-field switching of two-dimensional van der Waals magnets*, Nature materials **17**, 406 (2018).

[60] Z. Wang *et al.*, *Electric-field control of magnetism in a few-layered van der Waals ferromagnetic semiconductor*, Nature nanotechnology **13**, 554 (2018).

[61] D. Sander *et al.*, *The 2017 magnetism roadmap*, Journal of Physics D: Applied Physics **50**, 363001 (2017).

[62] K. S. Burch, D. Mandrus, and J.-G. Park, *Magnetism in two-dimensional van der Waals materials*, Nature **563**, 47 (2018).

[63] D. R. Klein *et al.*, *Probing magnetism in 2D van der Waals crystalline insulators via electron tunneling*, Science **360**, 1218 (2018).

[64] T. Song *et al.*, *Giant tunneling magnetoresistance in spin-filter van der Waals heterostructures*, Science **360**, 1214 (2018).

[65] H. H. Kim, B. Yang, T. Patel, F. Sfigakis, C. Li, S. Tian, H. Lei, and A. W. Tsen, *One million percent tunnel magnetoresistance in a magnetic van der Waals heterostructure*, Nano letters **18**, 4885 (2018).

[66] Z. Wang *et al.*, *Very large tunneling magnetoresistance in layered magnetic semiconductor* CrI_3, Nature communications **9**, 1 (2018).

[67] M. A. McGuire, H. Dixit, V. R. Cooper, and B. C. Sales, *Coupling of Crystal Structure and Magnetism in the Layered, Ferromagnetic Insulator* CrI_3, Chemistry of Materials **27**, 612 (2015).

[68] S. Li *et al.*, *Magnetic-field-induced quantum phase transitions in a van der Waals magnet*, Physical Review X **10**, 011075 (2020).

Chapter 2 Background

Starting from the usage of loadstone in navigation, magnetism has played an essential role in both academy and technology for more than a thousand years. Despite the long history of application and study, only until 20th century people have started to realize that the magnetic order in various magnets is a fully quantum mechanical phenomenon. Van Leeuwen stated in 1918 that without assuming a finite magnetic moment on each atom, classical Boltzman statistics applied to any dynamical system cannot produce either a susceptibility or a magnetic moment [2]. The required finite magnetic moment, either comes from the orbiting electron or spin, thus originates from quantized orbital or spin angular momentum.

Under the assumption of finite magnetic momentum, magnets can be divided into two main categories: classical magnets and quantum magnets. Semiclassical approach is sufficient to explain the collective behavior of the magnetic moments in classical magnets, while a full quantum description involving various DOFs is necessary for quantum magnets. Consequently, the key questions for understanding quantum magnets are: how do these DOFs interplay with one another in forming various exotic magnetic orders and which factors are the most important?

In this chapter, by introducing previous studies on two important class of quantum magnets, perovskite iridates and 2D vdW magnets, we aim to present the intriguing interplay between SOC,

correlation, dimension and magnetic anisotropy in quantum magnets, with particular emphasis of SOC and correlation in perovskite iridates, and dimension and magnetic anisotropy in 2D magnets.

2.1 Phase diagram of high-T_C cuprate SC

In this section, we will first briefly summarize the phases in high-T_C cuprates, which is intimately related to the perovskite iridates and serves as an model system to study strongly correlated Mott system. The concept of strongly correlated systems has been introduced for describing phases where canonical Laudau quasiparticle description fails to capture the essential physics properties. One classical example is high-T_C copper-based SC, or cuprates, which own a rich phase diagram with different doping levels and temperatures (Figure 2.1).

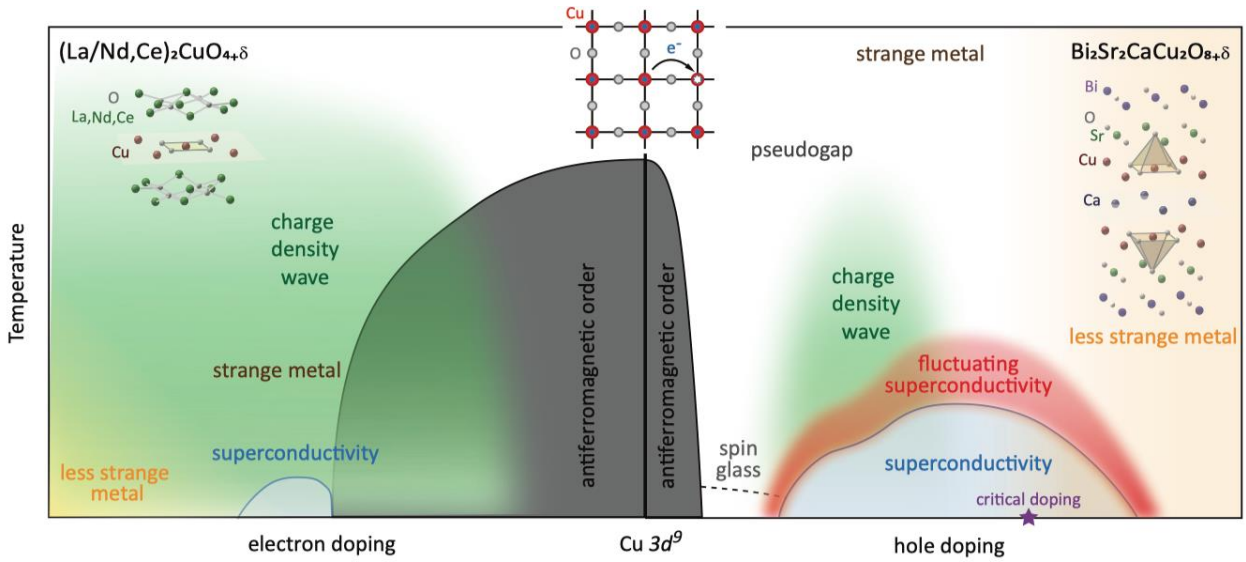

Figure 2.1 Schematic temperature-doping phase diagram of electron- and hole-doped cuprate SC, adapted from Reference [1] with permission.

As a single-band system, the low-energy electronic states of cuprates are dominated by Cu 3*d* orbitals. Although simple band-filling argument suggests a metallic ground state, the strong onsite electron-electron Coulomb interaction drives undoped cuprates into a correlated Mott insulating state with AFM LRO below its Neel temperature [4,5]. The charge localization of the insulating phase can be alleviated by electron/hole doping, which gives rise to a plethora of exotic phases. Dome-shape unconventional *d*-wave superconductivity phase shows up with both electron doping and hole doping [6], after the AFM LRO being destroyed with excessive carriers. A spin glass phase characterized by slow spin dynamics [7], charge density wave (CDW) order and spin stripes [8,9] and coherent normal metallic state [10] can also be induced by gradually increasing hole doping level. The strong electronic interaction in cuprates also manifests itself through emergent phases with elevated temperature, especially the strange metal phase [11,12], which appears above the superconducting transition temperature and below critical doping and featured with anomalous linear resistivity [13] and large self-energy correction in the spectrum [14].

2.2 J_{eff} = 1/2 pseudospins in Mott-insulating Sr_2IrO_4 and $Sr_3Ir_2O_7$

As we move from 3*d* to 5*d* TM on the periodic table, the electron orbitals become more extended so that the local Hubbard repulsion U is reduced. On the other hand, the relativistic SOC effect which increases with the larger atomic number becomes significant in 5*d* TM compounds. The competing interactions can result in a plethora of novel phases, as shown in Figure 2.2, which is plotted in terms of the relative strength of U/t and λ/t, where λ is the SOC strength and t is the hopping energy. When U is much larger than the band width t, we enter the Mott insulator regime where metal-insulator transition (MIT) occurs along with AFM order due to the strong electron-

electron interaction. Typical example includes the high-temperature superconductor $La_{2-x}Ba_xCuO_4$ [15]. When λ becomes the dominating energy scale, band inversion can happen in certain metal and semiconductor, and drive them into TI or topological semimetal state, for example the TI $Bi_{1-x}Sb_x$ [16]. In the intermediate region where both U and λ are non-negligible, SOC leads to the splittings of the bands and effectively decreasing the kinetic energy t. As a result, only a relatively smaller U is necessary to induce a Mott-insulating phase, and thus U and λ cooperate in creating a SOC Mott insulator.

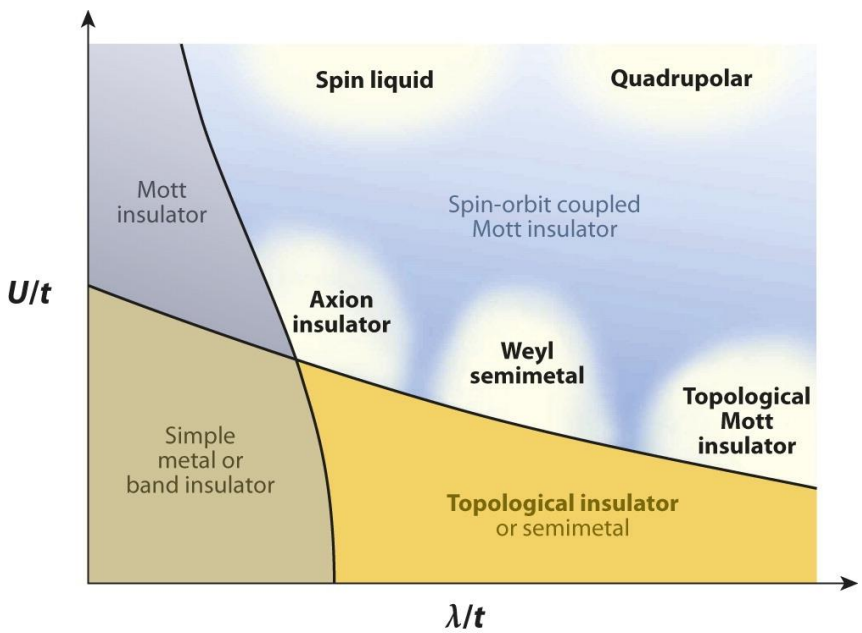

Figure 2.2 Schematic phase diagram in terms of *U*/*t* and *λ*/*t* adapted from Reference [17] with permission.

In this interesting intermediate region of SOC Mott insulators, several transition metal oxides (TMO) have been experimentally observed to show insulating behavior despite partially filled 5*d* bands in band structure calculation, including iridium oxides [3,18-36] and osmium oxides [37,38].

Iridium oxides, or iridates, are a large family of TMOs that display a range of emergent phases in this SOC Mott-insulating region. Optical data on Ir^{4+} suggest a high value of the SOC λ ~380 meV [39], which is large enough to lock the orbit and spin angular momentum locally and thus total angular momentum becomes a well-defined quantum number in describing the band structure. Among the large family of iridates, the hexagonal insulators $(Na/Li)_2IrO_3$ have been shown to possess an AFM Mott-insulating GS [25,27] and their magnetic GS hold the potential for realizing quantum spin liquids [26,30]. The pyrochlore iridate $R_2Ir_2O_7$ shows an MIT and unconventional magnetic instability [32,33,36]. The spinel structure iridate $Na_4Ir_3O_8$ is theoretically predicted to be a candidate for spin liquid [34].

We are particularly interested in the RP series of perovskite iridates $Sr_{n+1}Ir_nO_{3n+1}$ (n = 1, 2, ∞). This family of iridates has drawn considerable interest because its single-layer compound Sr_2IrO_4 shows strong similarity to the high-T_C cuprate SC in terms of Mottness and electronic structure, and efforts have been made in searching for SC in doped Sr_2IrO_4, despite so far no direct evidence of SC has been found.

To understand the role of SOC and interaction in $Sr_{n+1}Ir_nO_{3n+1}$ family, here we summarize the current consensus on the electronic and spin structure of Sr_2IrO_4 and $Sr_3Ir_2O_7$. The octahedral crystal field potential splits the states of the Ir *d*-electrons into an e_g doublet and a t_{2g} triplet, with t_{2g} states being the lower-energy states (Figure 2.3 b). The d^5 configuration of Ir^{4+} is thus equivalent to a hole in the t_{2g} states. SOC further splits the t_{2g} multiplet into J_{eff} = 1/2 doublet and J_{eff} = 3/2 quartet as shown in Figure 2.3 c. Simple electron counting leads to fully occupied low-energy J_{eff} = 3/2 states and a half-filled J_{eff} = 1/2 state.

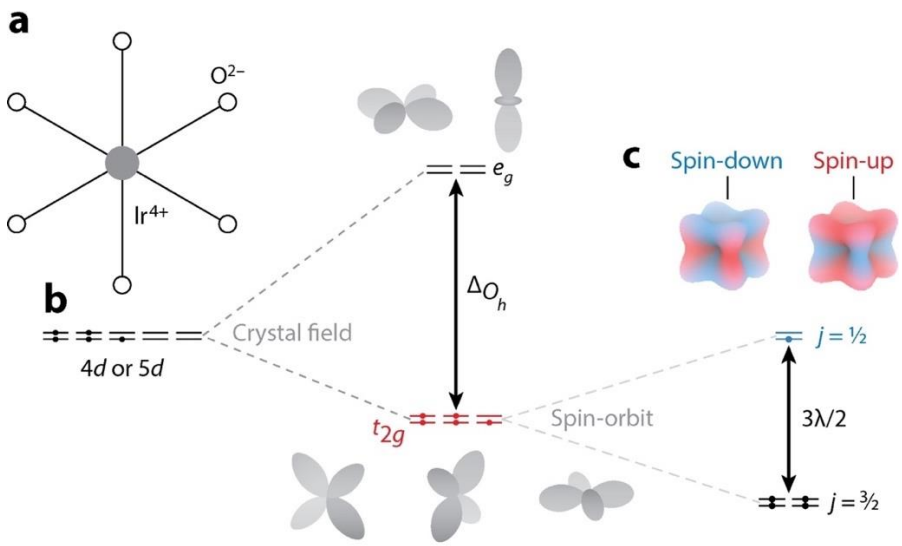

Figure 2.3 (a) The octahedral crystal field of Ir^{4+}, (b) crystal field splitting of the d^5 states into the t_{2g}^5 states, and (c) SOC induced J_{eff} = 1/2 doublet and J_{eff} = 3/2 quartet. This figure is adapted from Reference [40] with permission.

The t_{2g} orbital states have effective angular momentum of l = 1 [41]. They can be written with basis of the *xy*, *xz*, and *yz* orbitals.

$$|l_z = 0\rangle = |xy\rangle$$
$$|l_z = \pm 1\rangle = -\frac{1}{\sqrt{2}}(i|xz\rangle \pm |yz\rangle) \tag{2.1}$$

Considering the SOC, the single-ion Hamiltonian becomes [42]

$$H_0 = \lambda \vec{l} \cdot \vec{s} + \Delta l_z^2 \tag{2.2}$$

Δ is the tetragonal splitting term. The lowest energy level J_{eff} = 1/2 states are

$$\left|J_{eff} = +\frac{1}{2}\right\rangle = \sin\theta\,|0,\uparrow\rangle - \cos\theta\,|+1,\downarrow\rangle$$
$$\left|J_{eff} = -\frac{1}{2}\right\rangle = \sin\theta\,|0,\downarrow\rangle - \cos\theta\,|-1,\uparrow\rangle \tag{2.3}$$

where the first parameter 0, ± 1 denote l_z of the orbital angular momentum, and $\uparrow, \downarrow$ denote the z-component of the spin angular momentum. θ is determined by the relative strength of SOC and the tetragonal splitting energies, where $\tan 2\theta = 2\sqrt{2}\lambda/(\lambda - 2\Delta)$.

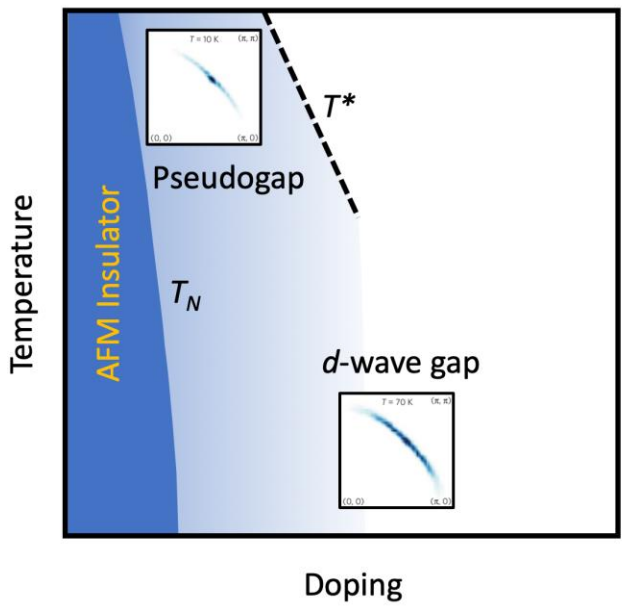

Figure 2.4 A schematic temperature versus electron-doping phase diagram of Sr_2IrO_4, based on Reference [43,44].

Although the on-site Hubbard repulsion U is relatively small in iridates, it is sufficient to split the $J_{eff} = 1/2$ band, driving Sr_2IrO_4 and $Sr_3Ir_2O_7$ into SOC-induced Mott insulators [45]. Sr_2IrO_4 **s**hows interesting similarity to the high-T_C SC cuprate La_2CuO_4, both of which show AFM insulating GS with comparable exchange interactions on the order of J ~100 meV [20,21], and charge gaps much larger than J. Efforts have been made searching for SC in doped Sr_2IrO_4, with discoveries of Fermi arcs [44] and d-wave gap [43] analog to doped cuprates (Figure 2.4). Although SC has been predicted theoretically in this d-wave gap region [46], no SC behavior has been observed

experimentally so far. Figure 2.5 shows the temperature versus La-doping phase diagram of $(Sr_{1-x}La_x)_3Ir_2O_7$. Our study is focused on the insulating AFM region of both compounds.

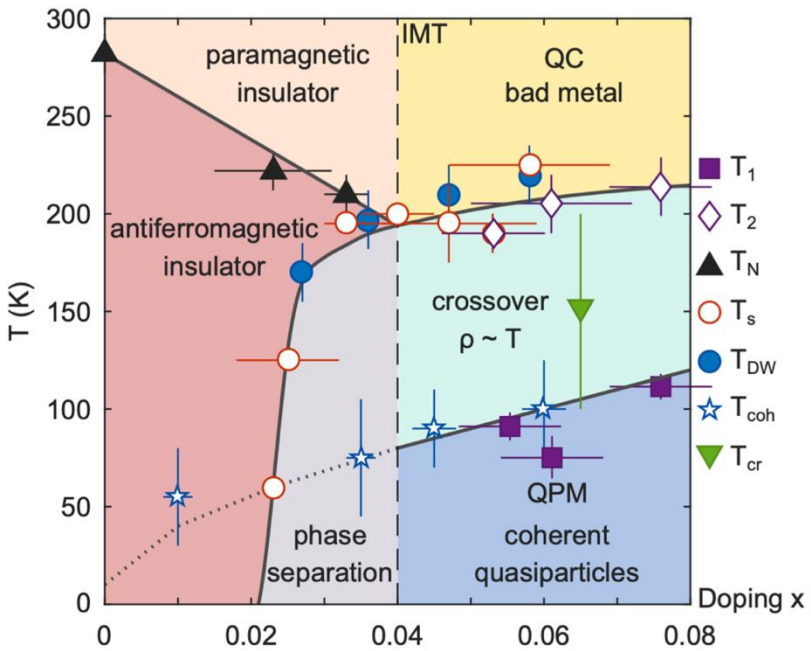

Figure 2.5 Temperature versus La-doping phase diagram of $(Sr_{1-x}La_x)_3Ir_2O_7$ summarizing experiments with various techniques, adapted from Reference [47] with permission. The Neel temperature T_N and the structural phase transition temperature T_s are acquired with neutron powder diffraction [48]. T_{DW} marks the onset temperature of a possible CDW instability from pump probe optical reflectivity [49]. T_{cr} is the crossover temperature from resonant elastic X-ray scattering [50]. T_{coh} cooresponds to loss of coherent spectral weight by angle-resolved photoelectron spectroscopy [51]. T_1 (T_2) marks the onset (end) of constant $d\rho/dT$ [48,52].

Unlike the isotropic spin exchange interactions that dominate in cuprates, the 3D density profile of the J_{eff} = 1/2 pseudospins (the top panel of Figure 2.3 c and Figure 2.6) in iridates results in additional anisotropic magnetic interactions including the Dzyaloshinsky-Moriya (DM) and

pseudodipolar (PD) interactions [42]. In Chapter 3, we will discuss in more detail on the form of the magnetic interactions of the J_{eff} = 1/2 pseudospins. As a result, novel magnetic GSs emerge including the large in-plane net magnetic moment in Sr_2IrO_4 [42,53], and the transition from in-plane magnetic moments in Sr_2IrO_4 to out-of-plane magnetic moments in $Sr_3Ir_2O_7$ [22].

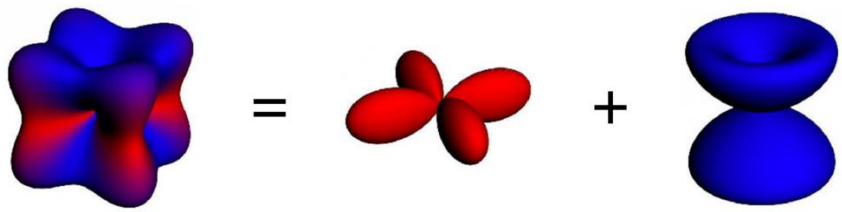

Figure 2.6 The spatial distribution of $J_{eff,z}$ = + 1/2 state as a superposition of S_z = + 1/2, L_z = 0 state, and S_z = - 1/2, L_z = + 1 state. The color red and blue represent spins up and down. This figure is adapted from Reference [42] with permission.

2.3 Resonant inelastic X-ray scattering of magnetism in Sr_2IrO_4 and $Sr_3Ir_2O_7$

Resonant inelastic X-ray scattering (RIXS) studies of Sr_2IrO_4 revealed a gapless magnon band (the blue dots in Figure 2.7) [21]. This magnon dispersion is well described with spin wave theory of an isotropic Heisenberg AFM (the purple line in Figure 2.7), similar to La_2CuO_4 [21].

$Sr_3Ir_2O_7$, on the contrary, displays a large magnetic gap ~92 meV (Figure 2.8) [3,54]. The nature of this gap has been on a debate regarding the dominating magnetic interactions in bilayer $Sr_3Ir_2O_7$. Two distinct models have been proposed to explain the giant magnon gap. The first model assumes the GS is a traditional bilayer AFM, and the magnetic branch B in the RIXS data is attributed to

degenerate acoustic and optical single-magnon excitations (Figure 2.8 b: theoretical fittings, and Figure 2.9 a: a schematic illustration). The gap is due to a large interlayer PD interaction [3,50].

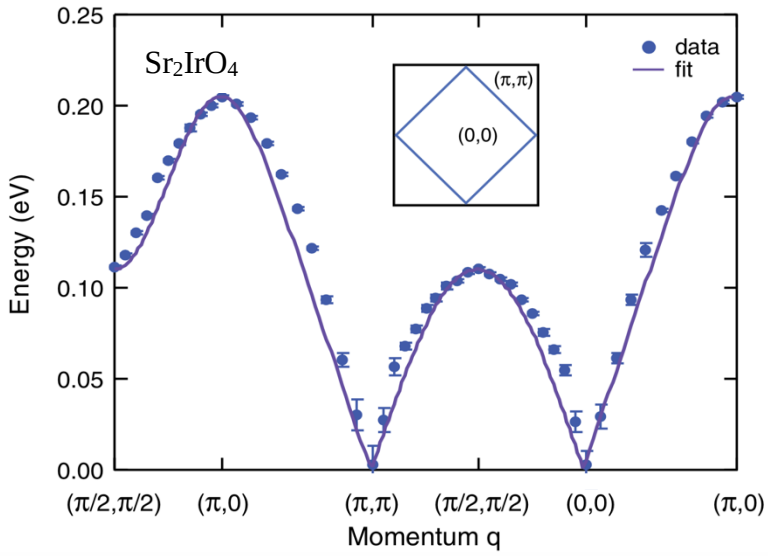

Figure 2.7 RIXS data of the magnon dispersion in Sr_2IrO_4 (blue dots) and spin wave fitting of Heisenberg AFM model (purple line), adapted from Reference [21] with permission.

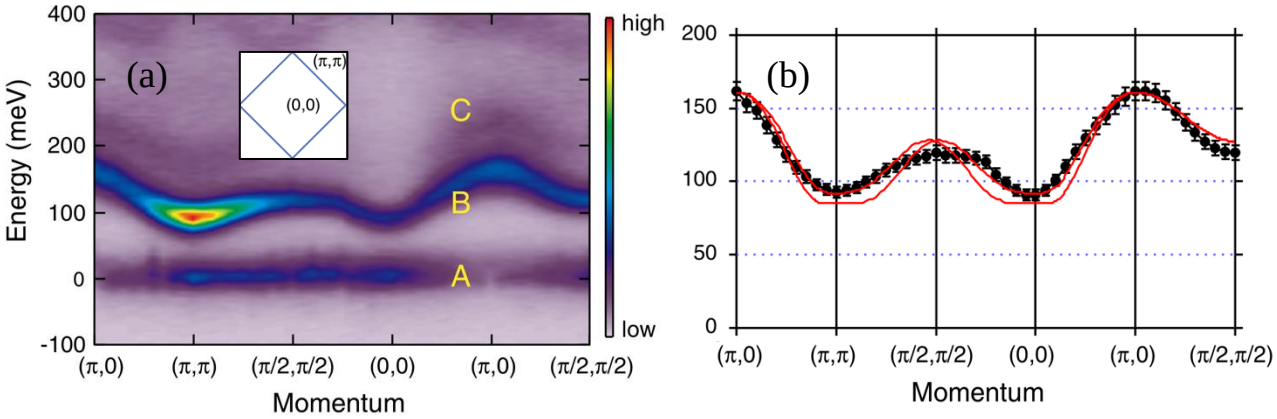

Figure 2.8 (a) RIXS data of magnetic excitations in $Sr_3Ir_2O_7$ that are composed of three dispersive features: A is the elastic scattering branch, B is the magnetic branch whose origin is on debate, and C is the multi-magnon branch. (b) Fitting of feature B assuming two degenerate acoustic and optical single-magnon branches. This figure is adapted from Reference [3] with permission.

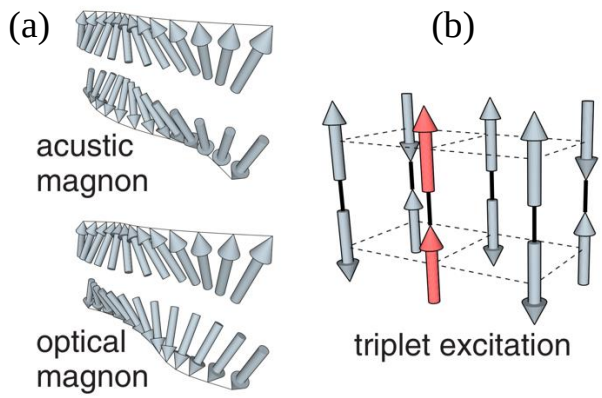

Figure 2.9 Schematic illustration of the two theories of the magnetic excitation discovered in $Sr_3Ir_2O_7$, which are (a) the spin wave picture, and (b) the dimer triplet picture. This figure is adapted from [54] with permission.

Because feature B shows moderate dispersion throughout the entire Brillouin zone, the second model assumes that the GS is the quantum dimer state formed by the adjacent spins from two layers because of a large interlayer coupling [54,55]. The gap corresponds to the dimer triplet excitation (Figure 2.9 b) and the moderate dispersion is due to the localized nature of the dimers. Either explanation assumes that bilayer $Sr_3Ir_2O_7$ holds special anisotropies that differ drastically from single-layer Sr_2IrO_4 or cuprates.

To provide more insight into the nature of this gap, we use a combination of polarized Raman spectroscopy and spin wave calculations, which will be introduced in Chapter 3, to probe an excitation with the same energy as the 92 meV magnetic gap. Polarized Raman spectroscopy provides much higher energy resolution and additional symmetry resolution compared to RIXS, which is crucial in determining the nature of the magnon gap. Combined with spin wave calculations, our study shows that the gap is not a single magnon excitation as the previous studies

suggested, but rather a two-magnon process. More importantly, our model requires minimal anisotropy in bilayer $Sr_3Ir_2O_7$ suggesting its similarity to its single layer counterpart Sr_2IrO_4.

2.4 Mermin-Wagner theorem

Since the discovery of graphene in 2004 [56], a wide range of 2D materials have been discovered which display various electronic properties. The existence of 2D magnet has been studied both theoretically and experimentally. In this section, we introduce the Mermin-Wagner theorem which imposes constraints on the magnetic order in low dimensions, which provides guidance in the search of the layered magnets that hold magnetic LRO down to the monolayer limit.

Mermin and Wagner proved in their paper in 1966 that AFM or FM order does not exist in 1-dimensional (1D) or 2D isotropic Heisenberg model with finite-range exchange interaction at any finite temperature [57]. Let us prove a subset of Mermin-Wagner theorem in an alternate form: thermal fluctuations will destroy FM LRO in 2D isotropic Heisenberg model.

Consider the isotropic Heisenberg model with FM exchange interaction

$$H_{HFM} = -J \sum_{<i,j>} \vec{S}_i \cdot \vec{S}_j \tag{2.4}$$

where $<i, j>$ sums over the nearest-neighbor spin products, J is the exchange interaction, $\vec{S}_i$ is the spin vector on site i. In the case of FM Heisenberg model, the overall negative sign combined with a positive J favors the spins to be parallel to each other to lower the GS energy.

Using Holstein-Primakoff transformations in the $\vec{k}$-space which will be discussed in detail in Section 3.6 [58],

$$\begin{aligned} S_i^+ &= S_i^x + iS_i^y = \sqrt{\frac{2S}{N}} \sum_{\vec{k}} a_{\vec{k}} e^{i\vec{k}\cdot\vec{r}_i} \\ S_i^- &= S_i^x - iS_i^y = \sqrt{\frac{2S}{N}} \sum_{\vec{k}} a_{\vec{k}}^+ e^{-i\vec{k}\cdot\vec{r}_i} \\ S_i^z &= S - \frac{1}{N} \sum_{\vec{k},\vec{k}'} a_{\vec{k}}^+ a_{\vec{k}'} e^{i(\vec{k}'-\vec{k})\cdot\vec{r}_i} \end{aligned} \tag{2.5}$$

the FM Heisenberg Hamiltonian in Equation 2.7 can be diagonalized to

$$H_{HFM} = \sum_{\vec{k}} E_{\vec{k}} a_{\vec{k}}^+ a_{\vec{k}} \tag{2.6}$$

where

$$E_{\vec{k}}^{HFM} = JSZ\left(1 - \gamma_{\vec{k}}\right) \tag{2.7}$$

$$\gamma_{\vec{k}} = \frac{1}{Z} \sum_{<j>} e^{i\vec{k}\cdot(\vec{r}_i - \vec{r}_j)} \tag{2.8}$$

Equations 2.7 and 2.8 give the spin wave dispersion relations. Near the Brillouin-zone center where $\vec{k} \to 0$, the spin energy is quadratic in wave vector $E_{\vec{k}} \sim k^2$, the 2D density of states (DOS) per unit volume $N(E)$ is thus a constant

$$N(E)dE = \frac{kdk}{(2\pi)^2} \sim d(k^2) \sim dE \tag{2.9}$$

The thermal occupation of spin waves causes a reduction in the magnetization

$$\Delta M \sim \int_0^\infty dE \frac{1}{e^{\frac{E}{k_B T}} - 1} \to \infty \tag{2.10}$$

This integral diverges which means that the reduction in magnetization is sufficient to destroy any 2D magnetic order at a finite temperature.

If we consider anisotropic Ising FM,

$$H_{IFM} = -J_{xy} \sum_{<i,j>} (S_i^x S_j^x + S_i^y S_j^y) - J_z \sum_{<i,j>} S_i^z S_j^z \tag{2.11}$$

the spin wave spectrum becomes gapped whose energy gap is determined by the z-axis anisotropy

$$E_{\vec{k}}^{IFM} = \left(J_z - J_{xy}\gamma_{\vec{k}}\right)SZ \tag{2.12}$$

Because of this energy gap, the lower bound of the integral in Equation 2.10 is no longer 0, so that ΔM becomes a finite value. Rigorous proof of the existence of 2D Ising FM can be found in Reference [59].

2.5 Introduction of 2D magnets

Historically, the attempts to experimentally realize 2D magnetic order started since the successful growth of epitaxial thin film and superlattices. The giant magnetoresistance (MR), for instance, was demonstrated in artificially constructed layered magnetic structures [60,61]. However, the doubt over whether thin films can be viewed as an intrinsic 2D magnetic system has been long-existing, because film structure suffers from substrate effect like strain and nonuniformity with small islands [62]. Therefore, a substrate-free clean 2D flatland with magnetic LRO is highly desirable.

Since the discovery of graphene, tremendous efforts have been dedicated to inducing magnetic order in nonmagnetic 2D exfoliated samples. Various strategies have been employed including introducing local moments through defects [63,64], band structure engineering for obtaining high density of states (DOS) near Fermi level and causing Stoner instability [65-67], and magnetic proximity effect by fabricating 2D magnetic – nonmagnetic structures [68]. Particularly, great success has been achieved via band engineering, as correlation and instability-induced FM order is realized in pristine magnetic angle twist-bilayer graphene [69] and related systems. However, the relatively small magnetic moment and low Curie temperature hinder further application in ambient condition.

Instead of introducing magnetism in 2D systems, finding an exfoliated bulk crystal with intrinsic magnetic order down to few-layer limit has been a long-sought goal. Based on Mermin-Wagner theorem, bulk Ising magnet is a preferred starting point. In 2017, the first two intrinsic 2D magnetic systems, $Cr_2Ge_2Te_6$ [70] and CrI_3 [71], were reported, where $Cr_2Ge_2Te_6$ hosts 2D Heisenberg FM with a small applied magnetic field, and few-layer CrI_3 can be viewed as 2D Ising interlayer AFM. Since then, the field of 2D magnetic atomic crystals has been advancing rapidly, with more notable 2D VDW magnetic systems being discovered or predicted [72]. More importantly, the key feature of magnetic flatlands, control of the magnetism via external stimuli, has been demonstrated in various material platforms. For example, spin-lattice coupling, strain or pressure can substantially alter the magnetic moment direction and transition temperature in $Cr_2Ge_2Te_6$ [73]. Giant electric-field tunability has been observed in few-layer CrI_3 [74], where gating completely changes the magnetic GS from interlayer AFM to FM. The diverse magnetic properties and tunability of 2D magnets promise various device applications. Benefiting from atomically uniform and ultra-thin

layered structure, VDW magnets provide ideal ingredient for constructing magnetic tunnel junctions, the key building block of modern spintronics industry. For instance, although still limited in operating temperature, graphite-CrI_3-graphite heterostructure shows giant MR up to 10^6 % at 1.4 K [75], holding great promise in high-efficiency spintronic applications.

2.6 Previous studies on the structural and magnetic phases of CrI_3

In this section, we will briefly summarize the previous studies of semiconducting FM CrI_3, one of the first-discovered monolayer FM magnet. Our detailed Raman study on the magnetic structure of bulk CrI_3 will be presented in Chapter 6.

The Cr^{3+} ions of CrI_3 form a honeycomb lattice in edge-sharing octahedra. At room temperature, CrI_3 has monoclinic crystal structure with point group C_{2h} [76]. Below 220K, CrI_3 undergoes a first-order structural phase transition into a rhombohedral C_{3i} phase, with changes in the in-plane bond distance and a shearing of the layers. Although both phases stack in ABC sequence, the high-temperature structure has an in-plane displacement between layers which breaks the three-fold rotational symmetry, while in the low-temperature phase, each Cr^{3+} ion is directly over the honeycomb vacancy of the two adjacent layers, and thus the structure preserves the three-fold rotational symmetry along *z*-axis.

Magnetic measurements including magnetization, magnetic susceptibility [76] and Mössbauer spectroscopy [77] have shown that bulk CrI_3 is a strong anisotropic FM below its Curie temperature of 61K, with the magnetic moments of Cr ions pointing perpendicular to the layers.

With weak interlayer VDW bonding, relatively high Curie temperature, and a large magnetic anisotropy, CrI_3 and the family of CrX_3 (X = Br, Cl, I) have been theoretically predicted to be promising candidates for realizing intrinsic 2D FM [64,65]. Indeed, with exfoliated CrI_3 flakes, clear signature of FM order in monolayer CrI_3 is revealed with magneto-optical Kerr effect (MOKE) measurements (Figure 2.10 a). Similar to the bulk crystal, the FM order in monolayer CrI_3 has out-of-plane easy axis and the Curie temperature is around 45K [71]. However, systematic layer dependent magnetic measurement shows completely unexpected behavior. Figure 2.10 shows the evolution from FM order in monolayer to the vanishing net moment in bilayer CrI_3 at low field, then to the stored net moment in tri-layer CrI_3, strongly suggesting the interlayer AFM coupling in the thin flake limit, distinct from the bulk [71]. Tunneling measurements also displays stepped tunneling currents with external magnetic field, confirming the interlayer AFM in CrI_3 flakes [78-80]. Figure 2.11 shows the puzzling evolution from bulk FM to few-layer interlayer AFM and it remains an open question on the mechanism behind the layer dependent crossover, although some tentative explanations including external effects introduced by strain or capping layer have been given [81-84].

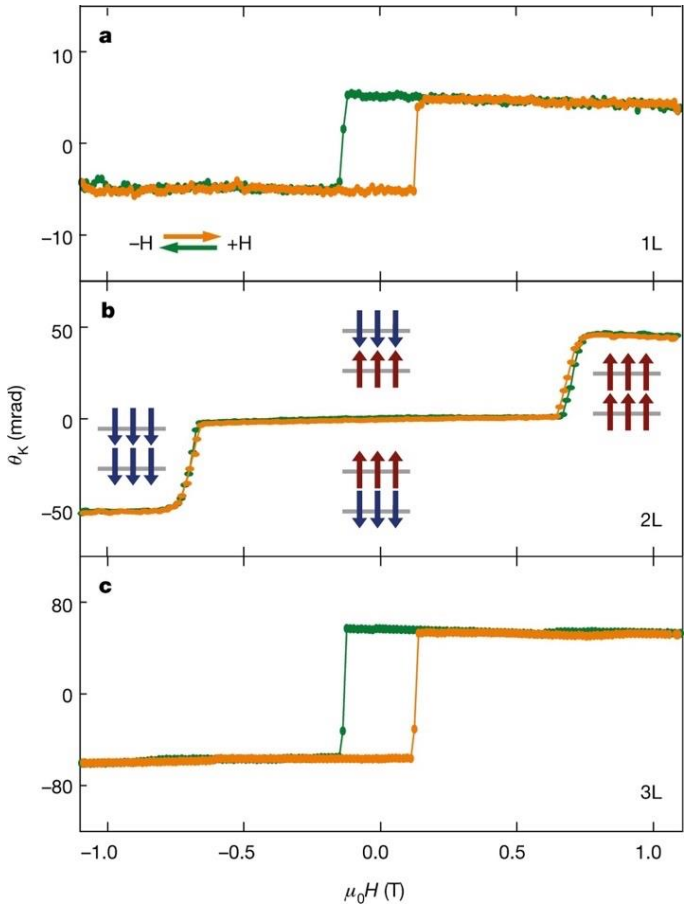

Figure 2.10 (a-c) MOKE measurements on 1-3 layers of CrI_3 flakes, adapted from Reference [71] with permission.

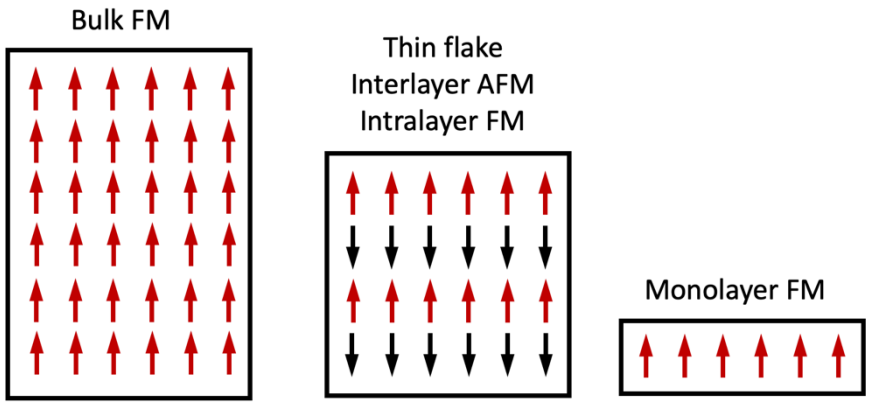

Figure 2.11 Illustrations of the thickness dependence of CrI_3 magnetism.

To solve this magnetic puzzle, our collaborative study probes the magnetic structure of bulk CrI_3. It is the limited penetration depth of optical techniques that permits the probing of its thin-layer magnetism within its bulk. With magnetic field-dependent Raman spectroscopy of the magnons, our study unambiguously shows the coexistence of AFM and FM magnons even in bulk CrI_3, which further suggests that bulk CrI_3 actually hosts interlayer AFM at its surface and interlayer FM in its deeper bulk (Fig 2.12), instead of the uniform FM order as reported in previous literature. It provides a natural explanation of the evolution from the FM in 3D bulk to the layered AFM in 2D flakes.

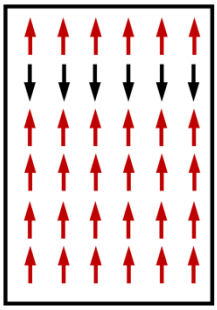

Figure 2.12 Coexistence of surface interlayer AFM and bulk interlayer FM in bulk CrI_3.

References

[1] J. A. Sobota, Y. He, and Z.-X. Shen, *Angle-resolved photoemission studies of quantum materials*, Reviews of Modern Physics **93**, 025006 (2021).

[2] J. H. Van Vleck, *Electric and magnetic susceptibilities* (Clarendon Press, 1932).

[3] J. Kim *et al.*, *Large spin-wave energy gap in the bilayer iridate $Sr_3Ir_2O_7$: Evidence for enhanced dipolar interactions near the mott metal-insulator transition*, Physical review letters **109**, 157402 (2012).

[4] P. A. Lee, N. Nagaosa, and X.-G. Wen, *Doping a Mott insulator: Physics of high-temperature superconductivity*, Reviews of modern physics **78**, 17 (2006).

[5] A. Damascelli, Z. Hussain, and Z.-X. Shen, *Angle-resolved photoemission studies of the cuprate superconductors*, Reviews of modern physics **75**, 473 (2003).

[6] W. Hardy, D. Bonn, D. Morgan, R. Liang, and K. Zhang, *Precision measurements of the temperature dependence of λ in $YBa_2Cu_3O_{6.95}$: Strong evidence for nodes in the gap function*, Physical Review Letters **70**, 3999 (1993).

[7] B. Keimer *et al.*, *Magnetic excitations in pure, lightly doped, and weakly metallic La_2CuO_4*, Physical Review B **46**, 14034 (1992).

[8] J. Tranquada, B. Sternlieb, J. Axe, Y. Nakamura, and S. Uchida, *Evidence for stripe correlations of spins and holes in copper oxide superconductors*, nature **375**, 561 (1995).

[9] P. Abbamonte, A. Rusydi, S. Smadici, G. Gu, G. Sawatzky, and D. Feng, *Spatially modulated'mottness' in $La_{2-x}Ba_xCuO_4$*, Nature Physics **1**, 155 (2005).

[10] Y. Ando, Y. Hanaki, S. Ono, T. Murayama, K. Segawa, N. Miyamoto, and S. Komiya, *Carrier concentrations in $Bi_2Sr_{2-z}La_zCuO_{6+\delta}$ single crystals and their relation to the Hall coefficient and thermopower*, Physical Review B **61**, R14956 (2000).

[11] M. Gurvitch and A. Fiory, *Resistivity of $La_{1.825}Sr_{0.175}CuO_4$ and $YBa_2Cu_3O_7$ to 1100 K: absence of saturation and its implications*, Physical review letters **59**, 1337 (1987).

[12] R. Cooper *et al.*, *Anomalous criticality in the electrical resistivity of $La_{2-x}Sr_xCuO_4$*, Science **323**, 603 (2009).

[13] S. Martin, A. T. Fiory, R. Fleming, L. Schneemeyer, and J. V. Waszczak, *Normal-state transport properties of $Bi_{2+x}Sr_{2-y}CuO_{6+\delta}$ crystals*, Physical Review B **41**, 846 (1990).

[14] Z. X. Shen and G. Sawatzky, *Novel electronic structure of cuprate superconductors revealed by the anomalous spectral lineshape in ARPES experiments*, physica status solidi (b) **215**, 523 (1999).

[15] J. Axe, A. Moudden, D. Hohlwein, D. Cox, K. Mohanty, A. Moodenbaugh, and Y. Xu, *Structural phase transformations and superconductivity in $La_{2-x}Ba_xCuO_4$*, Physical review letters **62**, 2751 (1989).

[16] D. Hsieh, D. Qian, L. Wray, Y. Xia, Y. S. Hor, R. J. Cava, and M. Z. Hasan, *A topological Dirac insulator in a quantum spin Hall phase*, Nature **452**, 970 (2008).

[17] W. Witczak-Krempa, G. Chen, Y. B. Kim, and L. Balents, *Correlated Quantum Phenomena in the Strong Spin-Orbit Regime*, Annual Review of Condensed Matter Physics **5**, 57 (2014).

[18] B. Kim *et al.*, *Novel J_{eff} = 1/2 Mott state induced by relativistic spin-orbit coupling in Sr_2IrO_4*, Physical review letters **101**, 076402 (2008).

[19] B. Kim, H. Ohsumi, T. Komesu, S. Sakai, T. Morita, H. Takagi, and T.-h. Arima, *Phase-sensitive observation of a spin-orbital Mott state in Sr_2IrO_4*, Science **323**, 1329 (2009).

[20] S. Fujiyama, H. Ohsumi, T. Komesu, J. Matsuno, B. Kim, M. Takata, T. Arima, and H. Takagi, *Two-dimensional Heisenberg behavior of J_{eff} = 1/2 isospins in the paramagnetic state of the spin-orbital Mott insulator Sr_2IrO_4*, Physical review letters **108**, 247212 (2012).

[21] J. Kim *et al.*, *Magnetic excitation spectra of Sr_2IrO_4 probed by resonant inelastic X-ray scattering: establishing links to cuprate superconductors*, Physical Review Letters **108**, 177003 (2012).

[22] J. Kim, Y. Choi, J. Kim, J. Mitchell, G. Jackeli, M. Daghofer, J. Van Den Brink, G. Khaliullin, and B. Kim, *Dimensionality driven spin-flop transition in layered iridates*, Physical review letters **109**, 037204 (2012).

[23] S. Fujiyama, K. Ohashi, H. Ohsumi, K. Sugimoto, T. Takayama, T. Komesu, M. Takata, T. Arima, and H. Takagi, *Weak antiferromagnetism of J_{eff} = 1/2 band in bilayer iridate $Sr_3Ir_2O_7$*, Physical Review B **86**, 174414 (2012).

[24] P. King *et al.*, *Spectroscopic indications of polaronic behavior of the strong spin-orbit insulator $Sr_3Ir_2O_7$*, Physical Review B **87**, 241106 (2013).

[25] Y. Singh and P. Gegenwart, *Antiferromagnetic Mott insulating state in single crystals of the honeycomb lattice material Na_2IrO_3*, Physical Review B **82**, 064412 (2010).

[26] Y. Singh, S. Manni, J. Reuther, T. Berlijn, R. Thomale, W. Ku, S. Trebst, and P. Gegenwart, *Relevance of the Heisenberg-Kitaev model for the honeycomb lattice iridates A_2IrO_3*, Physical review letters **108**, 127203 (2012).

[27] H. Gretarsson *et al.*, *Crystal-field splitting and correlation effect on the electronic structure of A_2IrO_3*, Physical review letters **110**, 076402 (2013).

[28] X. Liu *et al.*, *Long-range magnetic ordering in Na_2IrO_3*, Physical Review B **83**, 220403 (2011).

[29] J. Clancy, N. Chen, C. Kim, W. Chen, K. Plumb, B. Jeon, T. Noh, and Y.-J. Kim, *Spin-orbit coupling in iridium-based 5d compounds probed by x-ray absorption spectroscopy*, Physical Review B **86**, 195131 (2012).

[30] S. Choi *et al.*, *Spin waves and revised crystal structure of honeycomb iridate Na_2IrO_3*, Physical review letters **108**, 127204 (2012).

[31] M. Sakata, T. Kagayama, K. Shimizu, K. Matsuhira, S. Takagi, M. Wakeshima, and Y. Hinatsu, *Suppression of metal-insulator transition at high pressure and pressure-induced magnetic ordering in pyrochlore oxide $Nd_2Ir_2O_7$*, Physical Review B **83**, 041102 (2011).

[32] T. Qi, O. Korneta, X. Wan, L. DeLong, P. Schlottmann, and G. Cao, *Strong magnetic instability in correlated metallic $Bi_2Ir_2O_7$*, Journal of Physics: Condensed Matter **24**, 345601 (2012).

[33] K. Matsuhira, M. Wakeshima, R. Nakanishi, T. Yamada, A. Nakamura, W. Kawano, S. Takagi, and Y. Hinatsu, *Metal–Insulator Transition in Pyrochlore Iridates $Ln_2Ir_2O_7$ (Ln = Nd, Sm, and Eu)*, Journal of the Physical Society of Japan **76**, 043706 (2007).

[34] Y. Okamoto, M. Nohara, H. Aruga-Katori, and H. Takagi, *Spin-liquid state in the S = 1/2 hyperkagome antiferromagnet* $Na_4Ir_3O_8$, Physical review letters **99**, 137207 (2007).

[35] H. Kuriyama *et al.*, *Epitaxially stabilized iridium spinel oxide without cations in the tetrahedral site*, Applied Physics Letters **96**, 182103 (2010).

[36] D. Yanagishima and Y. Maeno, *Metal-nonmetal changeover in pyrochlore iridates*, Journal of the Physical Society of Japan **70**, 2880 (2001).

[37] Y. Shi *et al.*, *Continuous metal-insulator transition of the antiferromagnetic perovskite* $NaOsO_3$, Physical Review B **80**, 161104 (2009).

[38] J. Yamaura *et al.*, *Tetrahedral magnetic order and the metal-insulator transition in the pyrochlore lattice of* $Cd_2Os_2O_7$, Physical review letters **108**, 247205 (2012).

[39] O. Schirmer, A. Forster, H. Hesse, M. Wohlecke, and S. Kapphan, *Paramagnetic resonance and near-infrared optical absorption of* $SrTiO_3$*:* Ir^{4+}, Journal of Physics C: Solid State Physics **17**, 1321 (1984).

[40] J. G. Rau, E. K.-H. Lee, and H.-Y. Kee, *Spin-Orbit Physics Giving Rise to Novel Phases in Correlated Systems: Iridates and Related Materials*, Annual Review of Condensed Matter Physics **7**, 195 (2016).

[41] A. Abragam and B. Bleaney, *Electron paramagnetic resonance of transition ions* (OUP Oxford, 2012).

[42] G. Jackeli and G. Khaliullin, *Mott insulators in the strong spin-orbit coupling limit: from Heisenberg to a quantum compass and Kitaev models*, Physical review letters **102**, 017205 (2009).

[43] Y. K. Kim, N. Sung, J. Denlinger, and B. Kim, *Observation of ad-wave gap in electron-doped* Sr_2IrO_4, Nature Physics **12**, 37 (2016).

[44] Y. K. Kim, O. Krupin, J. Denlinger, A. Bostwick, E. Rotenberg, Q. Zhao, J. Mitchell, J. Allen, and B. Kim, *Fermi arcs in a doped pseudospin-1/2 Heisenberg antiferromagnet*, Science **345**, 187 (2014).

[45] S. Moon *et al.*, *Dimensionality-Controlled Insulator-Metal Transition and Correlated Metallic State in 5d Transition Metal Oxides* $Sr_{n+1}Ir_nO_{3n+1}$ *(n = 1, 2, and ∞)*, Physical review letters **101**, 226402 (2008).

[46] F. Wang and T. Senthil, *Twisted Hubbard model for Sr_2IrO_4: magnetism and possible high temperature superconductivity*, Physical Review Letters **106**, 136402 (2011).

[47] J. G. Vale and E. C. Hunter, *Putative magnetic quantum criticality in $(Sr_{1-x}La_x)_3Ir_2O_7$*, Physical Review B **98**, 100406 (2018).

[48] T. Hogan *et al.*, *First-order melting of a weak spin-orbit Mott insulator into a correlated metal*, Physical review letters **114**, 257203 (2015).

[49] H. Chu, L. Zhao, A. de la Torre, T. Hogan, S. Wilson, and D. Hsieh, *A charge density wave-like instability in a doped spin–orbit-assisted weak Mott insulator*, Nature materials **16**, 200 (2017).

[50] X. Lu, D. McNally, M. M. Sala, J. Terzic, M. Upton, D. Casa, G. Ingold, G. Cao, and T. Schmitt, *Doping Evolution of Magnetic Order and Magnetic Excitations in $(Sr_{1-x}La_x)_3Ir_2O_7$*, Physical review letters **118**, 027202 (2017).

[51] G. Affeldt, T. Hogan, C. L. Smallwood, T. Das, J. D. Denlinger, S. D. Wilson, A. Vishwanath, and A. Lanzara, *Spectral weight suppression near a metal-insulator transition in a double-layer electron-doped iridate*, Physical Review B **95**, 235151 (2017).

[52] E. C. Hunter, *An exploration of novel correlated electronic states in 5d transition metal oxides* (University of Edinburgh, 2016).

[53] G. Cao, J. Bolivar, S. McCall, J. Crow, and R. Guertin, *Weak ferromagnetism, metal-to-nonmetal transition, and negative differential resistivity in single-crystal Sr_2IrO_4*, Physical Review B **57**, R11039 (1998).

[54] M. M. Sala *et al.*, *Evidence of quantum dimer excitations in $Sr_3Ir_2O_7$*, Physical Review B **92**, 024405 (2015).

[55] T. Hogan, R. Dally, M. Upton, J. Clancy, K. Finkelstein, Y.-J. Kim, M. Graf, and S. D. Wilson, *Disordered dimer state in electron-doped $Sr_3Ir_2O_7$*, Physical Review B **94**, 100401 (2016).

[56] K. S. Novoselov, A. K. Geim, S. V. Morozov, D. Jiang, Y. Zhang, S. V. Dubonos, I. V. Grigorieva, and A. A. Firsov, *Electric field effect in atomically thin carbon films*, science **306**, 666 (2004).

[57] N. D. Mermin and H. Wagner, *Absence of ferromagnetism or antiferromagnetism in one- or two-dimensional isotropic Heisenberg models*, Physical Review Letters **17**, 1133 (1966).

[58] P. Fleury and R. Loudon, *Scattering of light by one-and two-magnon excitations*, Physical Review **166**, 514 (1968).

[59] R. B. Griffiths, *Peierls proof of spontaneous magnetization in a two-dimensional Ising ferromagnet*, Physical Review **136**, A437 (1964).

[60] M. N. Baibich, J. M. Broto, A. Fert, F. N. Van Dau, F. Petroff, P. Etienne, G. Creuzet, A. Friederich, and J. Chazelas, *Giant magnetoresistance of (001) Fe/(001) Cr magnetic superlattices*, Physical review letters **61**, 2472 (1988).

[61] G. Binasch, P. Grünberg, F. Saurenbach, and W. Zinn, *Enhanced magnetoresistance in layered magnetic structures with antiferromagnetic interlayer exchange*, Physical review B **39**, 4828 (1989).

[62] L. Falicov *et al.*, *Surface, interface, and thin-film magnetism*, Journal of Materials Research **5**, 1299 (1990).

[63] O. V. Yazyev and L. Helm, *Defect-induced magnetism in graphene*, Physical Review B **75**, 125408 (2007).

[64] M. M. Ugeda, I. Brihuega, F. Guinea, and J. M. Gómez-Rodríguez, *Missing atom as a source of carbon magnetism*, Physical Review Letters **104**, 096804 (2010).

[65] O. V. Yazyev and M. Katsnelson, *Magnetic correlations at graphene edges: basis for novel spintronics devices*, Physical review letters **100**, 047209 (2008).

[66] J. Jung, T. Pereg-Barnea, and A. MacDonald, *Theory of interedge superexchange in zigzag edge magnetism*, Physical review letters **102**, 227205 (2009).

[67] Y.-W. Son, M. L. Cohen, and S. G. Louie, *Half-metallic graphene nanoribbons*, Nature **444**, 347 (2006).

[68] Z. Wang, C. Tang, R. Sachs, Y. Barlas, and J. Shi, *Proximity-induced ferromagnetism in graphene revealed by the anomalous Hall effect*, Physical review letters **114**, 016603 (2015).

[69] A. L. Sharpe, E. J. Fox, A. W. Barnard, J. Finney, K. Watanabe, T. Taniguchi, M. Kastner, and D. Goldhaber-Gordon, *Emergent ferromagnetism near three-quarters filling in twisted bilayer graphene*, Science **365**, 605 (2019).

[70] C. Gong *et al.*, *Discovery of intrinsic ferromagnetism in two-dimensional van der Waals crystals*, Nature **546**, 265 (2017).

[71] B. Huang *et al.*, *Layer-dependent ferromagnetism in a van der Waals crystal down to the monolayer limit*, Nature **546**, 270 (2017).

[72] C. Gong and X. Zhang, *Two-dimensional magnetic crystals and emergent heterostructure devices*, Science **363** (2019).

[73] Z. Lin *et al.*, *Pressure-induced spin reorientation transition in layered ferromagnetic insulator* $Cr_2Ge_2Te_6$, Physical Review Materials **2**, 051004 (2018).

[74] S. Jiang, L. Li, Z. Wang, K. F. Mak, and J. Shan, *Controlling magnetism in 2D* CrI_3 *by electrostatic doping*, Nature nanotechnology **13**, 549 (2018).

[75] H. H. Kim, B. Yang, T. Patel, F. Sfigakis, C. Li, S. Tian, H. Lei, and A. W. Tsen, *One million percent tunnel magnetoresistance in a magnetic van der Waals heterostructure*, Nano letters **18**, 4885 (2018).

[76] M. A. McGuire, H. Dixit, V. R. Cooper, and B. C. Sales, *Coupling of Crystal Structure and Magnetism in the Layered, Ferromagnetic Insulator CrI3*, Chemistry of Materials **27**, 612 (2015).

[77] J. Friedt and J. Sanchez, *Origin of the magnetic hyperfine field transferred at iodine in ferromagnetic* CrI_3, Journal of Physics C: Solid State Physics **11**, 3731 (1978).

[78] D. R. Klein *et al.*, *Probing magnetism in 2D van der Waals crystalline insulators via electron tunneling*, Science **360**, 1218 (2018).

[79] T. Song *et al.*, *Giant tunneling magnetoresistance in spin-filter van der Waals heterostructures*, Science **360**, 1214 (2018).

[80] H. H. Kim, B. Yang, S. Tian, C. Li, G.-X. Miao, H. Lei, and A. W. Tsen, *Tailored tunnel magnetoresistance response in three ultrathin chromium trihalides*, Nano letters **19**, 5739 (2019).

[81] D. Shcherbakov *et al.*, *Raman spectroscopy, photocatalytic degradation, and stabilization of atomically thin chromium tri-iodide*, Nano letters **18**, 4214 (2018).

[82] N. Sivadas, S. Okamoto, X. Xu, C. J. Fennie, and D. Xiao, *Stacking-dependent magnetism in bilayer CrI_3*, Nano letters **18**, 7658 (2018).

[83] D. Soriano, C. Cardoso, and J. Fernández-Rossier, *Interplay between interlayer exchange and stacking in CrI_3 bilayers*, Solid State Communications **299**, 113662 (2019).

[84] P. Jiang, C. Wang, D. Chen, Z. Zhong, Z. Yuan, Z.-Y. Lu, and W. Ji, *Stacking tunable interlayer magnetism in bilayer CrI_3*, Physical Review B **99**, 144401 (2019).

Chapter 3 Experimental and Theoretical Techniques

Having discussed the two quantum magnet systems of our interest, in this chapter we will focus on our experimental and theoretical techniques, polarized Raman spectroscopy and spin-wave calculations. We will first introduce Raman spectroscopy as a widely used tool for charactering material properties, followed by a theoretical description of Raman scattering process and selection rules. Then we will elaborate on our Raman setup at the University of Michigan. In the end, we will present our main theoretical tool, the spin wave theory, for understanding our Raman experimental observations.

3.1 Basic Principles of Raman Spectroscopy

Raman scattering is an inelastic scattering process of visible light photon by the excitations in matter. It is named after the Nobel Prize laureate C. V. Raman who observed the effect in organic liquid in 1928 [1], 5 years after the theoretical prediction [2]. During a Raman scattering process, an incident photon excites the electrons into a virtual state. Instead of a real excited state which tends to fully absorb the light, the virtual state is unstable and quickly radiates a photon. Depending on the energy of the radiated photon equal, lower or higher than the incident photon, the scattering process is named an elastic Rayleigh process, a Stokes process, or an anti-Stokes process. Raman scattering is an inelastic scattering process, where the energy loss or gain of the photon corresponds to an excitation of the matter. Through analyzing the energy spectrum of the scattered photon, the

energy of the excitation can be obtained. Typical Raman-accessible excitations include phonons [3,4], plasmon [4], magnons [5], charge order [6], *etc*., with excitation energies ranging from a few meV to hundreds of meV.

Nowadays, Raman spectroscopy has become a powerful tool for identifying crystals, molecules and even proteins and DNAs by providing their unique structure fingerprints, *i.e.* phonons, and is thus widely used in both academy and industry. With modern designs of lasers and detectors, Raman spectroscopy has achieved higher sensitivity, faster data acquisition speed, and higher energy resolution comparing with other common techniques. Moreover, different variants of Raman techniques have been developed to satisfy various requirements. For instance, in order to obtain high spatial resolution, Raman microscopy (μm spatical resolution) and near-field scanning Raman microscopy (nm spatial resolution) utilize high NA objective and atomically sharp metallic tip. Polarized Raman spectroscopy, which will be discussed in detail later, provides additional symmetry information of the excitations, which is crucial in understanding the physics origin of Raman active modes and also the structure, orientation and symmetry of the study subject.

In order to gain more intuitive understanding of the Raman scattering process, we adopt a macroscopic approach to describe the phenomenon theoretically. If we consider an incident light with electric field $\vec{E}_I$, it induces a polarization in a material

$$\vec{P} = \epsilon_0 \chi \vec{E}_I \tag{3.1}$$

where χ is the linear electric susceptibility tensor of the material. The various excitations of the matter, for example phonons of the lattice vibrational modes, cause fluctuations in χ and thus $\vec{P}$.

Due to the oscillations of the electric dipole, the electrons radiate scattered light out of the material, whose electric field satisfies

$$(\nabla^2 + k_S^2)\vec{E}_S = -\frac{\omega_S^2}{\epsilon_0 c^2}\vec{P} \tag{3.2}$$

where the subscript S denotes scattered light. k_S and ω_S represent the wave vector and energy of the scattered photon, respectively.

The solution to Equation 3.2 is

$$\vec{E}_S(\vec{r},\omega_S) = \frac{\omega_S^2}{4\pi\epsilon_0 c^2}\int d^3\vec{r}'\,\frac{e^{ik_S|\vec{r}-\vec{r}'|}}{|\vec{r}-\vec{r}'|}\vec{P}(\vec{r}',\omega_S) \tag{3.3}$$

where the integration is over the scattering region. Consider $|\vec{r}| \gg |\vec{r}'|$, Equation 3.3 becomes

$$\vec{E}_S(\vec{r},\omega_S) = \frac{\omega_S^2}{4\pi\epsilon_0 c^2}\frac{e^{ik_S|\vec{r}|}}{|\vec{r}|}\int d^3\vec{r}'\,e^{-i\vec{k}_S\cdot\vec{r}'}\vec{P}(\vec{r}',\omega_S) \tag{3.4}$$

The intensity of the scattered light with polarization $\vec{\epsilon}_S$ can be written as

$$2\epsilon_0 c n_S\langle\vec{\epsilon}_S\cdot\vec{E}_S^*(\vec{r},\omega_S)\vec{\epsilon}_S\cdot\vec{E}_S(\vec{r},\omega_S)\rangle \tag{3.5}$$

where the bracket denotes an average.

Combining Equations 3.4 and 3.5, we arrive at the cross section of Raman scattering [7-9]

$$\frac{d^2\sigma}{d\Omega d\omega_S} = \frac{\omega_I\omega_S^3 V}{(4\pi\epsilon_0)^2 c^4}\frac{n_S}{n_I}\frac{1}{\left|\vec{E}_I\right|^2}\langle\vec{\epsilon}_S\cdot\vec{P}^*(\vec{k}_S,\omega_S)\vec{\epsilon}_S\cdot\vec{P}(\vec{k}_S,\omega_S)\rangle \tag{3.6}$$

where ω_I and ω_S are the frequencies of the incident and scattered light, n_I and n_S are the refractive indices of the incident and scattered light in the material, V is the volume of the material

that contributes to the scattering process, and $\vec{\epsilon}_S$ is the direction of the scattered light. Although the scattered light radiates in all directions, its intensity varies as a function of $\vec{\epsilon}_S$, which contains symmetry information that is especially important in our work.

Next we replace the incident light-induced polarization $\vec{P}$ in Equation 3.6 with Equation 3.1, whose form depends on the nature of the excitations that we are interested in. For nonmagnetic excitations, χ can be expanded in terms of the fluctuations caused by the excitations X around its equilibrium position. If we take the leading order expansion

$$\chi = \chi_0 + \left(\frac{d\chi}{dX}\right)_0 X + \cdots \tag{3.7}$$

The resulting Raman cross section is given by

$$\frac{d^2\sigma}{d\Omega d\omega_S} = \frac{\omega_I \omega_S^3 V}{(4\pi)^2 c^4} \frac{n_S}{n_I} \left| \vec{\epsilon}_S \cdot \frac{d\chi}{dX} \cdot \vec{\epsilon}_I \right|^2 \langle X(q,\omega) X^*(q,\omega) \rangle \tag{3.8}$$

For magnetic excitations, due to the symmetry properties of the magnetization, the polarization fluctuation and Raman cross section can be written as

$$\vec{P}^{(1)} = \epsilon_0 \frac{d\chi}{dM} \vec{M} \times \vec{E}_I \tag{3.9}$$

$$\frac{d^2\sigma}{d\Omega d\omega_S} = \frac{\omega_I \omega_S^3 V}{(4\pi)^2 c^4} \frac{n_S}{n_I} (\vec{\epsilon}_S \times \vec{\epsilon}_I)_i (\vec{\epsilon}_S \times \vec{\epsilon}_I)_j \langle M_i M_j^* \rangle \tag{3.10}$$

where $\vec{M}$ is the magnetic moment vector. Note that Equation 3.9 again involves only the leading order expansion in magnetization $\vec{M}$. A higher order expansion might be necessary depending on the material system, for example the magnons in CrI_3. Details will be given in Section 6.4.

3.2 Raman Scattering Selection Rules

Using group theoretical methods, we can determine whether two states (ϵ_S and ϵ_I in our case) are coupled to the interaction matrix ($\frac{d\chi}{dX}$ in the non-magnetic case as an example) by symmetry analysis [10]. In the case of Raman spectroscopy, we vary the polarizations of the incident and scattered light ϵ_I and ϵ_S to observe different modes with certain symmetry properties. The terms $\left|\vec{\epsilon}_S \cdot \frac{d\chi}{dX} \cdot \vec{\epsilon}_I\right|$ in Equation 3.8 and $(\vec{\epsilon}_S \times \vec{\epsilon}_I)_i(\vec{\epsilon}_S \times \vec{\epsilon}_I)_j$ in Equation 3.10 contain this symmetry information. It is required that those terms must be invariant under all the symmetry operations of the crystal's point group, *i.e.* transform as the fully symmetric A_1 representation, to be non-vanishing [8,10-12]. In other word, a phonon can be observed in a Raman process if its irreducible representation corresponds to one of the reduced irreducible representations of the representation of the polarizability tensor.

As an example, we show how to derive the symmetry-allowed phonon modes of the tetragonal D_{4h} point group. The polarizations ϵ_S and ϵ_I transform as polar vectors. In the D_{4h} point group, the irreducible representations A_{2u} and E_u transform as polar vectors, representing light polarizations. By taking the direct product of A_{2u} and E_u, we arrive at the collection of the irreducible representations of all the Raman phonons [8,10]. Equation 3.11 shows the decomposition of the reducible representation of $A_{2u}\otimes A_{2u} + E_u\otimes E_u$, which suggests that the Raman-allowed phonons take the symmetry from A_{1g}, A_{2g}, B_{1g}, B_{2g}, or E_g.

$$A_{2u}\otimes A_{2u} + E_u\otimes E_u = A_{1g} + A_{2g} + B_{1g} + B_{2g} + E_g \tag{3.11}$$

For any irreducible representation of a specific crystal symmetry, a Raman tensor can be written which relates the polarization of the scattered light with the polarization of the incident light. A table of the Raman-active irreducible representations and their corresponding Raman tensors for different crystal symmetries are available in many Raman-related materials [9,12].

The selection rule for magnetic excitations is drastically different. From the term $(\vec{\epsilon}_S \times \vec{\epsilon}_I)_i(\vec{\epsilon}_S \times \vec{\epsilon}_I)_j$ in Equation 3.10, we see that to probe magnetic excitations, the polarizations of the incident and scattered light need to be orthogonal. This orthogonality is very important in distinguishing magnetic from non-magnetic excitations in Raman spectroscopy technique. However, we note that Equations 3.9 and 3.10 assume that the magnetic excitation alters the net magnetization of the material, for example the local spin-flip excitation or the collective single magnon excitation. If the magnetic excitation does not induce a net magnetization, for example the two-magnon excitation, the selection rule above does not apply anymore. Additionally, as aforementioned in the last section, higher order expansion of the magnetization also leads to the break-down of this orthogonality rule, for example in the case of the single magnon in CrI_3. A detailed discussion of a quadratic expansion in CrI_3 magnetization will be given in Section 6.4.

3.3 Polarized Raman Spectroscopy Setup

Figure 3.1 shows the design of our Raman setup. Because the laser source and the spectrometer are commercial ones, my responsibility is to build the beam path which directs the incident light to the sample and collects the scattered light to the spectrometer with an ideal efficiency. Following the light propagation direction, the optical components are in order as follows:

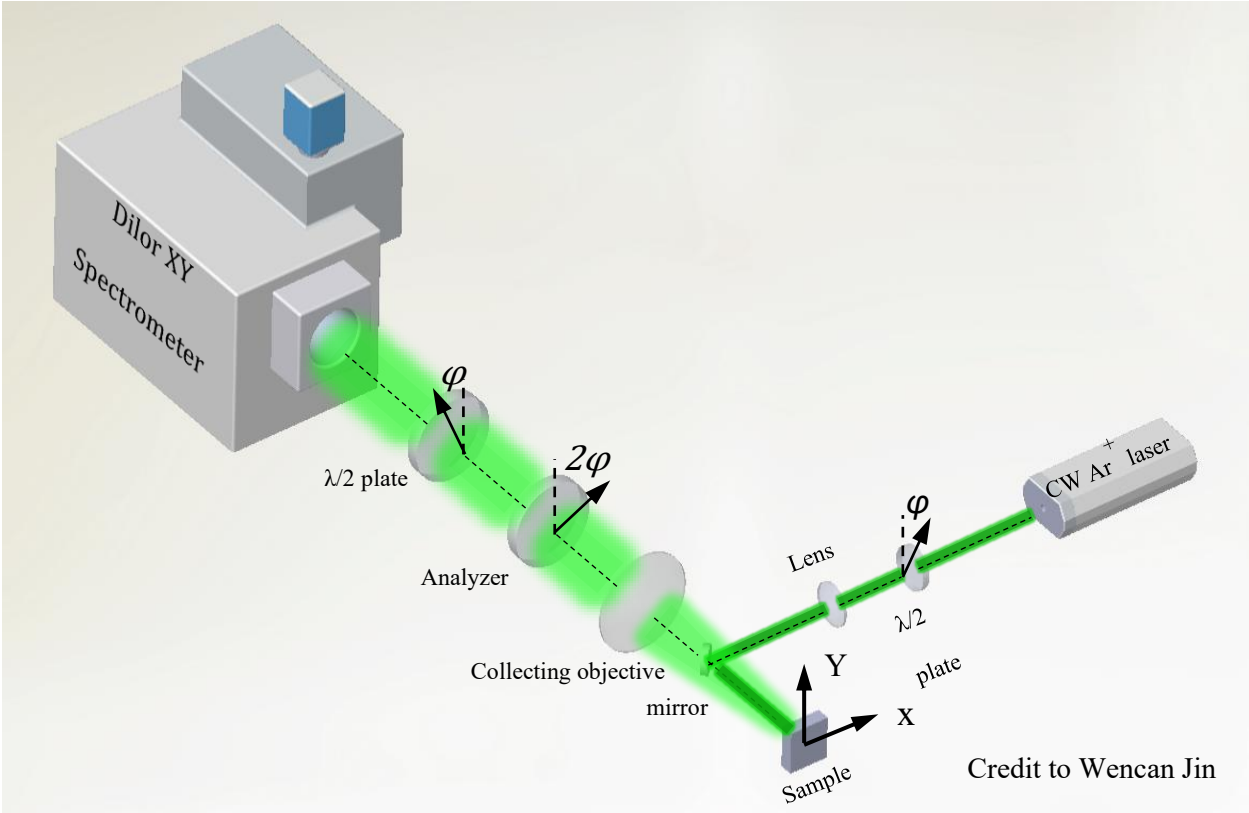

Figure 3.1 Schematics of the polarized Raman spectroscopy setup at the University of Michigan. A photo of the real setup will be shown in Figure 4.6 in Section 4.2.2.

- A 514 nm Argon ion laser (Spectra Physics 2580CWR), which runs in continuous-wave (CW) mode with high frequency and power stability. A chiller (Spectra Physics Model 314) is used for stabilizing the temperature of the laser.
- A zero-order half-wave plate (HWP) that rotates the linearly polarized light to our desired polarization.
- A collimating lens (f = 3”) that focuses the beam of ~100 μm on the sample in a high-vacuum optical cryostat (Janis ST-300).

- A small mirror (radius = 1/8") which directs the incident beam while not blocking too much of the back-scattered Raman signal.
- A high numerical aperture (NA = 1.2) collecting objective (Nikon Nikkor 50 mm 1:1.2) which collimates the Raman signal.
- An analyzer which determines the $\vec{\epsilon}_S$.
- Another HWP that rotates the $\vec{\epsilon}_S$ to the vertical direction, because Raman spectrometers are an order of magnitude more sensitive to vertically polarized light than horizontally polarized light.
- Raman spectrometer (triple-grating Dilor XY spectrometer). It allows for switching between a 600 g/mm and a 1800 g/mm grating.

Similar to other spectroscopy techniques that involves a light source, Raman spectroscopy requires a highly monochromatic and frequency-stabilized light source for obtaining high resolution data. Thus a temperature stabilized CW laser is usually adopted.

A typical Raman setup measures the mode energy and linewidth but not necessarily its symmetry. In our work, as aforementioned, symmetry information is very important in distinguishing magnetic from non-magnetic excitations. Thus our setup utilizes the polarizer and analyzer, and "polarized" is emphasized throughout this thesis.

In some Raman setups, an optical filter is used to block the back-scattered elastic scattered beam. However, the filter is not necessary for our setup, as the high power Rayleigh scattering is blocked by an internal slit of our Dilor Raman spectrometer. Through rotating the direction of the gratings,

we can also avoid the laser line and protect the high-sensitivity detector. A recently manufactured Raman spectrometer normally uses a notch filter to attenuate the Rayleigh scattering at a specific wavelength. Additionally, using a notch filter allows for measuring the Stokes and anti-Stokes side at the same time. Ultra-low energy excitations (< 10 cm^{-1}) can also be observed with this type of spectrometer. On the contrary, if we try to measure such low-energy excitations with Dilor Raman spectrometer, the Rayleigh scattering will be spatially too close to the slit edge so that it gets diffracted into the CCD camera and show up as low-energy Raman signal, preventing such low-energy measurement of real signal. On the other hand, Dilor Raman spectrometer has its own advantage. Because notch filters only work at a specific wavelength, we need to carefully design the notch filter given the laser source. Dilor Raman spectrometer, on the contrary, can work with a wide range of laser wavelength. The two setups outside of the University of Michigan that have been used in our work are both equipped with notch filter-based spectrometers.

High energy resolution is a significant advantage of Raman spectroscopy. Figure 3.2 shows the components inside the Dilor Raman spectrometer. Many factors affect the energy resolution of a Raman spectrometer, including the diffraction grating, the slit size, the spectrometer focal length, and the detector [13]. The groove density of the grating typically ranges from 300 g/mm to 1800 g/mm. Higher groove density allows for higher energy resolution with sacrifice of its spectral range. The slit size balances the spectral resolution and throughput. The higher slit size, the lower energy resolution and the higher power throughput. The spectrometer focal length is the distance between the focusing mirror (M10) and the detector (CCD). Longer focal length allows for larger spatial separation and higher resolution, but the spectrometer is less compact in size. The detector of a Raman spectrometer is often a high-solution CCD array whose pixel size affects the resolution.

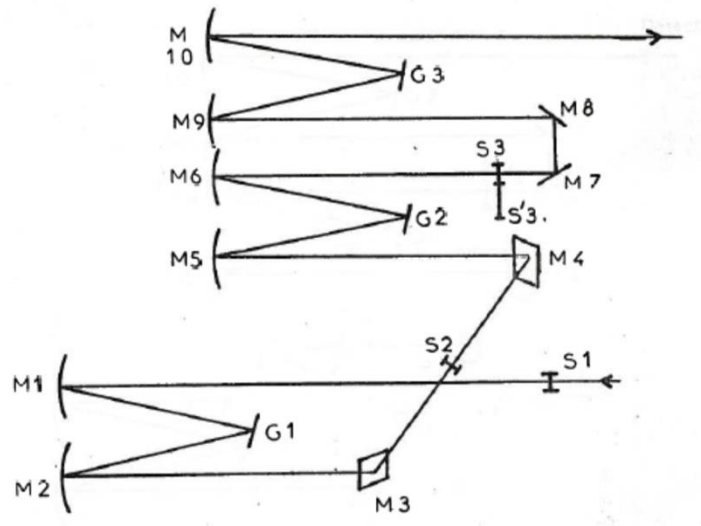

Figure 3.2 The components inside Dilor Raman spectrometer [14]. S/M/G stands for slit/ mirror/grating.

Three different Raman spectroscopy setups have been used for my studies. Magnetic field tunability is not supplied in our Raman setup, thus we turn to external resources. Raman measurements of perovskite iridates $Sr_3Ir_2O_7$ and Sr_2IrO_4 are performed at the University of Michigan and the National High Magnetic Field Lab (NHMFL). The Raman data of our collaborative work on bulk CrI_3 were acquired at Texas Tech University.

At NHMFL, a 532 nm sapphire laser (Coherent Sapphire SF NX 532) provides the continuous-wave (CW) incident light, and a Princeton Instrument TriVista spectrometer (PI Acton TriVista 557) is used to collect the scattered light. Samples are placed inside a magnetic cryostat with base temperature down to Helium temperature. A superconducting magnet provides magnetic field up to 17 T. Comparing with our domestic Raman setup, selection rules measurements cannot be performed at NHMFL, because the large numerical aperture of the focusing objective tilts the light and causes undesired out-of-plane component of light polarization. The stray magnetic fields

induce Faraday effect in optical components which further contaminates the linearly polarized light.

At Texas Tech University, a 633 nm He-Ne laser is used to match the resonance of CrI_3 and enhances the scattering cross section. A Raman spectrometer (Horiba Labram HR) collects the scattered light. The optical cryostat implemented in this setup can provide a 0 – 7 T magnetic field and liquid Helium temperature. The magnetic field-induced Faraday artifact is eliminated on this setup since we use circularly polarized light.

3.4 Magnetic Interactions in the Spin Hamiltonian

The theoretical tool we use to study the magnetic excitations in quantum magnets is the spin-wave theory, which describes a low energy collective magnetic excitation where the excited spins oscillate collectively near its ground state (Figure 3.3). The notation of "magnon" is equivalent to "spin wave", both of which are used interchangeably in this thesis. The spin wave can be treated with either a semi-classical or a quantum approach. We use the latter approach which we will describe in detail in Section 3.5. Detailed calculations applied to the actual magnets of $Sr_3Ir_2O_7$ and CrI_3 will be given in Chapter 5 and Chapter 6, respectively.

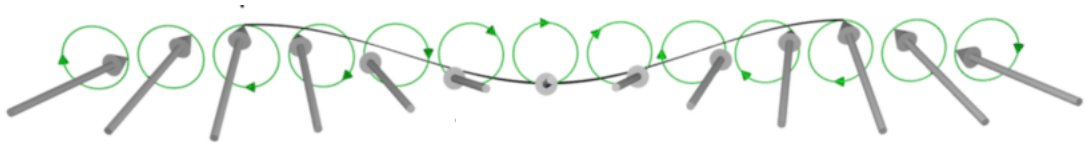

Figure 3.3 Schematics of the spin waves, adapted from Reference [15] with permission.

The first step to perform spin wave calculation is to determine the type of magnetic interactions in the material and construct the spin Hamiltonian. In the following sections, we will introduce several types of magnetic interactions which commonly appear in the spin Hamiltonian.

3.4.1 Magnetic Dipole-Dipole Interaction

Magnetic dipole-dipole interaction is the direct interaction between two magnetic moments through exchange of photons, in analogue to the Coulomb interaction between the electric dipoles. The dipole-dipole interaction has the following form

$$E_{DP} = \frac{\mu}{4\pi|\vec{r}|^3}\left(\vec{m}_1 \cdot \vec{m}_2 - 3(\vec{m}_1 \cdot \vec{r})(\vec{m}_2 \cdot \vec{r})\right) \tag{3.12}$$

where $\vec{m} = \gamma\hbar\vec{S}$ is the magnetic moment of the electron spin, and γ is the gyromagnetic ratio.

Compared to the exchange interaction which will be introduced in Section 3.4.2, magnetic dipole-dipole interaction is magnetic in nature and interacts at a longer range. Generally, the magnetic dipole-dipole interaction tends to align the magnetic moments in the same direction and form ferromagnetic order.

3.4.2 Exchange Interaction

Exchange interaction arises from the Pauli exclusion principle which states that identical fermions cannot occupy the same state and is thus a purely quantum mechanical effect. Because electrons

are fermions with both spin and orbital degrees of freedom, their spin and orbital states are intertwined as the total wavefunction must be antisymmetric under the permutation of two electrons. Therefore, the real-space electronic wavefunction, which is subject to the Coulomb interaction, has a strong influence on the spin configuration.

For simplicity, let's consider a two-electron system which forms either a singlet (total spin $S = 0$) or a triplet ($S = 1$) state [16]. The total spin satisfies

$$\vec{S}^2 = \left(\vec{S}_1 + \vec{S}_2\right)^2 = \frac{3}{2} + 2\vec{S}_1 \cdot \vec{S}_2 \tag{3.13}$$

Because $\vec{S}^2 = 0\ (2)$ for the singlet (triplet) state, $\vec{S}_1 \cdot \vec{S}_2 = -3/4\ (1/4)$ for the singlet (triplet) state. The spin Hamiltonian of the system can be written as

$$H^{spin} = \frac{1}{4}(E_s + 3E_t) - (E_s - E_t)\vec{S}_1 \cdot \vec{S}_2 \tag{3.14}$$

so that $H^{spin} = E_s\ (E_t)$ for the singlet (triplet) state. Omitting the constant energy term, we arrive at the spin Hamiltonian

$$H^{spin} = -J\vec{S}_1 \cdot \vec{S}_2 \tag{3.15}$$

where $J = E_s - E_t$ is the exchange coupling parameter, which is determined by the energy difference between the singlet and triplet state. The singlet (triplet) state has antisymmetric (symmetric) spin so that it has symmetric (antisymmetric) electronic wave function

$$\Psi_{s(t)}(\vec{r}_1, \vec{r}_2) = \frac{1}{\sqrt{2}}\left(\phi_a(\vec{r}_1)\phi_b(\vec{r}_2) \pm \phi_a(\vec{r}_2)\phi_b(\vec{r}_1)\right) \tag{3.16}$$

The different wave function overlap of the singlet and triplet states lead to different Coulomb energy, and thus a difference in E_s and E_t. In an actual solid, we sum over all the magnetic ions which yields the Heisenberg Hamiltonian

$$H^{Heisenberg} = -\sum J_{ij}\vec{S}_i \cdot \vec{S}_j \tag{3.17}$$

If $J_{ij} > 0$, parallel spin alignment is favored and the GS is FM. If $J_{ij} < 0$, the GS is AFM.

The exchange mechanism described above in the two-electron case is the direct exchange. Here several types of exchange interactions are listed.

- Direct exchange arises directly from the Coulomb interaction between the electrons from two magnetic ions. The nonmagnetic ions have no contribution to the exchange interaction in this case.

- Superexchange refers to the case where the nonmagnetic ions mediate the exchange interaction between the magnetic ions. Both the perovskite AFM $Sr_{n+1}Ir_nO_{3n+1}$ (n = 1, 2, ∞) and the layered FM CrI_3 fall into this category. In $Sr_{n+1}Ir_nO_{3n+1}$, the Oxygen ions mediate the superexchange interaction of the Iridium ions of the Ir-O octahedral cage. In CrI_3, the Chromium ions are the magnetic ions and the Iodine ions are the mediators.

- Indirect exchange is mediated through the coupling between the magnetic ions and the surrounding conduction electrons, which typically dominates in partially filled *f*-shell systems.

In Equation 3.17, the exchange interaction of all directions of the magnetic moments are described with a universal J_{ij}, *i.e.*, the Heisenberg Hamiltonian is isotropic. Anisotropic exchange

interactions, on the other hand, are common in real magnets and may lead to interesting magnetism that are under intensive research investigations.

Consider the following spin Hamiltonian:

$$H = -\sum J_{ij}(S_{ix} \cdot S_{jx} + S_{iy} \cdot S_{jy} + \alpha S_{iz} \cdot S_{jz}) \tag{3.18}$$

α measures the anisotropy of the Hamiltonian. If $\alpha > 1$, the spin Hamiltonian in Equation 3.18 becomes the Ising model. The GS of the Ising model is the out-of-plane FM. An example of the Ising magnet is the monolayer FM CrI_3 whose anisotropy counteracts the 2D thermal fluctuations, as discussed in Section 2.3. If $\alpha < 1$, Equation 3.18 becomes the XY model whose GS is the in-plane FM.

DM interaction is another type of interesting anisotropic exchange interaction, which only occurs when the inversion symmetry is broken, such as interface or crystals with no inversion center. It is known as the antisymmetric interaction with the following form

$$H_{ij}^{DM} = \vec{D}_{ij} \cdot (\vec{S}_i \times \vec{S}_j) \tag{3.19}$$

DM interaction causes spin canting in FM or AFM states and is the main driving force of magnetic skyrmions and magnetoelectric effect in multiferroics.

3.4.3 Other Interactions

Single-ion anisotropy, or magnetocrystalline anisotropy, is primarily caused by SOC. It has the following form

$$H^{SIA} = \sum_i A_i S_{iz}^2 \tag{3.20}$$

Zeeman energy is proportional to the external magnetic field

$$H^{Zeeman} = -g\mu_B \sum_i \vec{S}_i \cdot \vec{B} \tag{3.21}$$

The single ion anisotropy and the Zeeman energy are similar in the sense that they both provide an easy axis which the spins tend to align to.

3.5 Spin Hamiltonians of $Sr_3Ir_2O_7$ and CrI_3

In this section we construct the spin Hamiltonians of the two materials $Sr_3Ir_2O_7$ and CrI_3 using the magnetic interactions we previously introduced.

In the case of iridates, the dominating magnetic interaction is the exchange interaction. It is mentioned in Section 2.1 that for Ir^{4+} ion in an Ir-O octahedral cage, the lowest energy states are the Kramer's doublet of total angular momentum $J_{eff} = 1/2$ [17].

In the case of a 180° Ir-O-Ir bond, the superexchange Hamiltonian includes a regular isotropic exchange term, and a special term in the form of a dipole-dipole interaction, namely the pseudodipolar (PD) interaction [17,18].

$$H_{ij} = J_1 \vec{S}_i \cdot \vec{S}_j + J_2 (\vec{S}_i \cdot \vec{r}_{ij})(\vec{S}_j \cdot \vec{r}_{ij}) \tag{3.22}$$

It will be shown in Chapter 5 that this PD exchange interaction is crucial in providing the 92 meV magnetic gap with the special A_{1g} symmetry.

In the family of CrX_3 (X = Cl, Br, I), the spin Hamiltonian consists of the anisotropic exchange interaction which stabilizes *z*-axis or *xy*-plane FM GS, and the Zeeman interaction which induces the external field-induced phase transitions

$$H = -\sum J_{ij}(S_{ix} \cdot S_{jx} + S_{iy} \cdot S_{jy} + \alpha S_{iz} \cdot S_{jz}) - g\mu_B \sum_i \vec{S}_i \cdot \vec{B} \tag{3.23}$$

3.6 Spin-Wave Calculations

The quantum treatment of the spin wave theory uses the Holstein-Primakoff transformations which map the spin operators S_x and S_y to magnon creation b^+ and annihilation b operators [19]

$$\begin{aligned} S^+ &= S_x + iS_y = \sqrt{2S - b^+ b}\, b \\ S^- &= S_x - iS_y = b^+ \sqrt{2S - b^+ b} \end{aligned} \tag{3.24}$$

b^+ and b satisfy the bosonic commutation relations $\left[b_i, b_j^+\right] = \delta_{ij}$. Equation 3.24 assumes that the GS is FM, so that the excitation of a magnon decreases the total spin moment. If the GS is AFM, S^+ and S^- are related to b (b^+) and b^+ (b) on the sites that carry +*z* (-*z*) spins.

Because $\vec{S} \cdot \vec{S} = S(S+1)$, S_z can be computed using Equation 3.24

$$S_z^2 = S(S+1) - S_x^2 - S_y^2 = (S - b^+ b)^2 \tag{3.25}$$

and

$$S_z = S - b^+ b \tag{3.26}$$

It can be verified that S_x, S_y and S_z satisfy the spin commutation relations. Equation 3.26 confirms that the excitation of a magnon decreases the spin moment size.

Although Equation 3.24 preserves the commutation relations of spins, in practice a square root is too complicated to perform computations. Thus we expand Equation 3.24

$$\begin{aligned} S^+ &= \sqrt{2S - b^+ b}\, b = \sqrt{2S}\left(b - \frac{b^+ b b}{4S} + \cdots\right) \\ S^- &= b^+ \sqrt{2S - b^+ b} = \sqrt{2S}\left(b^+ - \frac{b^+ b^+ b}{4S} + \cdots\right) \end{aligned} \tag{3.27}$$

Applying Equation 3.27 to the exchange interaction $\vec{S}_i \cdot \vec{S}_j$, we can see that magnetic problems are correlated by nature, because high order terms of b^+ and b show up. In our work, however, high order terms are neglected which are not significant in spin wave calculations. We thus arrive at the simple form

$$\begin{aligned} S^+ &= \sqrt{2S} b \\ S^- &= \sqrt{2S} b^+ \\ S_z &= S - b^+ b \end{aligned} \tag{3.28}$$

Next, real-space creation and annihilation operators b^+ and b are transformed into $\vec{k}$-space operators a^+ and a.

$$\begin{aligned} a_{\vec{k}} &= \frac{1}{\sqrt{N}} \sum_i e^{-i\vec{k}\cdot\vec{r}_i} b_i \\ a_{\vec{k}}^+ &= \frac{1}{\sqrt{N}} \sum_i e^{i\vec{k}\cdot\vec{r}_i} b_i^+ \end{aligned} \tag{3.29}$$

$\vec{k}$ ($\vec{r}_i$) denotes the momentum (position) of the $\vec{k}$-space (real-space) excitation, and N is the total number of spin sites. It can be verified that a^+ and a also satisfy the bosonic commutation

relations. Combining the highest order approximation of the Holstein-Primakoff transformations and the Fourier transformations, we arrive at Equation 2.5

$$\begin{aligned} S_i^+ &= S_i^x + iS_i^y = \sqrt{\frac{2S}{N}} \sum_{\vec{k}} a_{\vec{k}} e^{i\vec{k}\cdot\vec{r}_i} \\ S_i^- &= S_i^x - iS_i^y = \sqrt{\frac{2S}{N}} \sum_{\vec{k}} a_{\vec{k}}^+ e^{-i\vec{k}\cdot\vec{r}_i} \\ S_i^z &= S - \frac{1}{N} \sum_{\vec{k},\vec{k}'} a_{\vec{k}}^+ a_{\vec{k}'} e^{i(\vec{k}'-\vec{k})\cdot\vec{r}_i} \end{aligned} \tag{3.30}$$

which is ready to be applied to the spin Hamiltonian.

Consider again the nearest neighbor (NN) FM Heisenberg Hamiltonian

$$\begin{aligned} H_{HFM} &= -J \sum_{<i,j>} \vec{S}_i \cdot \vec{S}_j = -J \sum_{<i,j>} [S_{iz}S_{jz} + \frac{1}{2}(S_i^+ S_j^- + S_i^- S_j^+)] \\ &= -\frac{NZJS^2}{2} - JS \sum_{<i,j>} \left(b_i^+ b_j + b_j^+ b_i\right) + JZS \sum_i b_i^+ b_i \\ &= -\frac{NZJS^2}{2} - \frac{JS}{2} \sum_{i,\vec{\delta}} \left(b_i^+ b_{i+\vec{\delta}} + b_{i+\vec{\delta}}^+ b_i\right) + JZS \sum_i b_i^+ b_i \end{aligned} \tag{3.31}$$

$Z = 4$ is the number of NN spins. $\vec{\delta}$ is the position vector $\vec{\delta} = \vec{x}_j - \vec{x}_i$ and the sum is over four NN spin sites. The first term $-NZJS^2/2$ is the GS energy.

We continue to rewrite Equation 3.31 in the $\vec{k}$-space

$$\begin{aligned} H_{HFM} &= -\frac{NZJS^2}{2} + JSZ \sum_{\vec{k},\vec{\delta}} [1 - \frac{1}{Z}\cos\left(\vec{k}\cdot\vec{\delta}\right)] a_{\vec{k}}^+ a_{\vec{k}} \\ H_{HFM} &= -\frac{NZJS^2}{2} + JSZ \sum_{\vec{k},\vec{\delta}} (1 - \gamma_{\vec{k}})\, a_{\vec{k}}^+ a_{\vec{k}} \end{aligned} \tag{3.32}$$

where $\gamma_{\vec{k}} \equiv 1 - 1/Z \cos(\vec{k} \cdot \vec{\delta})$ is determined by the lattice structure. Since now the Halmitonian is diagonal, the energy eigenvalues can be directly read out and the result is shown in Equation 2.7.

A real magnet, however, is often more complicated than the NN FM Heisenberg model, and the spin Hamiltonian is not diagonal. In this case, Bogoliubov transformations for bosonic particles are applied which diagonalize the spin Hamiltonian.

Consider the transformations

$$\begin{aligned} \alpha &= u\beta + v\beta^+ \\ \alpha^+ &= u^*\beta^+ + v^*\beta \end{aligned} \tag{3.33}$$

To preserve the bosonic commutation relations

$$[\alpha, \alpha^+] = [u\beta + v\beta^+, u^*\beta^+ + v^*\beta] = (|u|^2 - |v|^2)[\beta, \beta^+] \tag{3.34}$$

we need the canonical transformation condition $|u|^2 - |v|^2 = 1$. In practice, if we write the spin Hamiltonian in the matrix form

$$H_{HFM} = \begin{pmatrix} a_{\vec{k}}^+ & \cdots & a_{-\vec{k}} \end{pmatrix} \begin{pmatrix} M_{11} & \cdots & M_{1n} \\ \vdots & \ddots & \vdots \\ M_{n1} & \cdots & M_{nn} \end{pmatrix} \begin{pmatrix} a_{\vec{k}} \\ \cdots \\ a_{-\vec{k}}^+ \end{pmatrix} = V^T M V \tag{3.35}$$

finding the Bogoliubov transformations is essentially diagonalizing the matrix *JM*, where *J* is the *n*-dimensional matrix

$$J = \begin{pmatrix} I_{\frac{n}{2}} & 0_{\frac{n}{2}} \\ 0_{\frac{n}{2}} & -I_{\frac{n}{2}} \end{pmatrix} \tag{3.36}$$

where I_n (0_n) is the identity (zero) matrix of dimension n. Detailed calculations applied to perovskite iridates and CrX_3 (X = Cl, Br, I) are given in Chapters 5 and 6. In the next two paragraphs I will briefly introduce the results of those calculations.

In the treatment of the perovskite iridates $Sr_3Ir_2O_7$ and Sr_2IrO_4, the spin Hamiltonian Equation 3.22 includes the exchange couplings and the PD interaction. Polarized Raman spectroscopy shows that the magnetic gap in $Sr_3Ir_2O_7$ carries the A_{1g} symmetry, which is not allowed by a single magnon process. A two-magnon scattering process instead explains both the energy and the symmetry properties of the gap. In addition, the exchange energies turn out to be in perfect agreement with single layer Sr_2IrO_4, indicating the similarity of $Sr_3Ir_2O_7$ and Sr_2IrO_4. The spin wave theory is significant in this study to provide a quantitative explanation that pinpoints the nature of the gap. Detailed calculations will be shown in Chapter 5.

In the study of the magnetic field dependent magnon energies in CrX_3 (X = Cl, Br, I), the spin Hamiltonian Equation 3.23 includes the anisotropic magnetic exchange couplings and a Zeeman term. In the work on CrI_3, two spin Hamiltonians are established assuming either interlayer FM or AFM GS. Comparing the theoretical results of spin wave theory and our Raman data, it is evident that AFM and FM magnons coexist in bulk CrI_3. In the work on the CrX_3 family (X = Cl, Br, I), the anisotropy parameters α are determined for different halogen X, based on the experimental results. Details will be discussed in Chapter 6.

References

[1] C. Raman and K. Krishnan, *The negative absorption of radiation*, Nature **122**, 12 (1928).

[2] A. Smekal, *Zur quantentheorie der dispersion*, Naturwissenschaften **11**, 873 (1923).

[3] C. V. Raman, in *Proceedings of the Indian Academy of Sciences-Section A* (Springer India, 1956), pp. 99.

[4] A. Mooradian and A. McWhorter, *Polarization and intensity of Raman scattering from plasmons and phonons in gallium arsenide*, Physical Review Letters **19**, 849 (1967).

[5] P. Fleury, S. Porto, L. Cheesman, and H. Guggenheim, *Light Scattering by Spin Waves in* FeF_2, Physical Review Letters **17**, 84 (1966).

[6] K. Schmidt, C. Knetter, M. Grüninger, and G. Uhrig, *Charge-Order-Induced Sharp Raman Peak in* $Sr_{14}Cu_{24}O_{41}$, Physical review letters **90**, 167201 (2003).

[7] M. G. Cottam and D. J. Lockwood, *Light scattering in magnetic solids* (Wiley New York, 1986).

[8] S. L. Cooper *et al.*, *Raman scattering as a tool for studying complex materials*, Optical Techniques for Solid-state Materials Characterization, 193 (2011).

[9] W. Hayes and R. Loudon, *Scattering of light by crystals* (Courier Corporation, 2012).

[10] M. S. Dresselhaus, G. Dresselhaus, and A. Jorio, (Springer Berlin, 2008).

[11] V. Heine, *Group theory in quantum mechanics: an introduction to its present usage* (Courier Corporation, 2007).

[12] R. Loudon, *The Raman effect in crystals*, Advances in Physics **13**, 423 (1964).

[13] J. R. Ferraro, *Introductory raman spectroscopy* (Elsevier, 2003).

[14] *User Manual of Dilor XY Modular Laser Raman Spectrometer*.

[15] G. Dieterle *et al.*, *Coherent excitation of heterosymmetric spin waves with ultrashort wavelengths*, Physical review letters **122**, 117202 (2019).

[16] N. W. Ashcroft and N. D. Mermin, (holt, rinehart and winston, new york London, 1976).

[17] G. Jackeli and G. Khaliullin, *Mott insulators in the strong spin-orbit coupling limit: from Heisenberg to a quantum compass and Kitaev models*, Physical review letters **102**, 017205 (2009).

[18] G. Khaliullin, *Orbital order and fluctuations in Mott insulators*, Progress of Theoretical Physics Supplement **160**, 155 (2005).

[19] C. Kittel and C.-y. Fong, *Quantum theory of solids* (Wiley New York, 1963), Vol. 5.

Chapter 4 Raman Scattering of Single- and Bi-Layer Perovskite Iridates

In this chapter, I will discuss the experimental details of our Raman studies on the single-layer and bilayer perovskite iridates Sr_2IrO_4 and $Sr_3Ir_2O_7$, and the electron-doped compounds of $Sr_3Ir_2O_7$. Polarized Raman measurements have been performed on both samples with the setup at the University of Michigan. Magnetic field-dependent data have been collected at NHMFL.

As has been discussed in Chapter 2, RIXS has been the primary experimental technique to study the magnetic excitations of perovskite iridates [1-5]. Although the community has come to a consensus about the Heisenberg AFM nature of the magnetism in Sr_2IrO_4 [1], two distinct models have been proposed for $Sr_3Ir_2O_7$ [2,3], leaving it an open question of the nature of its magnetic GS and excitation. To address this question, we utilize polarized Raman spectroscopy, which has higher energy resolution and can provide additional symmetry information, to probe the magnetic excitations of $Sr_3Ir_2O_7$. We have observed a broad A_{1g} mode at 800 cm^{-1} together with a broad A_{1g} + B_{2g} mode at 1400 cm^{-1}, both of which have been attributed to two-magnon scatterings with our spin-wave theory.

Although different instrument has its own energy resolution, in general the energy resolution of a Raman spectrometer is ~1 cm^{-1} (0.12 meV). The experimental way to determine the energy resolution is to measure the linewidth of the stabilized monochromic laser. Such measurement on our Dilor Raman spectrometer yields a full width at half maximum (FWHM) of ~4 cm^{-1} under our experimental conditions. RIXS, on the other hand, typically has an energy resolution of ~100 meV

[6] and achieving high energy resolution requires building rather large spectrometer [6,7]. Modern high-resolution RIXS spectrometers can resolve the energy down to ~10 meV [7]. Compared to RIXS, Raman spectroscopy has a much higher energy resolution.

Another advantage of Raman spectroscopy is that it has well-defined selection rules. Because the wavelength of visible light (~100 nm) is much longer compared to the lattice constant (~0.1 nm), electric dipole approximation is fully valid and applicable in modeling Raman scattering process. On the contrary, the wavelength of X-ray is comparable to the lattice constant, and higher order multipolar transitions are present in RIXS process [6] which makes the selection rules less well-defined [8].

The above two factors of polarized Raman spectroscopy are crucial in our study of $Sr_3Ir_2O_7$. Firstly, the previous literature proposed that the emergence of the 90 meV magnetic gap observed in RIXS is a first-order process [2,3]. Instead, our study provides key evidence that it is a second-order process [8], where the ultrahigh energy resolution of the Raman technique reveals the lineshape of the mode. First-order processes are normally sharp while second-order processes are generally broad [9-13]. Symmetry information is also important in the determination of the nature of an excitation, as has been discussed in Chapter 3.

4.1 Previous Raman Studies on Sr_2IrO_4 and $Sr_3Ir_2O_7$

We have discussed the advantages of using polarized Raman spectroscopy to study the perovskite iridates. However, we are not the first to use this technique and Raman spectroscopy has been

utilized to study many properties of perovskite iridates. A majority of Raman studies have focused on the pseudospin-lattice coupling in Sr_2IrO_4 [11,14-16], $Sr_{2-x}La_xIrO_4$ [17], and $Sr_3Ir_2O_7$ [11]. Other lattice and electronic properties of perovskites iridates have also been investigated with Raman spectroscopy. The A_{1g} phonon modes near 274 cm^{-1} provide direct indication of the level of lattice distortion [18]. Raman spectrum on Sr_2IrO_4 samples under low [19] and high [20] pressure have shown a pressure-driven first order structural phase transition above 40.6 GPa and a series of phonon anomalies in low-pressure phase which suggest the emergence of a rotation symmetry broken instability and potentially account for the striking persistency of the insulating GS in Sr_2IrO_4, in contrast to cuprates. The symmetry properties of charge order in electron-doped $(Sr_{1-x}La_x)_3Ir_2O_7$ have been revealed with polarized Raman spectroscopy [21]. High-energy electronic transitions with different symmetries in Sr_2IrO_4 are also observed in Raman spectra, placing constraint on the possible theoretical interpretation of the electronic structure [22].

Here we are most interested in the magnetic excitations in perovskite iridates. Both first- [17,23] and second-order [11,17,24] magnons have been reported. Figure 4.1 shows the broad two-magnon continuum in (a) Sr_2IrO_4 and (b) $Sr_3Ir_2O_7$ starting from 1000 cm^{-1} and extending all the way to 3000 cm^{-1} in B_{2g} channel [11]. Figure 4.2 shows the low-energy single magnon excitations of ~10 cm^{-1} in $Sr_{2-x}La_xIrO_4$ which disappear in the metallic phase at high temperature and large La-doping. Magnetic field-dependent studies have also been performed on this single magnon excitation in Sr_2IrO_4 [23]. As Raman scattering probes zero-momentum excitations, the single magnon mode corresponds to the zone-center excitation which appears to be gapless in RIXS [1]. The question arises whether the 92 meV (742 cm^{-1}) magnetic gap [2,3] is also observable in Raman spectroscopy.

A thesis indeed reported a Raman continuum of ~700 cm^{-1} in $Sr_3Ir_2O_7$ (Figure 4.3) which is hypothesized to be a second-order spin flop scattering [25].

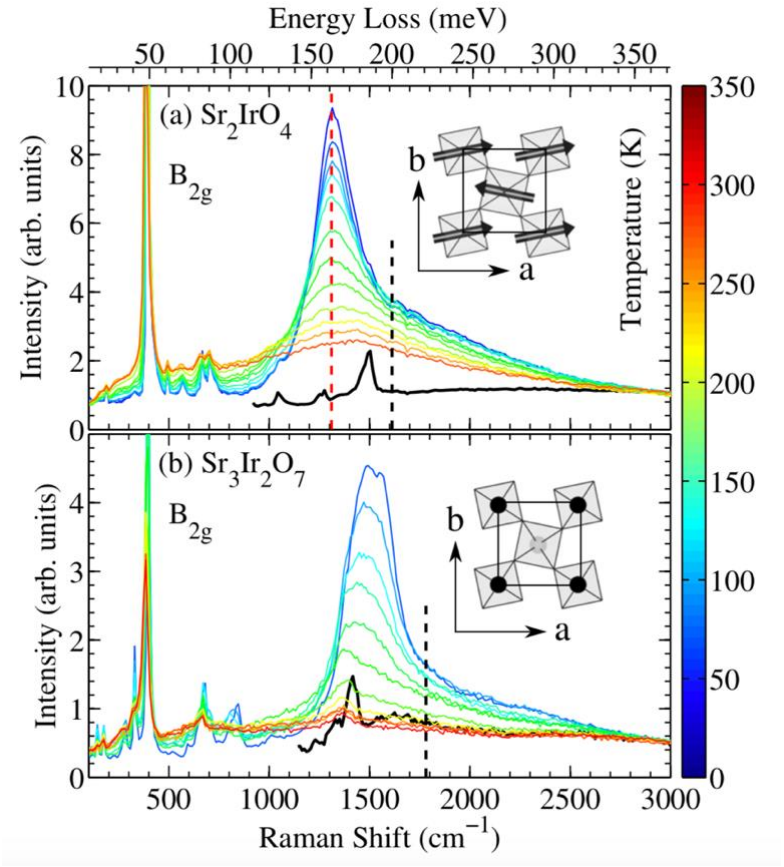

Figure 4.1 Temperature-dependent B_{2g} Raman spectra of (a) Sr_2IrO_4 and (b) $Sr_3Ir_2O_7$ adapted from Reference [11] with permission. The phonon modes are below 1000 cm^{-1}. The two-magnon continuum is above 1000 cm^{-1}.

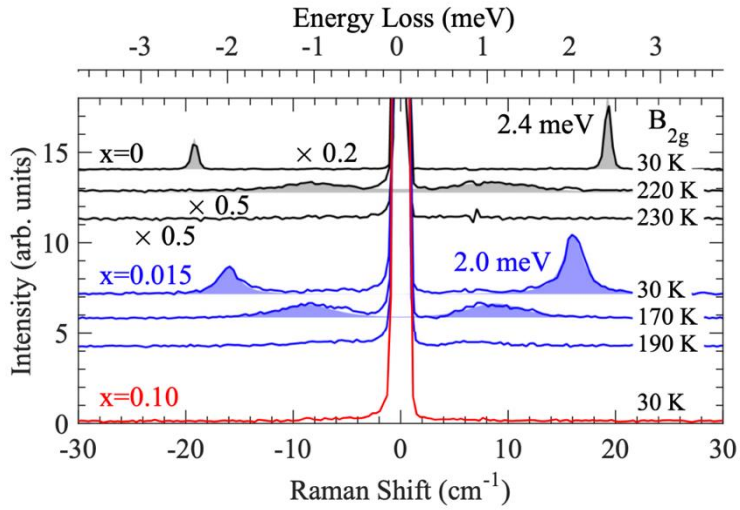

Figure 4.2 Temperature-dependent Raman spectra of $Sr_{2-x}La_xIrO_4$ with both Stokes and anti-Stokes sides in B_{2g} channel. The shaded peaks are the low-energy single-magnon excitations. This figure is adapted from Reference [17] with permission.

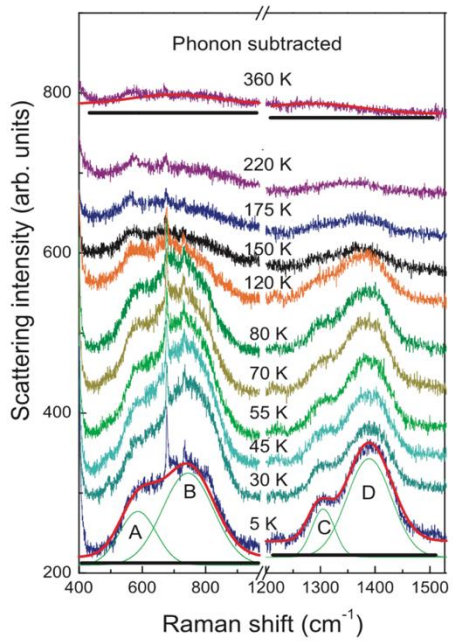

Figure 4.3 Temperature-dependent Raman spectra of $Sr_3Ir_2O_7$ showing both the low energy broad continuum at ~700 cm^{-1} and the two-magnon scattering at ~1400 cm^{-1}. This figure is adapted from Reference [25].

4.2 Experimental Procedure

4.2.1 Sample Preparation

Single crystals of Sr_2IrO_4, $Sr_3Ir_2O_7$, and $(Sr_{1-x}La_x)_3Ir_2O_7$ are grown using flux method [26-28] by research groups at the University of California, Santa Barbara and the University of Colorado, Boulder. They are black opaque crystals with few millimeters lateral dimension and a few hundred microns in thickness. When unused, they are stored in a lab desiccator pumped down to 10^{-1} MPa (using Edwards RV8 Rotary Vane Pump) and dried with molecular sieve desiccant. Each time prior to experiment, the samples are cleaved in the air to expose a clean surface in *xy*-plane.

The sample surface preparation process is different from the normal tape-cleave method, because the bonding force between layers of perovskite iridates are too strong to be cleaved with scotch tapes, so that we elaborate it in this paragraph. We use the top-post cleave method with Torr Seal and aluminum rod. First we grind the aluminum rod so that its face matches the shape of the sample. The rod should be thin at the top so that it stands by itself. Next we glue the rod to the sample top surface and the sample bottom surface to an oxygen-free bronze plate using the Torr Seal and let them stand to dry. The glue should be placed within the sample surface but not extend to the edge, otherwise it will be particularly hard to break from the sample. To speed up the drying process, we may choose to heat up the Torr Seal. After the rod is firmly glued to the sample, it will be broken apart from the sample so that a fresh sample surface is exposed. Microscope images of the sample surface are taken in ambient condition (Figure 4.4). Immediately after taking the photos, the bronze plate with the sample is installed in the cryostat (Janis ST-300) and pumped down to a pressure of 2×10^{-7} mbar (using Pfeiffer Turbo Pumping Station HiCube 80 Eco).

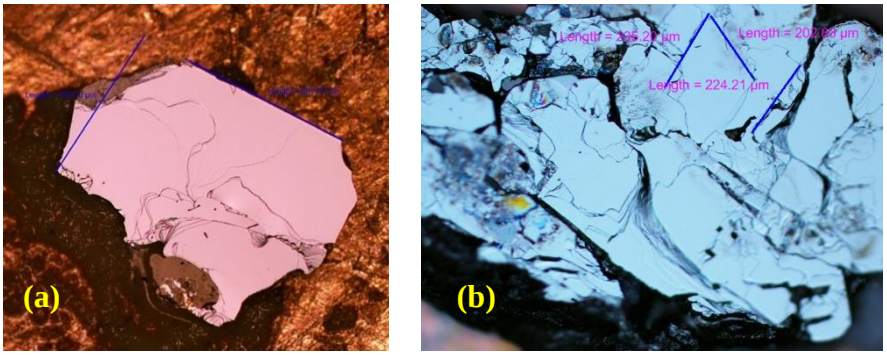

Figure 4.4 A typical microscope image of a cleaved iridate sample. This figure shows the (a) Sr_2IrO_4, (b) $(Sr_{1-x}La_x)_3Ir_2O_7$ (x = 2.25%) sample on the bronze plate. In Panel a, the blue labels are "Length = 735.10/878.57 µm". In Panel b, the magenta labels are "Length = 235.20/202.83/224.21 µm".

4.2.2 Experimental Procedure of Raman Measurements

In this section we discuss the experimental procedures of the Raman experiment. Figure 4.5 shows a photo illustrating the compositions of our actual Raman setup. The incident beam with a power of 1.5 mW is focused to a sample spot of 100 µm. A small mirror (radius = 1/8") directs the incident beam to the sample while blocking the reflected beam. We use a normal incidence and back-scattering geometry. A collecting objective (Nikon 50 mm 1:1.2) collimates the scattered light that passes through the mirror. To maximize the Raman signal, the mirror (radius = 1/8") is as small as the size of the incident beam and the collecting objective has a large NA (1.2).

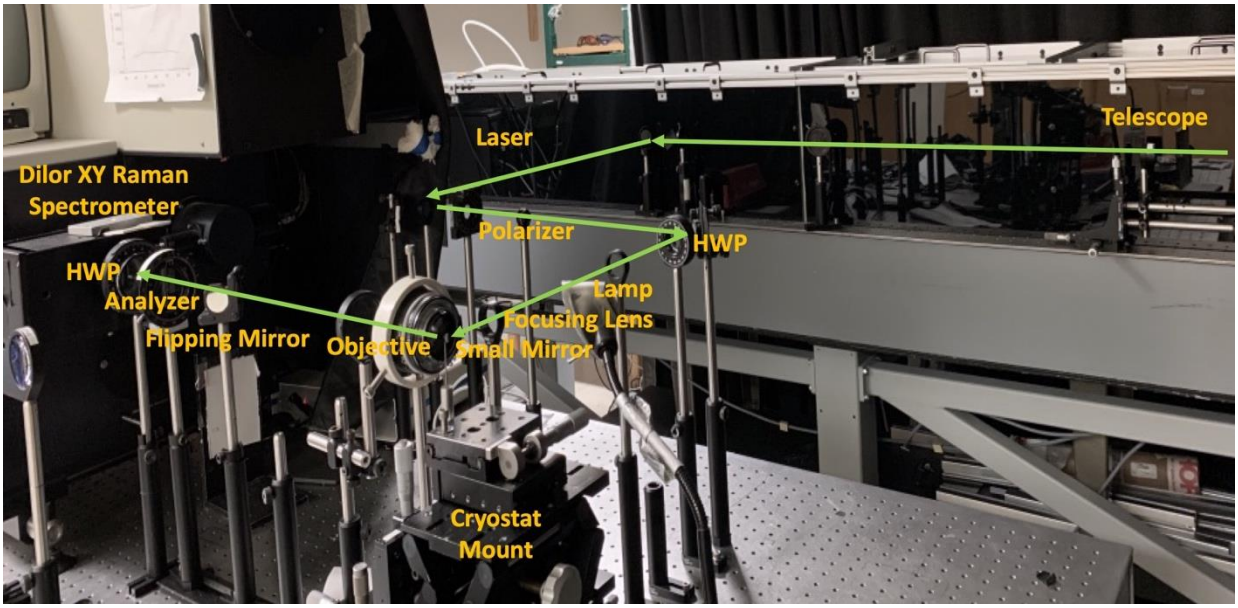

Figure 4.5 Photo showing our real Raman setup at the University of Michigan. Green line marks the beam path. The telescope collimates the incident beam. The lamp and the flipping mirror are used in sample imaging, whose functionalities are illuminating the sample and directing the beam to the imaging camera. The cryostat mount and the objective are equipped with translation stages.

Although the Ar^+ laser is linearly polarized itself, we use a polarizer to rotate it to the vertical polarization and a HWP with azimuth angle φ to rotate its polarization direction to 2φ. In the collection path, a polarizer, namely an analyzer, selects the scattered light with a certain polarization. For example, if we want to select the scattered and incident light with the same polarization direction, the analyzer azimuth angle will be set to 2φ. Another HWP at an angle -φ rotates its linear polarization back to the vertical direction, because the gratings inside the spectrometer are more efficient in transmitting vertically polarized light.

In the collecting path, we have inserted an imaging system to determine the beam size and beam position on the sample. Positioning the beam in the flat region of the sample is crucial for

performing scattering measurements, as cracks can lead to elastically scattered light in the undesired direction that passing through the mirror and reaching the detector. The microscope images have shown that the flat region on the sample is typically of ~100 μm (Figure 4.5 b), comparable to the beam size.

The collecting objective collimates the scattered light before sending it to the spectrometer. The objective is mounted on a 3-axes translation stage. The *z*-axis adjusts the collimation of the beam, while *x*- and *y*-axes adjust the position of the scattered light to maximize the collection efficiency of the spectrometer, which is achieved by focusing the scattered light on the entrance slit of the spectrometer. Real-time images of the entrance slit and the phonon intensities in the Raman spectra are utilized simultaneously to determine the optimal beam location.

Next, we perform a survey of the sample position and look for the optimal spot. Raman spectra of each sample spot is taken at both 290 K and 80 K. The criteria for selecting such a sample spot are as follow. First, the elastic scattering should be low enough so that the low energy feature is clearly visible. Second, the phonon modes should be narrow and intensive. Once the sample spot has been selected, a series of temperature dependent measurements are performed from the liquid helium or nitrogen temperature to room temperature. Because of the design of the cryostat, the sample surface is parallel to the longest dimension of the cryostat. When the temperature is increased, the cryostat undergoes severe thermal expansion and the sample point drifts away. The camera is thus on to keep monitoring the beam position.

4.3 Polarized Raman Spectroscopy of Two-Magnon Scattering in Perovskite Iridates

In this section, we present the temperature-dependent polarized Raman data on various compounds of the perovskite iridate family, including the parent compounds of the single-layer system Sr_2IrO_4 and the bilayer $Sr_3Ir_2O_7$, and the electron-doped bilayer compound $(Sr_{1-x}La_x)_3Ir_2O_7$. We will first discuss the published Raman data of $Sr_3Ir_2O_7$ [8], and then data of the other compounds as a comparison. In $Sr_3Ir_2O_7$, we uncovered two broad Raman modes at 800 cm^{-1} and 1400 cm^{-1}, both of which are explained with a unified two-magnon picture, with the first mode arising from the zone-center optical magnon and the second mode from the zone-boundary magnon. We have further acquired unpublished Raman data which confirmed our two-magnon interpretation. The 800 cm^{-1} mode is absent in Sr_2IrO_4 because of the absence of the optical branch in single-layer Sr_2IrO_4. Raman data in $(Sr_{1-x}La_x)_3Ir_2O_7$ show that the 800 (1400) cm^{-1} modes disappears (dampens) with increasing x out of the AFM insulating phase, confirming their magnetic origin. Field-dependent Raman data show no field response of both modes, consistent with our two-magnon interpretation.

To study the symmetry properties of various modes, we introduce the matrix representation of the Raman tensor and derive the intensity profile in different polarization channels. The perovskite iridate family crystalizes with point group tetragonal D_{4h}. As aforementioned in Section 3.2 that the symmetry of Raman-allowed phonon modes of the D_{4h} point group can be classified with the representations A_{1g}, A_{2g}, B_{1g}, B_{2g}, or E_g. Here we duplicate the standard table of the Raman tensors from References [29,30]. Because A_{2g} mode has an antisymmetric Raman tensor

$\begin{pmatrix} \cdot & b & \cdot \\ -b & \cdot & \cdot \\ \cdot & \cdot & \cdot \end{pmatrix}$, it is associated with magnetic excitations that breaks TRS. Thus A_{2g} is removed in the Raman tensor table typically designed for symmetric phonon modes.

Because we use the normal incidence geometry in the experiment, our probe is sensitive to the *x*- and *y*-components of the tensor elements. The doubly degenerate E_g modes have vanishing *x*- and *y*-components, and are thus not observed in our Raman data. For simplicity, in the following discussions we ignore the *z*-component of the light polarizations or Raman tensors.

Table 4.1 Raman tensors of the D_{4h} point group

$$A_{1g} \quad \begin{pmatrix} a_1 & \cdot & \cdot \\ \cdot & a_1 & \cdot \\ \cdot & \cdot & a_2 \end{pmatrix} \qquad B_{1g} \quad \begin{pmatrix} c & \cdot & \cdot \\ \cdot & -c & \cdot \\ \cdot & \cdot & \cdot \end{pmatrix} \qquad B_{2g} \quad \begin{pmatrix} \cdot & d & \cdot \\ d & \cdot & \cdot \\ \cdot & \cdot & \cdot \end{pmatrix} \qquad E_g \quad \begin{pmatrix} \cdot & \cdot & \cdot \\ \cdot & \cdot & e \\ \cdot & e & \cdot \end{pmatrix} \qquad E_g \quad \begin{pmatrix} \cdot & \cdot & -e \\ \cdot & \cdot & \cdot \\ -e & \cdot & \cdot \end{pmatrix}$$

The scattered light can be decomposed to two components either parallel or perpendicular to the incident light. When the two polarizations are parallel

$$\vec{\epsilon}_S = \vec{\epsilon}_I = (\cos\theta \quad \sin\theta) \tag{4.1}$$

Where $\vec{\epsilon}_S$ *and* $\vec{\epsilon}_I$ are electric field vector of the scattered light and incident light, respectively. θ denotes the angle between electric field vector and crystal axis.

The Raman signal intensity is given by multiplying $\vec{\epsilon}_S$ and $\vec{\epsilon}_I$ with the Raman tensor:

$$
\begin{aligned}
I_{A_{1g}} &\propto \left|\vec{\epsilon}_S \cdot \begin{pmatrix} a_1 & 0 \\ 0 & a_1 \end{pmatrix} \cdot \vec{\epsilon}_I\right|^2 = a_1^2 \\
I_{A_{2g}} &\propto \left|\vec{\epsilon}_S \cdot \begin{pmatrix} 0 & b \\ -b & 0 \end{pmatrix} \cdot \vec{\epsilon}_I\right|^2 = 0 \\
I_{B_{1g}} &\propto \left|\vec{\epsilon}_S \cdot \begin{pmatrix} c & 0 \\ 0 & -c \end{pmatrix} \cdot \vec{\epsilon}_I\right|^2 = c^2 \cos^2 2\theta \\
I_{B_{2g}} &\propto \left|\vec{\epsilon}_S \cdot \begin{pmatrix} 0 & d \\ d & 0 \end{pmatrix} \cdot \vec{\epsilon}_I\right|^2 = d^2 \sin^2 2\theta
\end{aligned}
\tag{4.2}
$$

On the other hand, when the two polarizations are perpendicular:

$$
\begin{aligned}
\vec{\epsilon}_I &\propto (\cos\theta \quad \sin\theta) \\
\vec{\epsilon}_S &\propto (-\sin\theta \quad \cos\theta)
\end{aligned}
\tag{4.3}
$$

Similar to the parallel case, the intensity of each mode is:

$$
\begin{aligned}
I_{A_{1g}} &\propto \left|\vec{\epsilon}_S \cdot \begin{pmatrix} a_1 & 0 \\ 0 & a_1 \end{pmatrix} \cdot \vec{\epsilon}_I\right|^2 = 0 \\
I_{A_{2g}} &\propto \left|\vec{\epsilon}_S \cdot \begin{pmatrix} 0 & b \\ -b & 0 \end{pmatrix} \cdot \vec{\epsilon}_I\right|^2 = b^2 \\
I_{B_{1g}} &\propto \left|\vec{\epsilon}_S \cdot \begin{pmatrix} c & 0 \\ 0 & -c \end{pmatrix} \cdot \vec{\epsilon}_I\right|^2 = c^2 \sin^2 2\theta \\
I_{B_{2g}} &\propto \left|\vec{\epsilon}_S \cdot \begin{pmatrix} 0 & d \\ d & 0 \end{pmatrix} \cdot \vec{\epsilon}_I\right|^2 = d^2 \cos^2 2\theta
\end{aligned}
\tag{4.4}
$$

Based on equation (4.3) and (4.4), we plot I vs θ in polar coordinates in Table 4.2.

From Table 4.2 it is clear that if the polarizations of the scattered and incident light are parallel and both aligned to (45° relative to) the crystal axes, both A_{1g} and B_{1g} (B_{2g}) modes will achieve their maximum intensity. If the polarizations of the scattered and incident light are perpendicular and aligned to (45° relative to) the crystal axes, B_{2g} (B_{1g}) modes will achieve their intensity

maximum, respectively. The correspondence between polarization channels and active Raman modes is summarized explicitly in Table 4.3.

Table 4.2 Polar plots of the Raman intensities of the scattered light parallel/cross to the incident light of different symmetry-allowed modes

	A_{1g}	B_{1g}	B_{2g}
Parallel	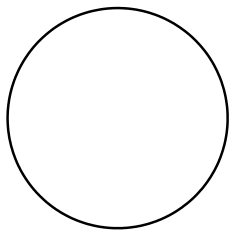	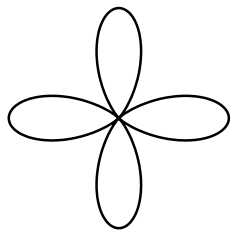	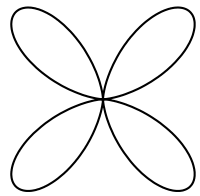
Cross	NA	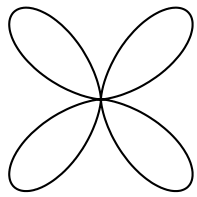	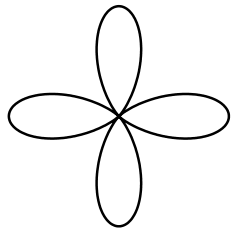

Table 4.3 Raman-accessible symmetry channels under different polarization geometries. The black (gray) arrow denotes the polarization of the incident (scattered) light. The third row shows the notations of the four geometries that will be used in this thesis.

		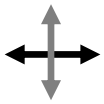	
$A_{1g} + B_{1g}$	$A_{1g} + B_{2g}$	B_{2g}	B_{1g}
Parallel 0°	Parallel 45°	Cross 0°	Cross 45°

4.3.1 Results on the Bilayer Perovskite Iridate $Sr_3Ir_2O_7$

In this section, we present our Raman data on the bilayer perovskite iridate $Sr_3Ir_2O_7$. First we discuss two datasets taken above or below the AFM onset temperature T_N = 230 K. Figure 4.6 shows the low- and high-temperature Raman spectra measured in the parallel 45° geometry. This geometry can detect most of the Raman modes in perovskite iridates, as will be discussed later in this section (Figure 4.6). Several features in the dataset at 80 K are marked with symbols ∗, ◊, and O. The low-energy sharp peaks marked with symbol ∗ are phonon modes and consistent with previous reports [11,21]. They are present both above and below T_N. On the high-energy side there are two broad features marked with ◊ and O. Asymmetric peak O is greatly enhanced below T_N. and has been attributed to two-magnon scattering [11]. Feature ◊ only emerges below T_N, which strongly indicates its magnetic origin. Interestingly, it is centered at an energy of ~800 cm^{-1} (99 meV), comparable to the magnetic gap observed in RIXS [2].

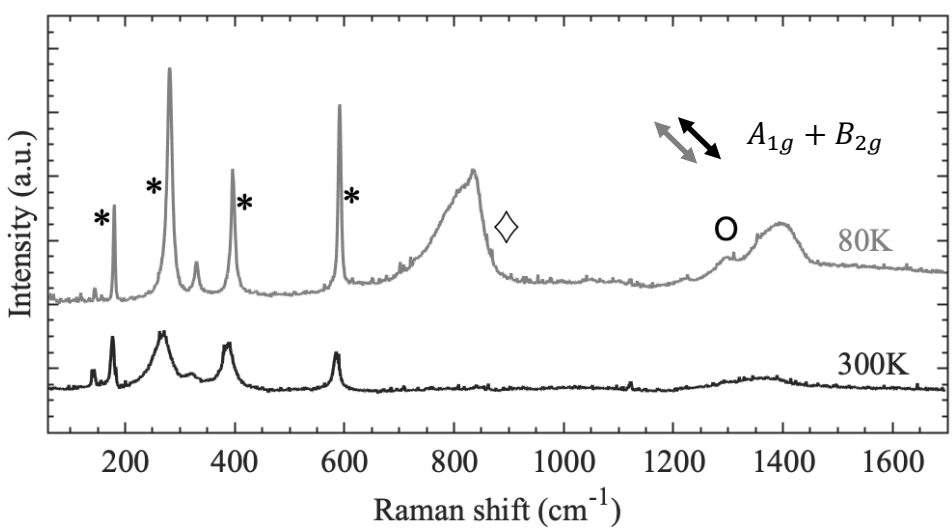

Figure 4.6 Comparison of the low- and high-temperature Raman spectra across T_N. This data is collected in the parallel 45° geometry.

To confirm the magnetic origin of feature ◊, detailed temperature dependent measurements from helium temperature to room temperature have been performed (shown in Figure 4.7). The two broad magnetic features are shaded with dark and light grey color. To acquire quantitative knowledge of the two modes, we extract their integrated intensity (Figure 4.8 a) and central energy (Figure 4.8 b) as a function of the temperature. Because we are unsure of the functional forms of both continuum, the data points in Figure 4.8 are not acquired from curve fitting. Instead, the integrated intensity is the shaded area above the background noise with the intensity of the 593 cm^{-1} phonon subtracted and its error bar defined by square root of the number of data points within the integral times the standard deviation of a single data point. The Raman shift is the maximum of the intensity continuum, with its error bar being the width above 0.99 times maximal intensity. As shown in Figure 4.8 a, the integrated intensities of both modes have a steep increase below 230 K, which is consistent with the AFM onset temperature measured with resonant X-ray diffraction [31]. In addition, both modes show softening behavior towards the transition temperature (Figure 4.8 b). We thus confirm the magnetic nature of both modes.

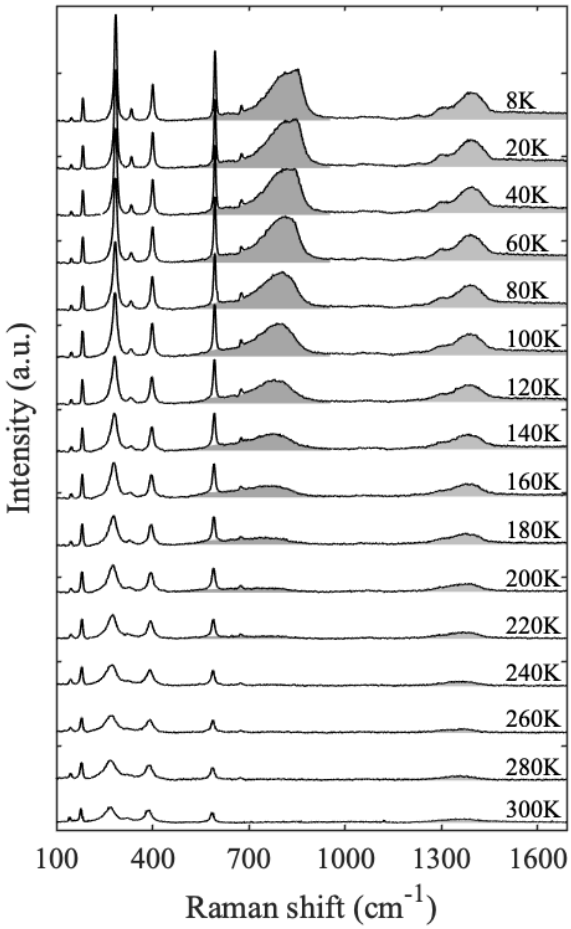

Figure 4.7 Temperature-dependent unpolarized Raman data of $Sr_3Ir_2O_7$ from 8 K to 300 K in steps of 20 K, adapted from Reference [8].

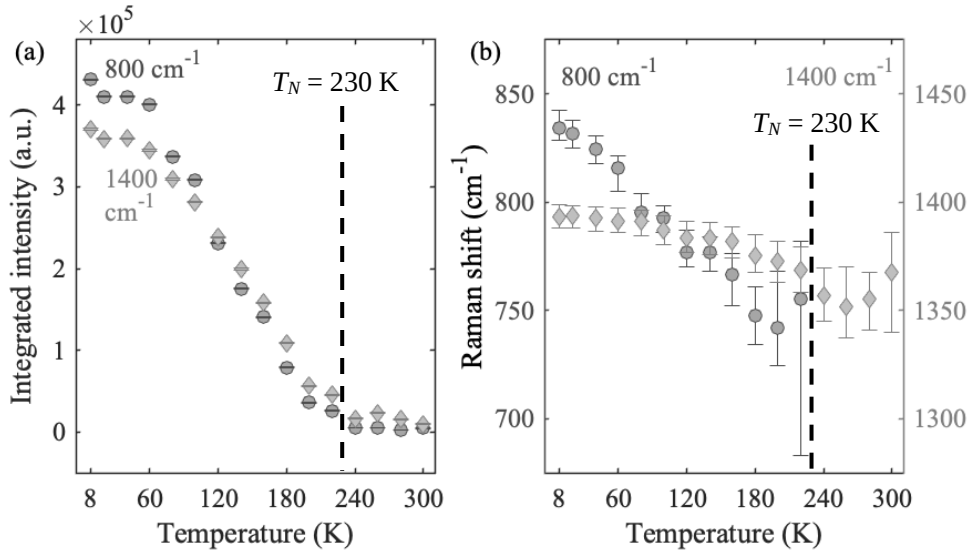

Figure 4.8 (a) Integrated intensity and (b) Raman shift as a function of temperature of both magnetic continuum at 800 (dark grey) and 1400 cm^{-1} (light grey), adapted from Reference [8]. The dashed line marks the AFM onset temperature T_N = 230 K.

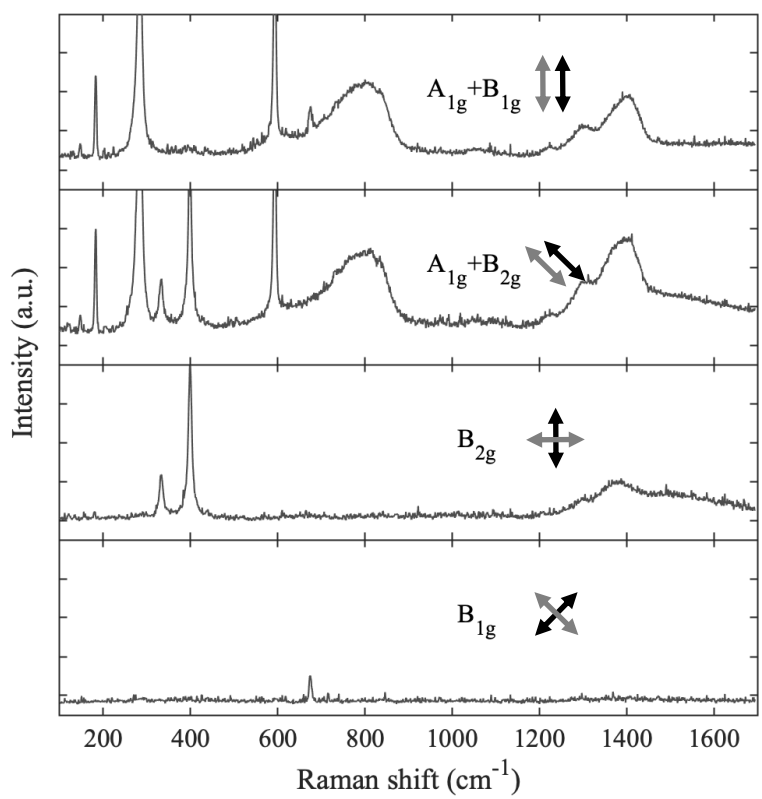

Figure 4.9 Selection rule measurements of $Sr_3Ir_2O_7$ at 80 K, adapted from Reference [8].

To gain further insight of the nature of the feature ◊, we perform selection rule measurements, as shown in Figure 4.9, in the four polarization geometries listed in Table 4.3. Panels 3 and 4 plot the Raman spectra with a single symmetry channel B_{2g} and B_{1g}. Subtracting Panel 1 with Panel 4 yields the Raman modes of symmetry A_{1g}.

Clearly, the phonon modes at 122 cm^{-1}, 147 cm^{-1}, 183 cm^{-1}, 283 cm^{-1}, and 593 cm^{-1} belong to A_{1g} representation. The phonon modes at 334 cm^{-1} and 399 cm^{-1} are of B_{2g} symmetry. There is only one B_{1g} phonon mode at 674 cm^{-1}. The assignment of the phonon symmetries agrees with the previous literature [11]. The two-magnon scattering at 1400 cm^{-1} shows up in both A_{1g} and B_{2g} channels, with its majority in A_{1g} channel. The broad feature at 800 cm^{-1} which has been attributed to a magnetic excitation, surprisingly open be present in the fully symmetric A_{1g} channel.

The broad line shape together with the A_{1g} symmetry of the 800 cm^{-1} feature rules out the possibility of a single magnon excitation. To understand the mechanism of this peculiar mode, we construct a minimal spin model with the exchange interactions and a pseudodipolar interaction, whose results perfectly match the experiment observations. Using the standard spin wave theory, we show that both the 800 cm^{-1} and the 1400 cm^{-1} features arise from two-magnon scattering. The 1400 cm^{-1} mode comes from the traditional zone-boundary two-magnon scattering. The 800 cm^{-1} mode, on the other hand, arises from two-magnon scattering of the gapped zone-center optical magnon. Details of this calculation will be given in Chapter 5.

Let us refer back to the temperature dependence of both two-magnon scattering modes. The 800 cm^{-1} two-magnon mode vanishes while the 1400 cm^{-1} two-magnon mode persists above T_N (Figure

4.7 and Figure 4.8 a). The reason of this discrepancy is as follows [11,32]. Although the 3D AFM order disappears above T_N, quasi-2D spin-spin correlation still exists. Because optical two-magnon mode arise from interlayer coupling, it vanishes as soon as 3D AFM disappears. Zone-boundary two-magnon mode results from in-plane AFM, so that it persists above T_N.

4.3.2 Results on the Single-Layer Perovskite Iridate Sr_2IrO_4

In the following two sections, we present our Raman results on the single-layer compound Sr_2IrO_4 and the electron-doped bilayer compounds $(Sr_{1-x}La_x)_3Ir_2O_7$, and compare them with the bilayer parent compound $Sr_3Ir_2O_7$. Although these data have not been published, they are in good agreement with our two-magnon scattering interpretation of both Raman modes.

We summarize the Raman data collected on Sr_2IrO_4 under all four polarization geometries in Figure 4.10, with Panel a/b taken at 80/290 K, respectively. Only one phonon mode at 691 cm^{-1} shows up in the B_{1g} channel, similar to $Sr_3Ir_2O_7$. The B_{2g} phonon mode at 393 cm^{-1} and the A_{1g} phonon modes at 185 cm^{-1}, 278 cm^{-1} and 562 cm^{-1} which appear in $Sr_3Ir_2O_7$ are also present. However, the lower energy side peaks of the B_{2g} phonon mode at 393 cm^{-1} and the A_{1g} phonon mode at 185 cm^{-1} are missing, indicating that those side peaks arise from interlayer lattice vibrations. In addition to the phonon modes below 700 cm^{-1} which have been observed in $Sr_3Ir_2O_7$, several peaks show up around 800 cm^{-1} which have been attributed to phonons [24]. Interestingly, there is a broad A_{1g} mode centered at 847 cm^{-1}, close to the low-energy two-magnon feature observed in $Sr_3Ir_2O_7$. However, this mode is also present at room temperature. Thus it is assigned to a phonon mode rather than a magnetic scattering.

At high energy, we again observe the broad two-magnon scattering at 1470 cm^{-1} in both A_{1g} and B_{2g} channels, similar to $Sr_3Ir_2O_7$. However, the two-magnon peak at 800 cm^{-1} is absent. This result is consistent our theoretical model, as the optical magnon branch only exists in the bilayer compound $Sr_3Ir_2O_7$.

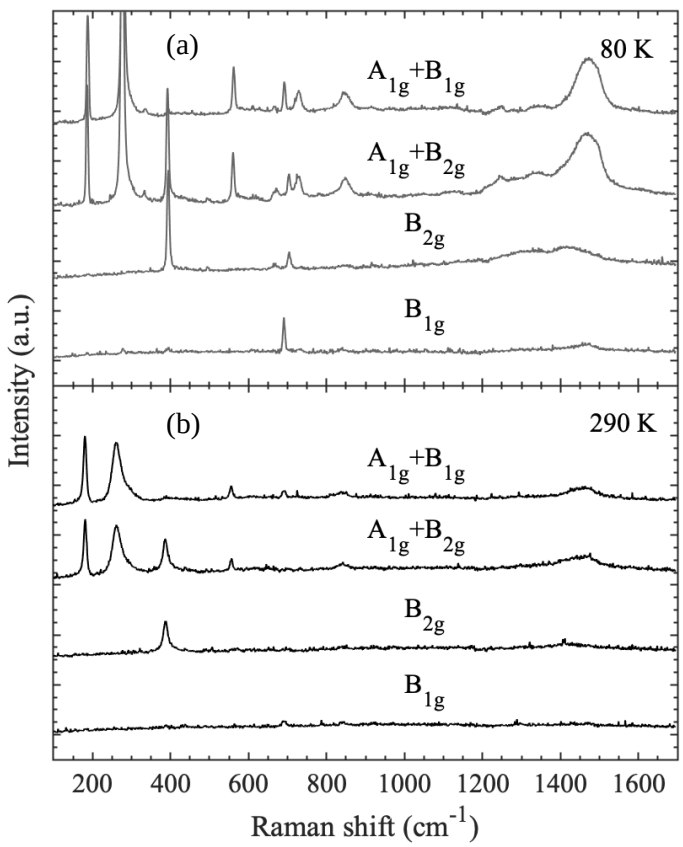

Figure 4.10 Polarized Raman data of Sr_2IrO_4, taken at (a) 80 K, and (b) 290 K.

4.3.3 Results on the Electron-Doped Bilayer Perovskite Iridate $(Sr_{1-x}La_x)_3Ir_2O_7$

As we have introduced in Chapter 2, the La-doped $(Sr_{1-x}La_x)_3Ir_2O_7$ undergoes an IMT at x_c = 4%. To characterize this interesting transition, we performed Raman measurements on a series of compounds with various La-doping level x = 2.25%, x = 3.6%, and x = 6.7%. The x = 2.25% compound retains the AFM GS, while x = 3.6% compound falls on the edge of the IMT, and the x = 6.7% compound is paramagnetic (PM). We thus expect the two-magnon scattering to vanish with increasing La-doping.

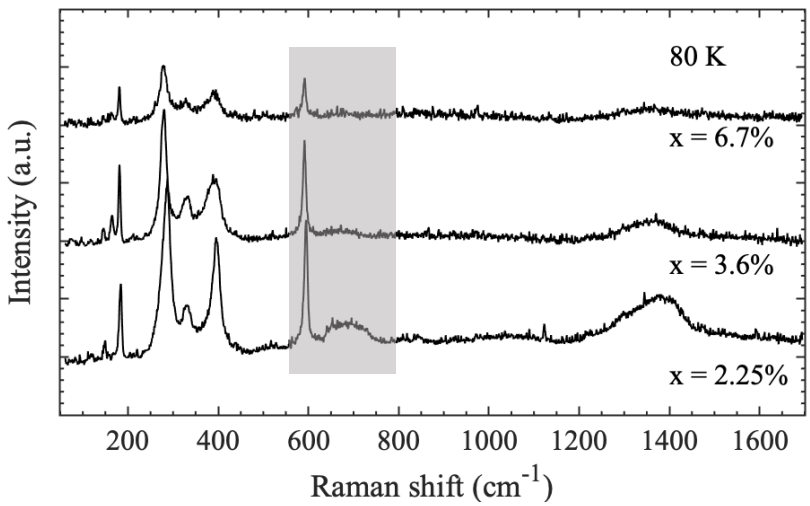

Figure 4.11 Doping dependent Raman spectra of $(Sr_{1-x}La_x)_3Ir_2O_7$ taken in the parallel 45° polarization geometry (A_{1g} + B_{2g}) at 80 K. The shaded area highlights the zone-center two-magnon mode at ~800 cm^{-1}.

The Raman data of $(Sr_{1-x}La_x)_3Ir_2O_7$ taken at 80 K in the A_{1g} + B_{2g} geometry are plotted in Figure 4.11 with the region around 800 cm^{-1} highlighted. As expected, the zone-center two-magnon scattering peak gradually disappears as the electron doping destroys the AFM order. It is greatly damped but clearly visible in the x = 2.25% compound, while hardly visible in the x = 3.6%

compound and vanishes in the x = 6.7% compound. The zone-boundary two-magnon scattering at 1400 cm^{-1}, on the other hand, persists into the PM phase, similar to the results in the parent compound (Figure 4.7).

4.3.4 Magnetic Field-Dependent Raman Spectroscopy of Sr_2IrO_4 and $Sr_3Ir_2O_7$

We performed unpolarized field-dependent Raman measurements on both Sr_2IrO_4 and $Sr_3Ir_2O_7$ up to 17 T at the NHMFL. Despite their magnetic origin, the two-magnon scatterings of both compounds display no observable field dependence, as shown in Figure 4.12 bd. The relative intensities of the phonons differ from the data taken at the University of Michigan, because an excitation wavelength of 532 nm is used at the NHMFL.

There are several reasons that the two-magnon modes show no response to external magnetic field. The characteristic energy scale of magnetic field response is given by $g\mu_B B$, where g is the g-factor and μ_B is the Bohr magneton. With $B = 17$ T, the energy is on the order of 1 meV, or 10 cm^{-1}. This energy is too small to perturb the AFM GS whose exchange interaction is 458 cm^{-1} (details given in Chapter 5). It is also negligible compared to the energy scale of the two-magnon scatterings of 800 and 1400 cm^{-1}.

Another reason lies in the scattering mechanism of two-magnon scattering of an AFM compound [10]. The zone-center two-magnon scattering can be classified with its net magnetic moment and parity

$$
\begin{aligned}
|J_z = 2, \text{Parity} +\rangle &= |\uparrow \vec{k}, \uparrow -\vec{k}\rangle \\
|J_z = 0, \text{Parity} +\rangle &= |\uparrow \vec{k}, \downarrow -\vec{k}\rangle + |\downarrow \vec{k}, \uparrow -\vec{k}\rangle \\
|J_z = 0, \text{Parity} -\rangle &= |\uparrow \vec{k}, \downarrow -\vec{k}\rangle - |\downarrow \vec{k}, \uparrow -\vec{k}\rangle \\
|J_z = -2, \text{Parity} +\rangle &= |\downarrow \vec{k}, \downarrow -\vec{k}\rangle
\end{aligned}
\tag{4.5}
$$

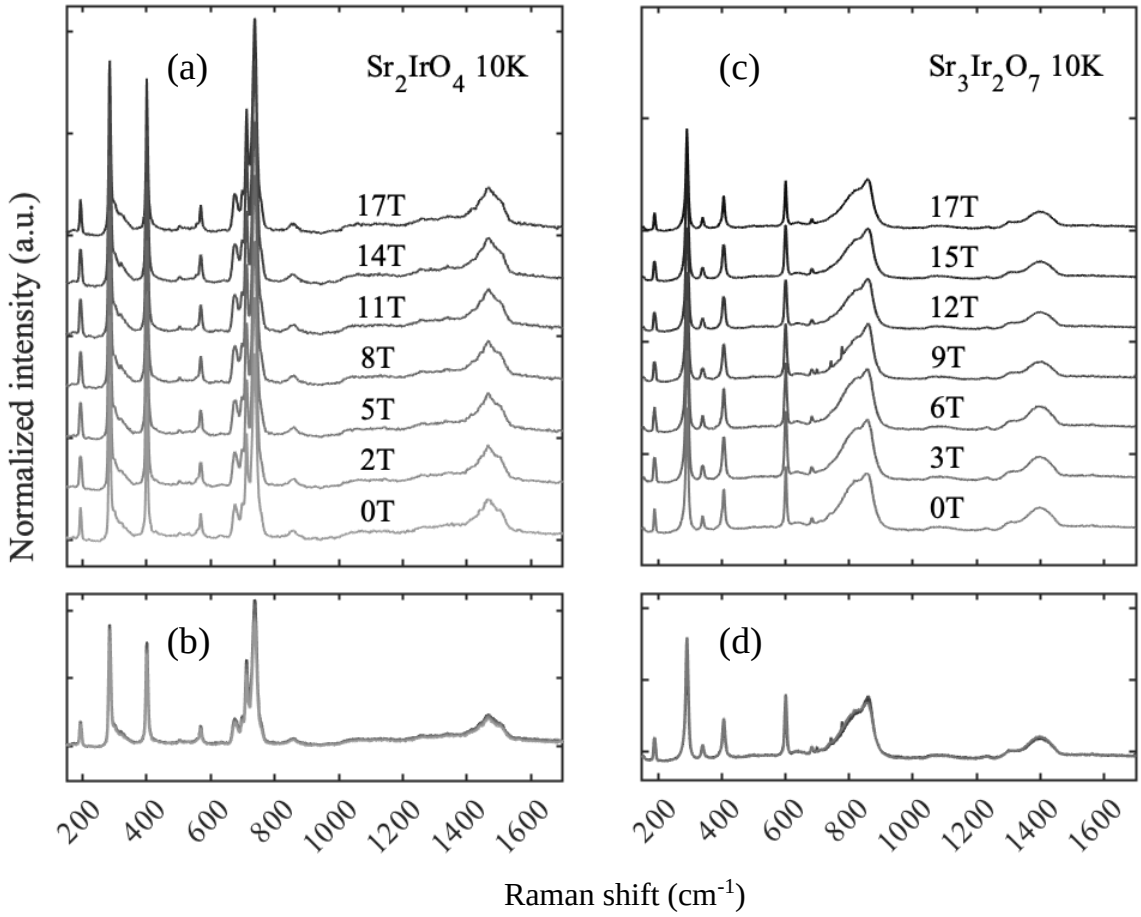

Figure 4.12 Unpolarized Raman spectra of (a) (b) Sr_2IrO_4 and (c) (d) $Sr_3Ir_2O_7$ under external magnetic field at 10 K. (a) (c) Individual spectra from 0 T to 17 T. (b) (d) The spectra in (a) (c) plotted with the same base level.

The parity – state is active in optical absorption rather than Raman scattering. The $|J_z = \pm 2, \text{Parity} +\rangle$ states excite mainly one sublattice of the AFM state, while the $|J_z = 0, \text{Parity} +\rangle$ state excite both sublattices. Because the two-magnon scattering is coupled through the electronic exchange interactions connecting neighboring spin sites, the dominating

two-magnon scattering is the $|J_z = 0, \text{Parity} +\rangle$ state which is expected to have no response to external magnetic fields.

4.4 Single Magnon Excitations in Perovskite Iridates

It is worth mentioning the magnetic excitation at ~10 cm^{-1} observed in Sr_2IrO_4 (Figure 4.2) [17,23]. This low-energy mode with a narrow linewidth is attributed to a single magnon excitation in the previous literature. On the one hand, it experiences mode softening and damping with increasing temperature [23] and electron doping [17,23] towards the critical point. On the other hand, its energy responds strongly to external magnetic field [23]. Its low energy is consistent with the fact that magnon band in Sr_2IrO_4 appears to be gapless in RIXS measurements [1]. However, this mode shows up in the B_{2g} symmetry channel [17] rather than the cross A_{2g} channel, which is yet not understood with the standard selection rule analysis of first-order magnetic excitation introduced in Section 3.2.

In $(Sr_{1-x}La_x)_3Ir_2O_7$, theoretically it is predicted that it hosts both the low-energy acoustic single magnon and the finite-energy optical single magnon in the parent and electron-doped compounds. However, no such single magnon Raman scattering on the low-energy side has been observed so far with a narrow linewidth and strong magnetic field dependence. In over-doped $(Sr_{1-x}La_x)_3Ir_2O_7$, a low-energy narrow mode of ~26 cm^{-1} emerges, however, in the metallic phase [21], which has been reported in Reference [33] and is attributed to CDW instability.

References

[1] J. Kim *et al.*, *Magnetic excitation spectra of Sr_2IrO_4 probed by resonant inelastic X-ray scattering: establishing links to cuprate superconductors*, Physical Review Letters **108**, 177003 (2012).

[2] J. Kim *et al.*, *Large spin-wave energy gap in the bilayer iridate $Sr_3Ir_2O_7$: Evidence for enhanced dipolar interactions near the mott metal-insulator transition*, Physical review letters **109**, 157402 (2012).

[3] M. M. Sala *et al.*, *Evidence of quantum dimer excitations in $Sr_3Ir_2O_7$*, Physical Review B **92**, 024405 (2015).

[4] T. Hogan, R. Dally, M. Upton, J. Clancy, K. Finkelstein, Y.-J. Kim, M. Graf, and S. D. Wilson, *Disordered dimer state in electron-doped $Sr_3Ir_2O_7$*, Physical Review B **94**, 100401 (2016).

[5] X. Lu, D. McNally, M. M. Sala, J. Terzic, M. Upton, D. Casa, G. Ingold, G. Cao, and T. Schmitt, *Doping Evolution of Magnetic Order and Magnetic Excitations in $(Sr_{1-x}La_x)_3Ir_2O_7$*, Physical review letters **118**, 027202 (2017).

[6] L. J. Ament, M. Van Veenendaal, T. P. Devereaux, J. P. Hill, and J. Van Den Brink, *Resonant inelastic x-ray scattering studies of elementary excitations*, Reviews of Modern Physics **83**, 705 (2011).

[7] A. Q. Baron, *Introduction to high-resolution inelastic x-ray scattering*, arXiv preprint arXiv:1504.01098 (2015).

[8] S. Li *et al.*, *Symmetry-resolved two-magnon excitations in a strong spin-orbit-coupled bilayer antiferromagnet*, Physical Review Letters **125**, 087202 (2020).

[9] P. Mishra and K. Jain, *First-and second-order Raman scattering in nanocrystalline silicon*, Physical Review B **64**, 073304 (2001).

[10] P. Fleury and R. Loudon, *Scattering of light by one-and two-magnon excitations*, Physical Review **166**, 514 (1968).

[11] H. Gretarsson, N. Sung, M. Höppner, B. Kim, B. Keimer, and M. Le Tacon, *Two-magnon Raman scattering and pseudospin-lattice interactions in Sr_2IrO_4 and $Sr_3Ir_2O_7$*, Physical review letters **116**, 136401 (2016).

[12] G. Blumberg, P. Abbamonte, M. Klein, W. Lee, D. Ginsberg, L. Miller, and A. Zibold, *Resonant two-magnon Raman scattering in cuprate antiferromagnetic insulators*, Physical Review B **53**, R11930 (1996).

[13] G. Blumberg, R. Liu, M. Klein, W. Lee, D. Ginsberg, C. Gu, B. Veal, and B. Dabrowski, *Two-magnon Raman scattering in cuprate superconductors: Evolution of magnetic fluctuations with doping*, Physical Review B **49**, 13295 (1994).

[14] F. Ye, C. Hoffmann, W. Tian, H. Zhao, and G. Cao, *Pseudospin-lattice coupling and electric control of the square-lattice iridate Sr_2IrO_4*, Physical Review B **102**, 115120 (2020).

[15] K. Samanta, D. Rigitano, P. Pagliuso, and E. Granado, *Isospin-phonon coupling and Fano-interference in spin-orbit Mott insulator Sr_2IrO_4*, Applied Physics Letters **114**, 152402 (2019).

[16] H. S. Kunwar, V. Dwij, B. K. De, S. Rana, S. Tyagi, G. Sharma, A. K. Rathore, and V. Sathe, in *AIP Conference Proceedings* (AIP Publishing LLC, 2020), p. 030564.

[17] H. Gretarsson, J. Sauceda, N. Sung, M. Höppner, M. Minola, B. Kim, B. Keimer, and M. Le Tacon, *Raman scattering study of vibrational and magnetic excitations in $Sr_{2-x}La_xIrO_4$*, Physical Review B **96**, 115138 (2017).

[18] N. Sung, H. Gretarsson, D. Proepper, J. Porras, M. Le Tacon, A. Boris, B. Keimer, and B. Kim, *Crystal growth and intrinsic magnetic behaviour of Sr_2IrO_4*, Philosophical Magazine **96**, 413 (2016).

[19] K. Samanta, F. Ardito, N. Souza-Neto, and E. Granado, *First-order structural transition and pressure-induced lattice/phonon anomalies in Sr_2IrO_4*, Physical Review B **98**, 094101 (2018).

[20] C. Chen *et al.*, *Persistent insulating state at megabar pressures in strongly spin-orbit coupled Sr_2IrO_4*, Physical Review B **101**, 144102 (2020).

[21] W. Jin *et al.*, *Polarized Raman spectroscopy study of metallic $(Sr_{1-x}La_x)_3Ir_2O_7$: A consistent picture of disorder-interrupted unidirectional charge order*, Physical Review B **99**, 041109 (2019).

[22] J.-A. Yang, Y.-P. Huang, M. Hermele, T. Qi, G. Cao, and D. Reznik, *High-energy electronic excitations in Sr_2IrO_4 observed by Raman scattering*, Physical Review B **91**, 195140 (2015).

[23] Y. Gim, A. Sethi, Q. Zhao, J. Mitchell, G. Cao, and S. Cooper, *Isotropic and anisotropic regimes of the field-dependent spin dynamics in Sr_2IrO_4: Raman scattering studies*, Physical Review B **93**, 024405 (2016).

[24] M. F. Cetin, P. Lemmens, V. Gnezdilov, D. Wulferding, D. Menzel, T. Takayama, K. Ohashi, and H. Takagi, *Crossover from coherent to incoherent scattering in spin-orbit dominated Sr_2IrO_4*, Physical Review B **85**, 195148 (2012).

[25] M. F. Cetin, *Light scattering in spin orbit coupling dominated systems*, (2012).

[26] M. Subramanian, M. Crawford, and R. Harlow, *Single crystal structure determination of double layered strontium iridium oxide [$Sr_3Ir_2O_7$]*, Materials research bulletin **29**, 645 (1994).

[27] C. Dhital *et al.*, *Spin ordering and electronic texture in the bilayer iridate $Sr_3Ir_2O_7$*, Physical Review B **86**, 100401 (2012).

[28] G. Cao, J. Bolivar, S. McCall, J. Crow, and R. Guertin, *Weak ferromagnetism, metal-to-nonmetal transition, and negative differential resistivity in single-crystal Sr_2IrO_4*, Physical Review B **57**, R11039 (1998).

[29] R. Loudon, *The Raman effect in crystals*, Advances in Physics **13**, 423 (1964).

[30] W. Hayes and R. Loudon, *Scattering of light by crystals* (Courier Corporation, 2012).

[31] S. Boseggia, R. Springell, H. Walker, A. Boothroyd, D. Prabhakaran, D. Wermeille, L. Bouchenoire, S. Collins, and D. McMorrow, *Antiferromagnetic order and domains in $Sr_3Ir_2O_7$ probed by X-ray resonant scattering*, Physical Review B **85**, 184432 (2012).

[32] B. Muschler *et al.*, *Electron interactions and charge ordering in CuO_2 compounds*, The European Physical Journal Special Topics **188**, 131 (2010).

[33] H. Chu, L. Zhao, A. de la Torre, T. Hogan, S. Wilson, and D. Hsieh, *A charge density wave-like instability in a doped spin–orbit-assisted weak Mott insulator*, Nature materials **16**, 200 (2017).

Chapter 5 Two-Magnon Calculations of $Sr_3Ir_2O_7$

5.1 Previous Studies on the Magnetism of Sr_2IrO_4 and $Sr_3Ir_2O_7$

5.1.1 The Spin-Wave Model of La_2CuO_4 and Sr_2IrO_4

As introduced in Chapter 2, single-layer perovskite iridate Sr_2IrO_4 has been shown to be analogue to the high-T_C SC cuprate La_2CuO_4, where both compounds hold a 2D Heisenberg AFM with in-plane magnetic moments.

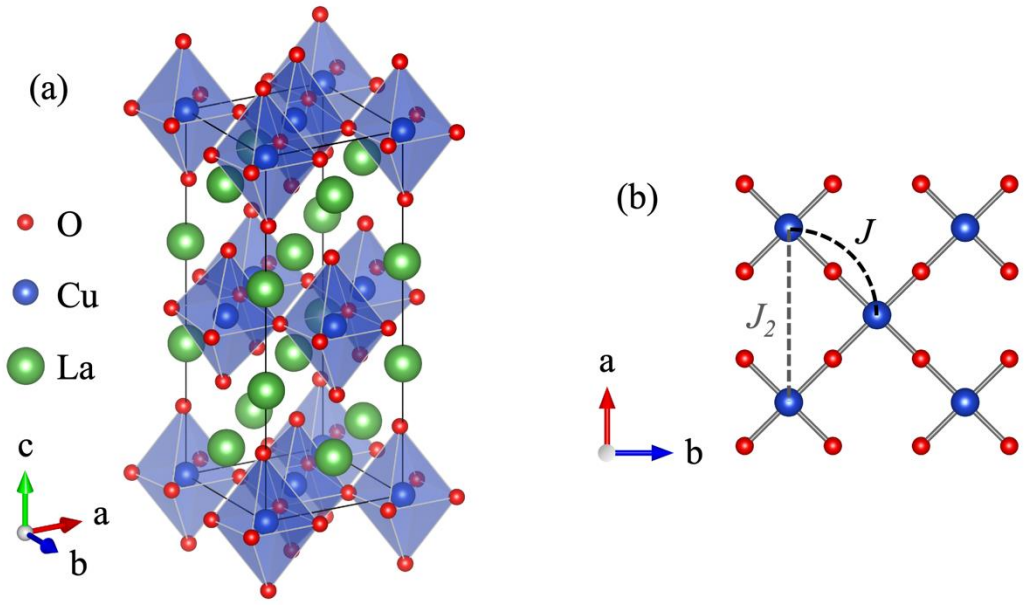

Figure 5.1 (a) The crystal structure of La_2CuO_4. (b) The Cu-O_2 plane viewed from the *c*-axis. *J* and J_2 are the NN and second-NN exchange interactions.

The crystal structure of La_2CuO_4 is the tetragonal D_{4h} structure with the magnetic Cu atoms residing in the center of the Cu-O octahedrons (Figure 5.1 a). We focus on one layer of Cu atoms to establish the spin Hamiltonian. Two exchange couplings, the NN and second-NN exchange parameters J and J_2, are used to fit the spin-wave dispersion from the inelastic neutron scattering data (Figure 5.1 b) [1]. The spin Hamiltonian takes the form

$$H_{\mathrm{La_2CuO_4}} = J \sum_{<i,j>} \vec{S}_i \cdot \vec{S}_j + J_2 \sum_i \vec{S}_i \cdot \vec{S}_{i'} \tag{5.1}$$

The sum $<i, j>$ is over the neighboring spin up and spin down sites i and j. i' marks the second-NN spin relative to site i which has the same spin direction as spin i. From fitting the inelastic neutron scattering data, J and J_2 are determined to be 104.1 meV and - 18 meV at 10 K [1].

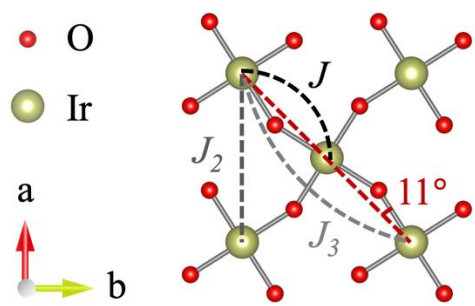

Figure 5.2 The Ir-O plane viewed from the *c*-axis. *J*, J_2, and J_3 are the NN, second-NN, and third-NN exchange couplings, respectively. The angle between the Ir-Ir bond and the Ir-O bond is around 11°.

Sr_2IrO_4 has a similar perovskite structure as La_2CuO_4, except that the Ir-O octahedra are rotated by ~11° (Figure 5.2) [2,3] with canted magnetic moments locked with the rotation of the octahedra [3-15]. The magnetic structure can be described with a Heisenberg model with the NN, second-NN, and third-NN exchange couplings J, J_2, and J_3 (Figure 5.2).

$$H_{\mathrm{Sr_2IrO_4}} = J \sum_{<i,j>} \vec{S}_i \cdot \vec{S}_j + J_2 \sum_i \vec{S}_i \cdot \vec{S}_{i'} + J_3 \sum_i \vec{S}_i \cdot \vec{S}_{i'} \tag{5.2}$$

The exchange parameters are experimentally determined as J = 60 meV, J_2 = - 20 meV, and J_3 = 15 meV [4].

5.1.2 Magnetism of $Sr_3Ir_2O_7$: Spin Wave or Quantum Dimer?

The magnetism of the bilayer iridate $Sr_3Ir_2O_7$ is not as straightforward as Sr_2IrO_4, because an unusually large magnetic gap ~99 meV has been observed in RIXS data [16]. Two models have been proposed to explain its magnetic excitations, the spin-wave model [16,17] and the quantum dimer model [18,19] (Figure 2.9).

As we have introduced in Chapter 2, magnetic bands have been observed with RIXS. In the earlier work, only one energy band has been identified, which has been attributed to two almost-degenerate acoustic and optical magnon branches [16]. The detailed spin Hamiltonian is given in Equation 5.3 which includes the intralayer and interlayer couplings H_{intra} and H_{inter} [16]

$$\begin{gathered} H = H_{intra} + H_{inter} \\ H_{intra} = \sum_{<i,j>} [J\vec{S}_i \cdot \vec{S}_j + \Gamma S_i^z S_j^z + D\left(S_i^x S_j^y - S_i^y S_j^x\right)] + J_2 \sum_i \vec{S}_i \cdot \vec{S}_{i'} + J_3 \sum_i \vec{S}_i \cdot \vec{S}_{i'} \\ H_{inter} = \sum_i [J_C \vec{S}_i \cdot \vec{S}_{i+z} + \Gamma_C S_i^z S_{i+z}^z + D_C\left(S_i^x S_{i+z}^y - S_i^y S_{i+z}^x\right)] + J_{2C} \sum_i \vec{S}_i \cdot \vec{S}_{i'+z} \end{gathered} \tag{5.3}$$

The parameters J, J_2, J_3, J_C, and J_{2C} are the isotropic exchange interactions where the subscript 1, 2, and 3 again denote the NN, second-NN, and third-NN, respectively, and the subscript C denotes interlayer couplings. Figure 5.3 displays a pictorial illustration of the various isotropic exchange

interactions by connecting the spins at different sites with blue solid lines. The parameters Γ is the anisotropic exchange term resulting from the PD interactions from Hund's exchange and Γ_C represents the exchange interaction due to the staggered rotations of the Ir-O octahedra [20]. D and D_C are the DM interactions arising from the rotations of the octahedra.

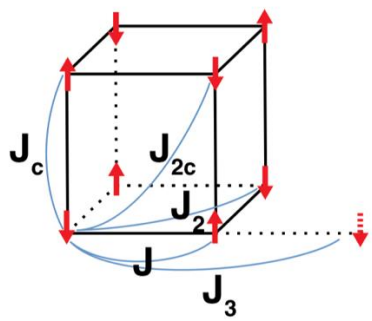

Figure 5.3 Various exchange interactions are represented with blue solid lines connecting different spin sites (red arrows), adapted from Reference [16] with permission.

J, J_C, Γ, Γ_C, D, and D_C can be expressed in terms of two microscopic parameters $\eta = J_H/U$, the ratio of the Hund's coupling to the Coulomb interaction, and θ which parametrizes the tetragonal distortion [20]. Thus there are only five free parameters in the spin Hamiltonian, η, θ, J_2, J_3, and J_{2C}. The fitting parameters are given in Table 5.1 and the fitting curves (red solid lines) of the magnon dispersion and mode intensity (black dots) are plotted in Figure 5.4 [16]. Two fitting curves are present in Figure 5.4 a, corresponding to the overlapping acoustic and optical magnon branches. Notably, large η and θ, which yields large anisotropic exchange interactions, are key in reproducing the large magnon gap.

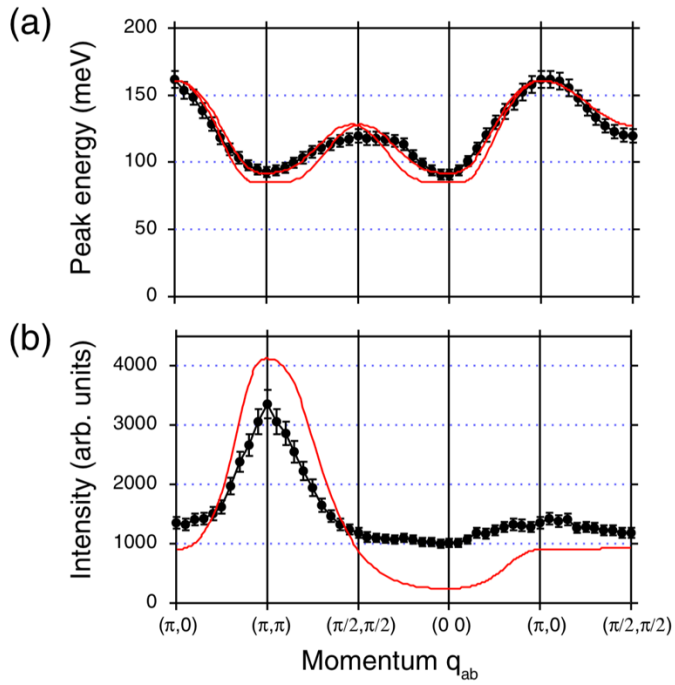

Figure 5.4 Fittings (red solid line) to the experimental (black dots) (a) magnon energy dispersion, and (b) mode intensity using the spin Hamiltonian in Equation 5.3. This figure is adapted from Reference [16] with permission.

Table 5.1 The fitting parameters of the spin-wave model of $Sr_3Ir_2O_7$ in meV [16]

J	J_2	J_3	J_C	J_{2C}	Γ	Γ_C	D	D_C
93	11.9	14.6	25.2	6.2	4.4	34.3	24.5	28.1

In a following RIXS study, a second magnon branch with a lower intensity has been identified using higher-resolution RIXS instruments [18]. The presence of the second magnon band is hard to reconcile with the spin-wave model, because it is asymmetric with respect to the wave vector point (1/4 π, 1/4 π) (feature D of Figure 5.5). Therefore, a bond operator mean-field theory has been developed which attributes the new magnon band to quantum dimer excitations [18].

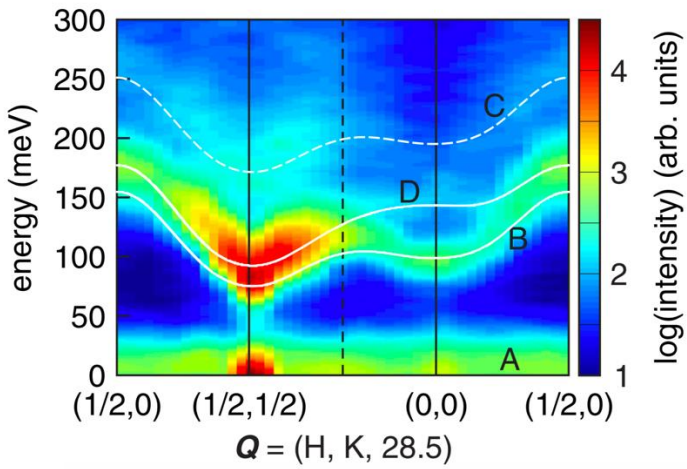

Figure 5.5 High-resolution RIXS data featuring multiple magnetic energy bands in $Sr_3Ir_2O_7$. A is due to the elastic scattering with almost-zero energy. B is the lower energy magnetic branch that has been identified in Reference [16]. C is the newly discovered magnetic branch at a higher energy. D is higher-order magnetic scattering. This figure is adapted from Reference [18] with permission.

In the bilayer Heisenberg model, a quantum phase transition (QPT) emerges as the interlayer coupling increases relative to the intralayer coupling, concurrent with an excitation gap [21-27]. In the limit of large or small ratio of J/J_C, this model can be solved accurately with either the spin-wave theory or perturbation theory. However, in the intermediate region, only approximate results can be acquired using the bond-operator mean-field theory. The obtained fitting parameters are given in Table 5.2.

Table 5.2 The fitting parameters of the quantum dimer model of $Sr_3Ir_2O_7$ in meV [18]

J	J_2	J_3	J_C	Γ	D
7.2	-15	6	90	18.8	25

In the sections to follow, I will introduce our theoretical treatment of two-magnon scatterings to explain the polarized Raman data, which is based on spin-wave theory and provide a third interpretation to the inelastic scattering results.

5.2 Two-Magnon Scattering of a Bilayer Square-Lattice AFM: NN Heisenberg Model

5.2.1 Magnon Dispersions and DOS

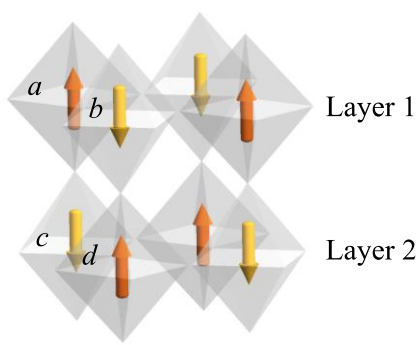

Figure 5.6 Four different sites *a*, *b*, *c*, and *d* within one unit cell of $Sr_3Ir_2O_7$. *a* and *d* sites are spin up. *b* and *d* sites are spin down.

Consider the spin Hamiltonian of a bilayer AFM system ($J > 0$)

$$H = J\sum_{<i,j>,n}\vec{S}_{i,n}\cdot\vec{S}_{j,n} + J_C\sum_i\vec{S}_{i,1}\cdot\vec{S}_{i,2} \tag{5.4}$$

As shown in Figure 5.6, there are four different spin sites in $Sr_3Ir_2O_7$ marked as *a*, *b*, c and *d*. Applying the Holstein-Primakoff transformation (up to the leading order) followed by the Fourier transform

$$
\begin{aligned}
S_{i,1}^{+} &= S_{i,1}^{x} + iS_{i,1}^{y} = \sqrt{2S/N}\textstyle\sum_{\vec{k}} a_{\vec{k}} e^{-i\vec{k}\cdot\vec{r}_i}, S_{i,1}^{-} = S_{i,1}^{x} - iS_{i,1}^{y} = \sqrt{2S/N}\textstyle\sum_{\vec{k}} a_{\vec{k}}^{+} e^{i\vec{k}\cdot\vec{r}_i} \\
S_{j,1}^{+} &= S_{j,1}^{x} + iS_{j,1}^{y} = \sqrt{2S/N}\textstyle\sum_{\vec{k}} b_{\vec{k}}^{+} e^{i\vec{k}\cdot\vec{r}_j}, S_{j,1}^{-} = S_{j,1}^{x} - iS_{j,1}^{y} = \sqrt{2S/N}\textstyle\sum_{\vec{k}} b_{\vec{k}} e^{-i\vec{k}\cdot\vec{r}_j} \\
S_{i,2}^{+} &= S_{i,2}^{x} + iS_{i,2}^{y} = \sqrt{2S/N}\textstyle\sum_{\vec{k}} c_{\vec{k}}^{+} e^{i\vec{k}\cdot\vec{r}_i}, S_{i,2}^{-} = S_{i,2}^{x} - iS_{i,2}^{y} = \sqrt{2S/N}\textstyle\sum_{\vec{k}} c_{\vec{k}} e^{-i\vec{k}\cdot\vec{r}_i} \\
S_{j,2}^{+} &= S_{j,2}^{x} + iS_{j,2}^{y} = \sqrt{2S/N}\textstyle\sum_{\vec{k}} d_{\vec{k}} e^{-i\vec{k}\cdot\vec{r}_j}, S_{j,2}^{-} = S_{j,2}^{x} - iS_{j,2}^{y} = \sqrt{2S/N}\textstyle\sum_{\vec{k}} d_{\vec{k}}^{+} e^{i\vec{k}\cdot\vec{r}_j}
\end{aligned}
\tag{5.5}
$$

where S^{+} and S^{-} are the spin ladder operators, S^{x} and S^{y} are the *x*- and *y*-components of spins, $S = 1/2$ is the total effective angular momentum of Ir atoms, *N* is the total number of primitive cells, $a_{\vec{k}}$, $b_{\vec{k}}$, $c_{\vec{k}}$, and $d_{\vec{k}}$ are bosonic operators with momentum $\vec{k}$, and $\vec{r}_i$ is the position vector of lattice site *i*. The spin Hamiltonian Equation 5.4 can be rewritten below using bosonic creation and annihilation operators in the momentum space,

$$
\begin{aligned}
H = JSz\textstyle\sum_{\vec{k}}[\gamma_{\vec{k}}(a_{\vec{k}}b_{\vec{k}} + c_{\vec{k}}d_{\vec{k}} + a_{\vec{k}}^{+}b_{\vec{k}}^{+} + c_{\vec{k}}^{+}d_{\vec{k}}^{+}) + (a_{\vec{k}}^{+}a_{\vec{k}} + b_{\vec{k}}^{+}b_{\vec{k}} + c_{\vec{k}}^{+}c_{\vec{k}} + d_{k}^{+}d_{k})] \\
+J_c S\textstyle\sum_{\vec{k}}(a_{\vec{k}}c_{\vec{k}} + b_{\vec{k}}d_{\vec{k}} + a_{\vec{k}}^{+}c_{\vec{k}}^{+} + b_{\vec{k}}^{+}d_{\vec{k}}^{+} + a_{\vec{k}}^{+}a_{\vec{k}} + b_{\vec{k}}^{+}b_{\vec{k}} + c_{\vec{k}}^{+}c_{\vec{k}} + d_{\vec{k}}^{+}d_{\vec{k}})
\end{aligned}
\tag{5.6}
$$

where $z = 4$ is the coordination number and $\gamma_{\vec{k}} = (\cos k_x + \cos k_y)/2$. This Hamiltonian can be diagonalized via the Bogoliubov transformation, which transforms these bosonic operators into magnon creation (α^{+}, β^{+}, γ^{+}, δ^{+}) or annihilation operators (α, β, γ, and δ),

$$
\begin{pmatrix} \alpha \\ \beta \\ \gamma^{+} \\ \delta^{+} \end{pmatrix} = \begin{pmatrix}
\frac{u_1 + v_1}{\sqrt{8u_1v_1}} & \frac{u_1 + v_1}{\sqrt{8u_1v_1}} & \frac{-u_1 + v_1}{\sqrt{8u_1v_1}} & \frac{-u_1 + v_1}{\sqrt{8u_1v_1}} \\
\frac{u_2 + v_2}{\sqrt{8u_2v_2}} & \frac{-u_2 - v_2}{\sqrt{8u_2v_2}} & \frac{u_2 - v_2}{\sqrt{8u_2v_2}} & \frac{-u_2 + v_2}{\sqrt{8u_2v_2}} \\
\frac{-u_1 + v_1}{\sqrt{8u_1v_1}} & \frac{-u_1 + v_1}{\sqrt{8u_1v_1}} & \frac{u_1 + v_1}{\sqrt{8u_1v_1}} & \frac{u_1 + v_1}{\sqrt{8u_1v_1}} \\
\frac{u_2 - v_2}{\sqrt{8u_2v_2}} & \frac{-u_2 + v_2}{\sqrt{8u_2v_2}} & \frac{u_2 + v_2}{\sqrt{8u_2v_2}} & \frac{-u_2 - v_2}{\sqrt{8u_2v_2}}
\end{pmatrix} \begin{pmatrix} a \\ d \\ b^{+} \\ c^{+} \end{pmatrix}
\tag{5.7}
$$

where

$$u_1 = \sqrt{Jz\left(1 - \gamma_{\vec{k}}\right)}$$
$$v_1 = \sqrt{2J_C + Jz(1 + \gamma_{\vec{k}})}$$
$$u_2 = \sqrt{Jz(1 + \gamma_{\vec{k}})}$$
$$v_2 = \sqrt{2J_C + Jz(1 - \gamma_{\vec{k}})}$$

After diagonalization with the 4×4 matrix in Equation 5.7, the eigen energies can be obtained:

$$E_1 = Su_1v_1, \text{and } E_2 = Su_2v_2. \tag{5.8}$$

Each energy band is doubly degenerate with one spin-up and one spin-down magnon branch.

As shown in Figure 5.7, the non-zero optical magnon energy at Γ-point is unique to the bilayer compound and contributes to a jump in the DOS at ~400 cm^{-1}, therefore leading to the observation of two-magnon feature M_1 at ~800 cm^{-1}. Furthermore, E_1 and E_2 are dispersionless along the *X*-*M* line, both contributing to the diverging DOS at ~950 cm^{-1}, which is the origin of the two-magnon feature M_2 at ~1900 cm^{-1}.

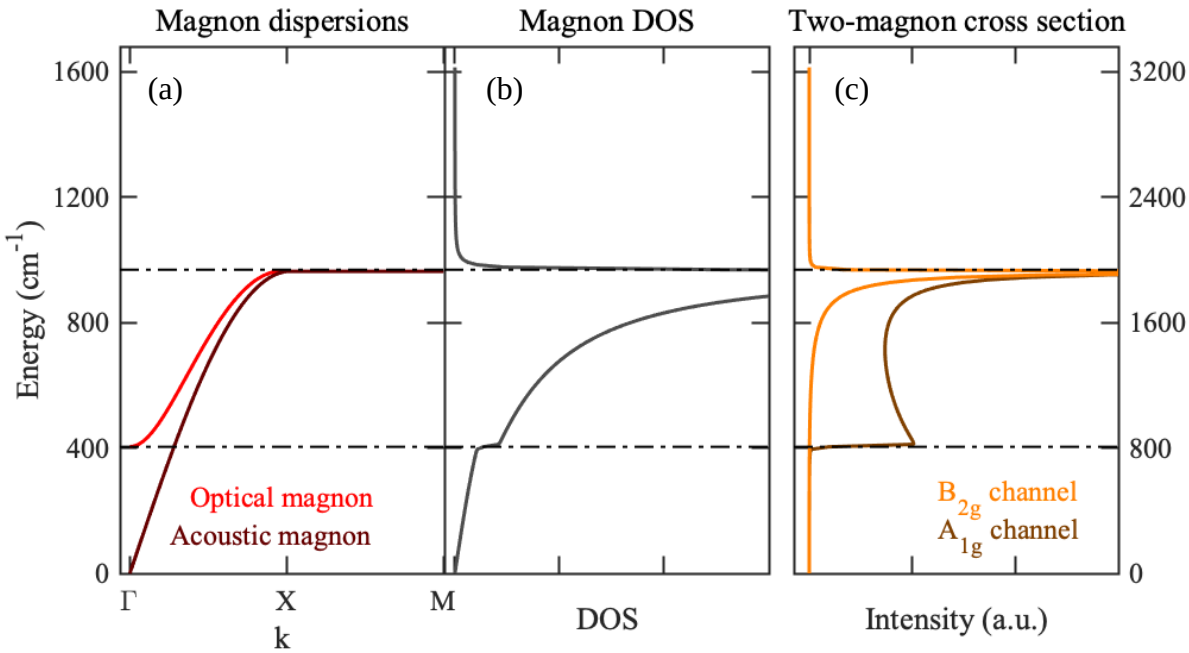

Figure 5.7 (a) The magnon dispersions, (b) the magnon DOS – magnon energy diagram, and (c) two-magnon cross section – two-magnon energy diagram using the NN Heisenberg model. Energies are in unit of cm^{-1} to compare with our Raman data.

Although detailed calculations of the two-magnon scatterings will be discussed in the next section, here we directly use the results to derive the exchange parameters we use in Fig 5.8. The energy of M_1 is twice of the zone-center optical magnon energy, $4\sqrt{JJ_C}$, and the energy of M_2 can be obtained by 0.73 times twice of the zone-boundary magnon energy, $1.46\sqrt{J(4J+2J_C)}$. The factor of 0.73 is a quantum correction to the divergent DOS at zone boundary [28]. The validity of this number has already been confirmed in Sr_2IrO_4, because the ratio of its two-magnon energy of 160 meV [29] to twice its single magnon energy at X-point of 220 meV [4] is ~0.73. Solving for $4\sqrt{JJ_C} = 800$ cm^{-1} and $1.46\sqrt{J(4J+2J_C)} = 1400$ cm^{-1}, we obtain $J = 458$ cm^{-1} (56.8 meV) and $J_C = 87$ cm^{-1} (11 meV). As we introduced in Section 5.1.2, a QPT from an AFM to a quantum dimer phase exists with increasing J_C in bilayer Heisenberg AFM. The quantum critical point

(QCP) of the ratio J/J_C is predicted to be $r_c = 2.522$ [30,31]. The ratio of J/J_C in $Sr_3Ir_2O_7$ is r = 0.19, much smaller than the QCP, which is self-consistent with our choice of the spin-wave theory in the first place.

5.2.2 Two-Magnon Cross Section

In this section, we will present our derivation of the two-magnon cross section plotted in Fig 5.8 (c). The interaction between light and two-magnon excitations can be described by the following scattering Hamiltonian (Loudon-Fleury Hamiltonian), which includes all the symmetry-allowed combinations of NN spin products [32]

$$H^S = \alpha \sum_{<i,j>,n} \phi_{ij} \vec{S}_{i,n} \cdot \vec{S}_{j,n} \tag{5.9}$$

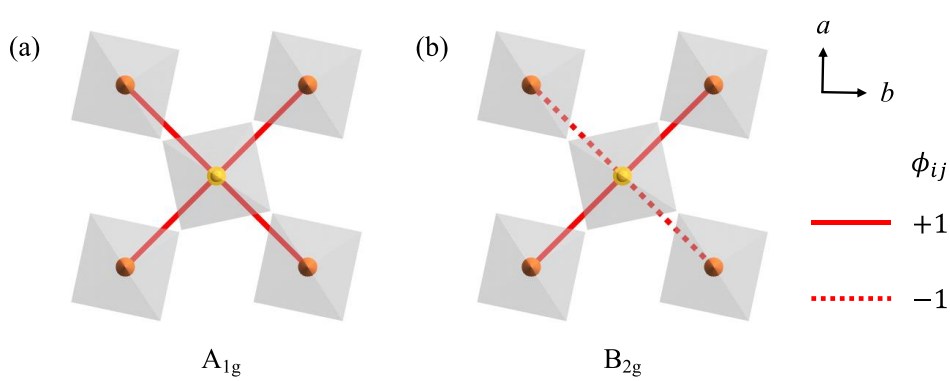

Figure 5.8 Bond-dependent ϕ_{ij} factor of NN bonds in (a) A_{1g} and (b) B_{2g} scattering Hamiltonian. $\phi_{ij} = +1$ for bonds marked by red solid lines, and $\phi_{ij} = -1$ for bonds marked by red dashed lines.

For A_{1g} symmetry, $\phi_{ij} = +1$ for all NN sites (Figure 5.8 a), which preserves all symmetry operations of the D_{4h} point group. Expressed in the form of magnon operators and only considering

the quadratic terms which make dominant contributions to the two-magnon scattering [28], Equation 5.9 can be written as

$$H_{A_{1g}}^{S} = \Gamma_1 \sum_{\vec{k}} \left(\alpha_{\vec{k}} \gamma_{\vec{k}} + \alpha_{\vec{k}}^{+} \gamma_{\vec{k}}^{+} \right) + \Gamma_2 \sum_{\vec{k}} \left(\beta_{\vec{k}} \delta_{\vec{k}} + \beta_{\vec{k}}^{+} \delta_{\vec{k}}^{+} \right) \tag{5.10}$$

where $\Gamma_1 = -J_C S u_1 / v_1$, and $\Gamma_2 = J_C S u_2 / v_2$.

For B_{2g} symmetry, $\phi_{ij} = \pm 1$ depending on the direction of the NN bond (Figure 5.8 b). This B_{2g} scattering Hamiltonian written in magnon operators takes the form

$$H_{B_{2g}}^{S} = \Gamma_3 \sum_{\vec{k}} \left(\alpha_{\vec{k}} \gamma_{\vec{k}} + \alpha_{\vec{k}}^{+} \gamma_{\vec{k}}^{+} \right) + \Gamma_4 \sum_{\vec{k}} \left(\beta_{\vec{k}} \delta_{\vec{k}} + \beta_{\vec{k}}^{+} \delta_{\vec{k}}^{+} \right), \tag{5.11}$$

where $\Gamma_3 = \gamma_- (J_C + Jz)/(u_1 v_1)$, $\Gamma_4 = \gamma_- (J_C + Jz)/(u_2 v_2)$, and $\gamma_- = (\cos k_x - \cos k_y)/2$.

The calculated A_{1g} and B_{2g} two-magnon scattering cross sections are plotted in Panel c of Figure 5.7. In A_{1g} channel, because all lattice symmetries are preserved, the two-magnon cross section captures all DOS features, resulting in two intensity maxima. The lower-energy intensity maximum is originated from the Γ-point optical magnon, and the higher-energy one from zone-boundary magnon. In B_{2g} channel, however, because the *c*-axis four-fold rotational symmetry is broken, the contribution from Γ-point vanishes, and thus only one intensity maximum shows up from the zone-boundary magnon.

It is worth-noting that in single-layer Sr_2IrO_4, only intralayer exchange term contributes to the Heisenberg spin Hamiltonian, which commutes with the A_{1g} scattering Hamiltonian. As a result, this channel does not create any two-magnon excitations, unless other terms (e.g. beyond NNs)

are included in the spin Hamiltonian. In contrast, for a bilayer system that we consider here, $[H, H_{A_{1g}}^{S}] \neq 0$, and thus two-magnon excitations are allowed in the A_{1g} channel.

5.3 Two-Magnon Scattering of a Bilayer Square-Lattice AFM: Beyond-NN Heisenberg Model with SOC

5.3.1 Magnon Dispersions and DOS

In the simple model above, only the intralayer NN and interlayer exchange interaction J and J_C are considered. In this section, we further include intralayer second-NN and third-NN exchange interactions J_2 and J_3 (Figure 5.2) [4], and dipole-like SOC interaction Δ [20] in the spin Hamiltonian. All these terms exist naturally in iridates with significant amplitudes. In Reference [20], only NN SOC interaction has been demonstrated. Here we extend the same type of SOCs to beyond-NN neighbors. Specifically, the SOC term we consider here is the second-NN interaction, which can be explicitly written as

$$H_{SOC} = \Delta \sum_{i,i',n} (\vec{S}_{i,n} \cdot \vec{\sigma}_2)(\vec{S}_{i',n} \cdot \vec{\sigma}_2), \tag{5.12}$$

where $\vec{\sigma}_2 = \vec{r}_{i'} - \vec{r}_i$ is a vector pointing from site i to the its second-NN i'.

Here, we apply the Holstein-Primakoff transformations and the Bogoliubov transformations to the spin Halmitonian, which in this case take the form

$$\begin{pmatrix} \alpha \\ \gamma \\ \delta \\ \beta \\ \alpha^+ \\ \gamma^+ \\ \delta^+ \\ \beta^+ \end{pmatrix} = \frac{1}{4} \begin{pmatrix} iM_{11} & M_{11} & M_{11} & iM_{11} & M_{12} & iM_{12} & iM_{12} & M_{12} \\ iM_{21} & M_{21} & -M_{21} & -iM_{21} & -M_{22} & -iM_{22} & iM_{22} & M_{22} \\ -iM_{31} & M_{31} & -M_{31} & iM_{31} & -M_{32} & iM_{32} & -iM_{32} & M_{32} \\ -iM_{41} & M_{41} & M_{41} & -iM_{41} & M_{42} & -iM_{42} & -iM_{42} & M_{42} \\ M_{12} & -iM_{12} & -iM_{12} & M_{12} & -iM_{11} & M_{11} & M_{11} & -iM_{11} \\ -M_{22} & iM_{22} & -iM_{22} & M_{22} & -iM_{21} & M_{21} & -M_{21} & iM_{21} \\ -M_{32} & -iM_{32} & iM_{32} & M_{32} & iM_{31} & M_{31} & -M_{31} & -iM_{31} \\ M_{42} & iM_{42} & iM_{42} & M_{42} & -iM_{41} & M_{41} & M_{41} & -iM_{41} \end{pmatrix} \begin{pmatrix} a \\ b \\ c \\ d \\ a^+ \\ b^+ \\ c^+ \\ d^+ \end{pmatrix} \tag{5.13}$$

where

$$M_{11,21,31,41} = -\frac{f_{1,2,3,4} + g_{1,2,3,4}}{\sqrt{f_{1,2,3,4} g_{1,2,3,4}}}$$

$$M_{12,22,32,42} = \frac{-f_{1,2,3,4} + g_{1,2,3,4}}{\sqrt{f_{1,2,3,4} g_{1,2,3,4}}}$$

and

$$f_1 = \sqrt{J(1+\gamma_{\vec{k}}) - J_2(1-\gamma_{\vec{k}'}) - J_3(1-\gamma_{2\vec{k}}) - \Delta\gamma_{\vec{k}''} + J_C/2}$$

$$g_1 = \sqrt{J(1-\gamma_{\vec{k}}) - J_2(1-\gamma_{\vec{k}'}) - J_3(1-\gamma_{2\vec{k}}) + \Delta\gamma_{\vec{k}''}}$$

$$f_2 = \sqrt{J(1-\gamma_{\vec{k}}) - J_2(1-\gamma_{\vec{k}'}) - J_3(1-\gamma_{2\vec{k}}) + \Delta\gamma_{\vec{k}''} + J_C/2}$$

$$g_2 = \sqrt{J(1+\gamma_{\vec{k}}) - J_2(1-\gamma_{\vec{k}'}) - J_3(1-\gamma_{2\vec{k}}) - \Delta\gamma_{\vec{k}''}}$$

$$f_3 = \sqrt{J(1-\gamma_{\vec{k}}) - J_2(1-\gamma_{\vec{k}'}) - J_3(1-\gamma_{2\vec{k}}) - \Delta\gamma_{\vec{k}''} + J_C/2}$$

$$g_3 = \sqrt{J(1+\gamma_{\vec{k}}) - J_2(1-\gamma_{\vec{k}'}) - J_3(1-\gamma_{2\vec{k}}) + \Delta\gamma_{\vec{k}''}}$$

$$f_4 = \sqrt{J(1+\gamma_{\vec{k}}) - J_2(1-\gamma_{\vec{k}'}) - J_3(1-\gamma_{2\vec{k}}) + \Delta\gamma_{\vec{k}''} + J_C/2}$$

$$g_4 = \sqrt{J(1-\gamma_{\vec{k}}) - J_2(1-\gamma_{\vec{k}'}) - J_3(1-\gamma_{2\vec{k}}) - \Delta\gamma_{\vec{k}''}}$$

and

$$\gamma_{\vec{k}'} = \cos k_x \cos k_y$$
$$\gamma_{2\vec{k}} = (\cos 2k_x + \cos 2k_y)/2$$
$$\gamma_{\vec{k}''} = -\sin k_x \sin k_y$$

The eigen energies are

$$\begin{aligned} E_1' &= 4Sf_1g_1 \\ E_2' &= 4Sf_2g_2 \\ E_3' &= 4Sf_3g_3 \\ E_4' &= 4Sf_4g_4 \end{aligned} \tag{5.14}$$

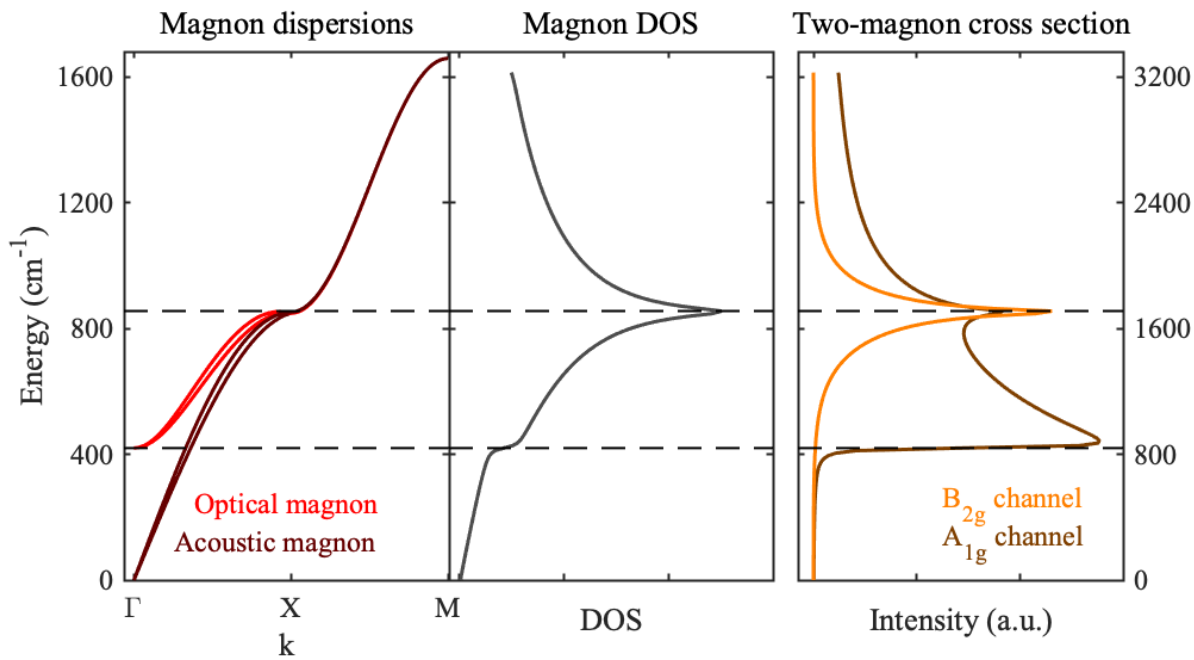

Figure 5.9 (a) The magnon dispersions, (b) the magnon DOS – energy diagram, and (c) two-magnon cross section – energy diagram using the J-J_2-J_3-J_C model with SOC.

The intralayer exchange energies used in the calculations are consistent with the RIXS study of Sr_2IrO_4 [4], which are $J = 60$ meV ($484\ \mathrm{cm}^{-1}$), $J_2 = -20$ meV ($-161\ \mathrm{cm}^{-1}$), and $J_3 = 15$ meV ($121\ \mathrm{cm}^{-1}$). Interlayer exchange energy J_C is determined as 91 cm^{-1}, which minimizes the overall energy deviations of both M_1 and M_2. Again J_C is found to be a small value compared

to J (~0.19 of J), which justifies our choice of the spin-wave model. The strength of the SOC term Δ is chosen as a small value (16 cm^{-1}). It is worthwhile to emphasize that as long as Δ is small, its value only changes the overall amplitude of the B_{2g} two-magnon intensity, while other qualitative features reported below are insensitive to the value of Δ. We observe a gap of ~400 cm^{-1} at Γ-point (Figure 5.9 a), similar to the previous model, and large dispersions along the *X*-*M* line, which is a mimic of Sr_2IrO_4. The SOC term slightly breaks the two-fold degeneracy of each magnon band. In this case, *X*-point is a van Hove singularity point with a divergent DOS (Figure 5.9 b). In the current model, only the single Van Hove singularity point contributes to the large DOS peak at ~800 cm^{-1}, in contrast to the model above with only NN exchange interaction, where the entire *X*-*M* line is responsible for its divergent DOS.

5.3.2 Two-Magnon Cross Section

Through calculating the scattering Hamiltonian of Equation 5.9, the two-magnon cross section maintains the main shape as in the simplified model in the A_{1g} channel, with two intensity maxima at ~800 cm^{-1} and ~1700 cm^{-1}. However, the van Hove singularity point is invisible to the B_{2g} scattering Hamiltonian with only NN exchange interaction. Because J_2 is not negligible (1/3 J), another B_{2g} scattering Hamiltonian can be constructed including second-NN exchange interaction, which has a checkerboard pattern as shown in Figure 5.10.

$$H_{B_{2g}}^{S'} = \alpha' \sum_{i,i',n} \phi_{ii'n} (\vec{S}_{i,n} \cdot \vec{S}_{i',n}) \tag{5.15}$$

$\phi_{ii'n} = +1$ for bonds marked in red solid line, and $\phi_{ii'n} = -1$ for bonds marked in red dashed line. This scattering Hamiltonian flips sign under the vertical mirror operation (black dashed line).

This light-spin interaction term is sensitive to contributions from the van Hove singularity point. Thus the corresponding cross section kinks up at ~1700 cm^{-1} as shown in Panel c of Figure 5.9.

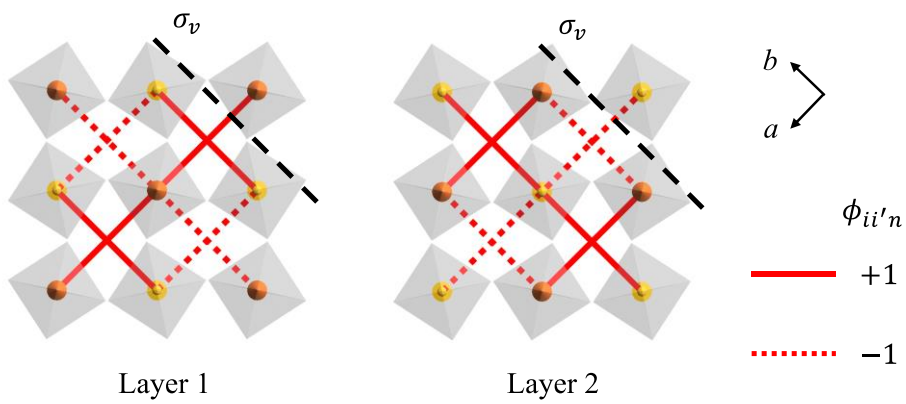

Figure 5.10 Checkerboard pattern of bond-dependent $\boldsymbol{\phi_{ii'n}}$ factor of second-NN bonds in the new $\boldsymbol{B_{2g}}$ scattering Hamiltonian. $\boldsymbol{\phi_{ii'n} = +1}$ for bonds marked by red solid lines, and $\boldsymbol{\phi_{ii'n} = -1}$ for bonds marked by red dashed lines.

5.4 Comparison of Two Models

Through comparison of the two models discussed above, our first observation is that the physics of the first two-magnon mode M_1 is quite robust regardless of the model we choose. Firstly, the A_{1g} symmetry ensures that the Γ-point magnon gap shows up in the two-magnon scattering cross section. Secondly, the gap energy is not sensitive to the number of neighbors included in the second model. Because Γ-point magnon represents a collective motion where equivalent spins have the same motion, adding neighbors from two equivalent sites (*i.e.*, J_2 and J_3) does not affect its energy.

We now proceed to the zone boundary where the second two-magnon mode M_2 is originated. In the first model, the entire zone boundary is dispersionless, resulting in a divergent DOS, which is the origin of M_2. As second- and third-NN spin exchanges are included in the second model, the *X*-point becomes a van Hove singularity point with a divergent DOS. Similar to the first model, this divergent DOS also results in two-magnon features. However, as mentioned in the previous section, this two-magnon feature arises from two-magnon excitations beyond NN. The mathematical reason is that every NN term in B_{2g} scattering Hamiltonian contains cosine pre-factors of k_x or k_y. At the *X*-point, because $k_x = k_y = \pi/2$ and $\cos k_x = \cos k_y = 0$, its contribution to two-magnon scattering vanishes. Because beyond-NN exchange interaction is not negligible in our spin Hamiltonian, it is natural to include second-NN in B_{2g} scattering Hamiltonian. These terms contain cosine terms of $k_x + k_y$ and $k_x - k_y$, which are non-zero at the *X*-point. Thus, the divergent DOS associated with the *X*-point becomes visible in two-magnon scattering and results in M_2. Similarly, SOC becomes a necessary ingredient in generating M_2 in the second model.

In summary, although M_2 appears in both models with similar energies, they actually have different origins. The first simple model is sufficient in the situation where beyond-NN exchanges are negligible, for example in cuprates [1]. In comparison, the second model offers a realistic and interesting manifestation of both the large magnon dispersions along the *X*-*M* line as established in the single layer Sr_2IrO_4, and the strong SOC in perovskite iridates.

5.5 Comparison of A_{1g} Two-Magnon and Amplitude Mode of a Bilayer AFM

Having established zone-center two-magnon scattering as the origin of M_1, we discuss the relation between M_1 and the amplitude mode which appears near the QCP. Both modes share some similarities leading to difficulty in distinguishing the two modes from the data only. Firstly, zone-center two-magnon excitation and the amplitude mode (*i.e.*, Higgs mode) are both of A_{1g} symmetry and can both be characterized by the Loudon-Fleury scattering Hamiltonian [31]. Secondly, the amplitude mode is in general damped by other low-energy excitations, resulting in a broad line shape similar to that of the two-magnon excitation. However, the amplitude mode and the zone-center two-magnon excitation do happen at different r. In our calculations, the zone-center two-magnon excitations is visible only when J_C is weak compared with J (*i.e.*, well below r_c). In a recent numeric study [31], the amplitude mode is only well-defined in a very small window near the QCP. Neither amplitude mode nor zone-center two-magnon mode appears for intermediate r between the two regimes. Based on our fitted value $r = 0.19$, it is more reasonable to attribute M_1 to zone-center two-magnon excitations.

References

[1] R. Coldea, S. Hayden, G. Aeppli, T. Perring, C. Frost, T. Mason, S.-W. Cheong, and Z. Fisk, *Spin waves and electronic interactions in La_2CuO_4*, Physical review letters **86**, 5377 (2001).

[2] Q. Huang, J. Soubeyroux, O. Chmaissem, I. N. Sora, A. Santoro, R. Cava, J. Krajewski, and W. Peck Jr, *Neutron powder diffraction study of the crystal structures of Sr_2RuO_4 and Sr_2IrO_4 at room temperature and at 10 K*, Journal of Solid State Chemistry **112**, 355 (1994).

[3] S. Boseggia *et al.*, *Locking of iridium magnetic moments to the correlated rotation of oxygen octahedra in Sr_2IrO_4 revealed by x-ray resonant scattering*, Journal of Physics: Condensed Matter **25**, 422202 (2013).

[4] J. Kim *et al.*, *Magnetic excitation spectra of Sr_2IrO_4 probed by resonant inelastic X-ray scattering: establishing links to cuprate superconductors*, Physical Review Letters **108**, 177003 (2012).

[5] J. Kim, Y. Choi, J. Kim, J. Mitchell, G. Jackeli, M. Daghofer, J. Van Den Brink, G. Khaliullin, and B. Kim, *Dimensionality driven spin-flop transition in layered iridates*, Physical review letters **109**, 037204 (2012).

[6] Y. Hong, Y. Jo, H. Y. Choi, N. Lee, Y. J. Choi, and W. Kang, *Large magnetic anisotropy in canted antiferromagnetic Sr_2IrO_4 single crystals*, Physical Review B **93**, 094406 (2016).

[7] B. Kim, H. Ohsumi, T. Komesu, S. Sakai, T. Morita, H. Takagi, and T.-h. Arima, *Phase-sensitive observation of a spin-orbital Mott state in Sr_2IrO_4*, Science **323**, 1329 (2009).

[8] I. Fina *et al.*, *Anisotropic magnetoresistance in an antiferromagnetic semiconductor*, Nature communications **5**, 1 (2014).

[9] C. Wang, H. Seinige, G. Cao, J.-S. Zhou, J. B. Goodenough, and M. Tsoi, *Anisotropic magnetoresistance in antiferromagnetic Sr_2IrO_4*, Physical Review X **4**, 041034 (2014).

[10] C. Lu, B. Gao, H. Wang, W. Wang, S. Yuan, S. Dong, and J. M. Liu, *Revealing controllable anisotropic magnetoresistance in spin–orbit coupled antiferromagnet Sr_2IrO_4*, Advanced Functional Materials **28**, 1706589 (2018).

[11] H. Wang, W. Wang, N. Hu, T. Duan, S. Yuan, S. Dong, C. Lu, and J.-M. Liu, *Persistent large anisotropic magnetoresistance and insulator-to-metal transition in spin-orbit-coupled $Sr_2(Ir_{1-x}Ga_x)O_4$ for antiferromagnetic spintronics*, Physical Review Applied **10**, 014025 (2018).

[12] H. Wang, C. Lu, J. Chen, Y. Liu, S. Yuan, S.-W. Cheong, S. Dong, and J.-M. Liu, *Giant anisotropic magnetoresistance and nonvolatile memory in canted antiferromagnet Sr_2IrO_4*, Nature communications **10**, 1 (2019).

[13] L. Miao, H. Xu, and Z. Mao, *Epitaxial strain effect on the J_{eff} = 1/2 moment orientation in Sr_2IrO_4 thin films*, Physical Review B **89**, 035109 (2014).

[14] N. Lee, E. Ko, H. Y. Choi, Y. J. Hong, M. Nauman, W. Kang, H. J. Choi, Y. J. Choi, and Y. Jo, *Antiferromagnet-Based Spintronic Functionality by Controlling Isospin Domains in a Layered Perovskite Iridate*, Advanced Materials **30**, 1805564 (2018).

[15] M. Ge, T. Qi, O. Korneta, D. De Long, P. Schlottmann, W. Crummett, and G. Cao, *Lattice-driven magnetoresistivity and metal-insulator transition in single-layered iridates*, Physical Review B **84**, 100402 (2011).

[16] J. Kim *et al.*, *Large spin-wave energy gap in the bilayer iridate $Sr_3Ir_2O_7$: Evidence for enhanced dipolar interactions near the mott metal-insulator transition*, Physical review letters **109**, 157402 (2012).

[17] X. Lu, D. McNally, M. M. Sala, J. Terzic, M. Upton, D. Casa, G. Ingold, G. Cao, and T. Schmitt, *Doping Evolution of Magnetic Order and Magnetic Excitations in $(Sr_{1-x}La_x)_3Ir_2O_7$*, Physical review letters **118**, 027202 (2017).

[18] M. M. Sala *et al.*, *Evidence of quantum dimer excitations in $Sr_3Ir_2O_7$*, Physical Review B **92**, 024405 (2015).

[19] T. Hogan, R. Dally, M. Upton, J. Clancy, K. Finkelstein, Y.-J. Kim, M. Graf, and S. D. Wilson, *Disordered dimer state in electron-doped $Sr_3Ir_2O_7$*, Physical Review B **94**, 100401 (2016).

[20] G. Jackeli and G. Khaliullin, *Mott insulators in the strong spin-orbit coupling limit: from Heisenberg to a quantum compass and Kitaev models*, Physical review letters **102**, 017205 (2009).

[21] K. Hida, *Quantum Disordered State without Frustration in the Double Layer Heisenberg Antiferromagnet—Dimer Expansion and Projector Monte Carlo Study—*, Journal of the Physical Society of Japan **61**, 1013 (1992).

[22] A. Millis and H. Monien, *Spin Gaps and Spin Dynamics in* $La_{2-x}Sr_xCuO_4$ *and* $YBa_2Cu_3O_{7-\delta}$, Physical review letters **70**, 2810 (1993).

[23] A. Millis and H. Monien, *Spin gaps and bilayer coupling in* $YBa_2Cu_3O_{7-\delta}$ *and* $YBa_2Cu_4O_8$, Physical Review B **50**, 16606 (1994).

[24] A. Sandvik and D. Scalapino, *Order-disorder transition in a two-layer quantum antiferromagnet*, Physical review letters **72**, 2777 (1994).

[25] T. Miyazaki, I. Nakamura, and D. Yoshioka, *Bilayer Heisenberg model studied by the Schwinger-boson Gutzwiller-projection method*, Physical Review B **53**, 12206 (1996).

[26] T. Sommer, M. Vojta, and K. W. Becker, *Magnetic properties and spin waves of bilayer magnets in a uniform field*, The European Physical Journal B-Condensed Matter and Complex Systems **23**, 329 (2001).

[27] C. Hamer, J. Oitmaa, and Z. Weihong, *Restoration of symmetry in the spectrum of the bilayer Heisenberg antiferromagnet*, Physical Review B **85**, 014432 (2012).

[28] C. Canali and S. Girvin, *Theory of Raman scattering in layered cuprate materials*, Physical Review B **45**, 7127 (1992).

[29] H. Gretarsson, N. Sung, M. Höppner, B. Kim, B. Keimer, and M. Le Tacon, *Two-magnon Raman scattering and pseudospin-lattice interactions in* Sr_2IrO_4 *and* $Sr_3Ir_2O_7$, Physical review letters **116**, 136401 (2016).

[30] L. Wang, K. Beach, and A. W. Sandvik, *High-precision finite-size scaling analysis of the quantum-critical point of S = 1/2 Heisenberg antiferromagnetic bilayers*, Physical Review B **73**, 014431 (2006).

[31] M. Lohöfer, T. Coletta, D. Joshi, F. Assaad, M. Vojta, S. Wessel, and F. Mila, *Dynamical structure factors and excitation modes of the bilayer Heisenberg model*, Physical Review B **92**, 245137 (2015).

[32] P. Fleury and R. Loudon, *Scattering of light by one-and two-magnon excitations*, Physical Review **166**, 514 (1968).

Chapter 6 Magnetic Field-Induced Phase Transitions of the CrX_3 Family (X = Cl, Br, I)

In this chapter, I will introduce our work on the second family of quantum magnets CrX_3 (X = Cl, Br, I). Our work on CrX_3 contains two parts, a temperature- and magnetic field-dependent polarized Raman study on the phonon and magnon excitations of bulk CrI_3 which reveals the coexistence of surface-AFM (SAFM) and bulk-FM (BFM), as well as a field-induced structural and magnetic phase transition in bulk CrI_3 (Sections 6.1 – 6.4), and an electron tunneling study on the halogen-dependent spin-wave parameters in bilayer CrX_3 (Section 6.5).

Prior to or concurrent with our Raman study on bulk CrI_3, intensive research has been performed on CrI_3 with Raman spectroscopy, ranging from experimental [1-8] to first-principle studies [9,10], or a combination of the two [11]. The structural phases in bulk [11] and thin CrI_3 [1] have been mapped through the phonon symmetries. Two intriguing modes at 78 cm^{-1} and 128 cm^{-1} have been widely studied in few-layer CrI_3 due to their unique selection rules, which have been proposed first as magnons [2], and then as optical phonons modified by magnetic order in several field-dependent studies [3-5], followed by a first-principle study [10]. Magneto-Raman [6] and magneto-optical effects [7] have been studied on few-layer CrI_3 with external magnetic field applied.

Albeit being a bulk CrI_3 study, our field-dependent polarized Raman data revealed a coexistence of the thin-film (interlayer AFM) and bulk (interlayer FM) features. We also examined the nature

of the 78 cm^{-1} and 128 cm^{-1} magnetic modes, and uncovered the concurrent field-induced magnetic and structural phase transitions. In the next section, I will start by introducing our innovative Raman selection rule measurements with circularly polarized light.

6.1 Raman Selection Rules with Linearly and Circularly Polarized Light

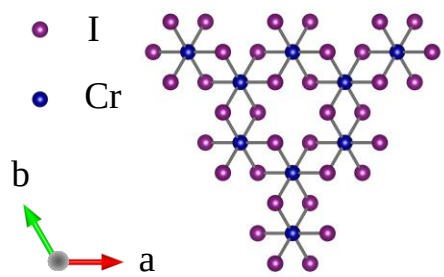

Figure 6.1 Top view of the atomic structure of one layer of CrI_3.

Figure 6.1 shows the atomic structure of CrI_3. As mentioned in Chapter 2, at low temperature, the crystal point group of bulk CrI_3 is the rhombohedral C_{3i}. Referring again to the Raman tensor table [12,13], the Raman-allowed irreducible representations of the C_{3i} point group are A_g and the doubly-degenerate E_g, with their corresponding Raman tensors listed in Table 6.1.

Table 6.1 Raman tensors of the point group C_{3i}

$$\overset{A_g}{\begin{pmatrix} a_1 & \cdot & \cdot \\ \cdot & a_1 & \cdot \\ \cdot & \cdot & a_2 \end{pmatrix}} \quad \overset{E_g}{\begin{pmatrix} b_1 & b_2 & c_1 \\ b_2 & -b_1 & c_2 \\ c_1 & c_2 & \cdot \end{pmatrix}} \quad \overset{E_g}{\begin{pmatrix} b_2 & -b_1 & -c_2 \\ -b_1 & -b_2 & c_1 \\ -c_2 & c_1 & \cdot \end{pmatrix}}$$

Instead of scanning the entire range of the incident and outgoing polarization angles, we utilize the four polarization channels, parallel 0°, parallel 45°, cross 0°, and cross 45°. Normal incidence and back-scattering geometry are used so that only the *x*- and *y*-components of the Raman tensors are active. We follow similar calculation processes as shown in Section 4.3. When the two polarizations are parallel

$$\begin{gathered} I_{A_g} \propto a_1^2 \\ I_{E_g^1} \propto (b_1 \cos 2\theta + b_2 \sin 2\theta)^2 \\ I_{E_g^2} \propto (b_2 \cos 2\theta - b_1 \sin 2\theta)^2 \end{gathered} \tag{6.1}$$

When the two polarizations are perpendicular

$$\begin{gathered} I_{A_g} \propto 0 \\ I_{E_g^1} \propto (b_1 \sin 2\theta - b_2 \cos 2\theta)^2 \\ I_{E_g^2} \propto (b_1 \cos 2\theta + b_2 \sin 2\theta)^2 \end{gathered} \tag{6.2}$$

Table 6.2 Selection rules of point group C_{3i} with linearly polarized light

	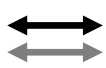 Parallel 0°	 Parallel 45°	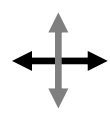 Cross 0°	 Cross 45°
A_g	a_1^2	a_1^2	0	0
E_g^1	b_1^2	b_2^2	b_2^2	b_1^2
E_g^2	b_2^2	b_1^2	b_1^2	b_2^2

The resulting selection rules are listed in Table 6.2. The A_g mode shows up in the parallel channels but not in the cross channels. The E_g mode, on the other hand, shows up in all four polarization channels. Raman spectra of bulk CrI_3 in the four linear polarization channels at 10 K are shown in

Figure 6.2 [2]. The A_g phonons (A_1 – A_3) show up only in parallel channels (black line) while the E_g phonons (E_1 – E_4) are present in both parallel and cross channels, consistent with the selection rule analysis shown in Table 6.2. M_1 and M_2 are magnetic excitations which will be discussed in Section 6.2.

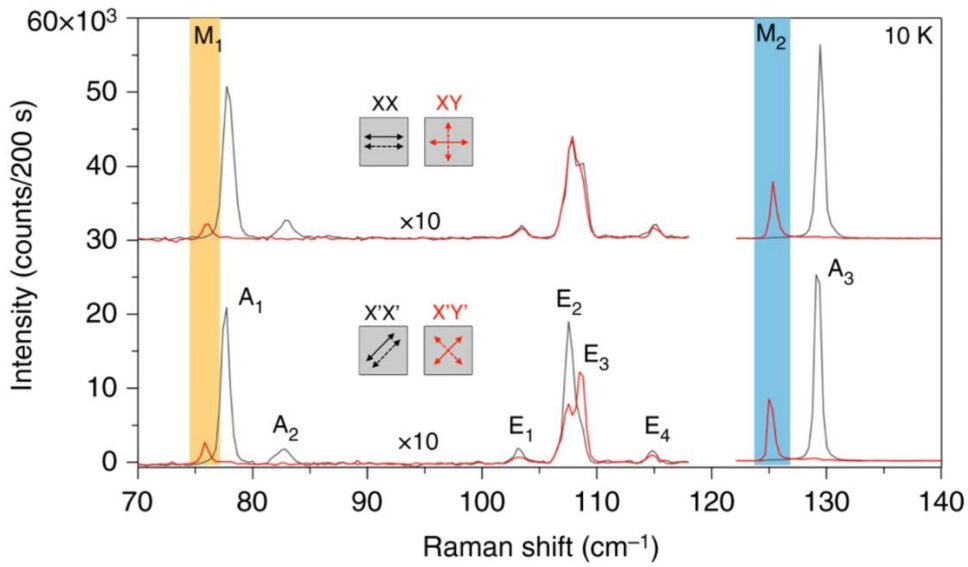

Figure 6.2 Raman spectra of bulk CrI_3 in linear polarization channels at 10 K, adapted from Reference [2]. The A_g phonons (A_1 – A_3) show up only in parallel channels (black line) while the E_g phonons (E_1 – E_4) show up in both parallel and cross channels. M_1 and M_2 are magnetic excitations which show up only in cross channels.

In the magnetic field-dependent study of bulk CrI_3, circularly polarized light has been adopted instead of linearly polarized light, because the magneto-optical Faraday effect of the quartz-based optical components rotates the transmitting linearly polarized light under external magnetic field. This effect introduces artifacts in selection rule measurements, which are observable in the phonon modes shown in Fig 6.3. For simplicity, we analyze this artifact using A_g phonons, and instead of all four linear polarization channels relative to the crystal axes, here we measure with two

geometries, the vertical-vertical (VV) polarization (parallel) and the horizontal-vertical (HV) polarization (cross) channels with respect to the lab frame. The A_g phonons (shaded in red) should show up only in the VV parallel channel according to Table 6.2 (Figure 6.3 a), as is the case at 0 T. However, their intensities leak into the HV cross channel with increasing external field (Figure 6.3 b). As there is no structural phase transition at low magnetic field and the phonon selection rule only depends on the symmetry of the crystal, this intensity leak is purely due to magneto-optical Faraday effect of the optical components.

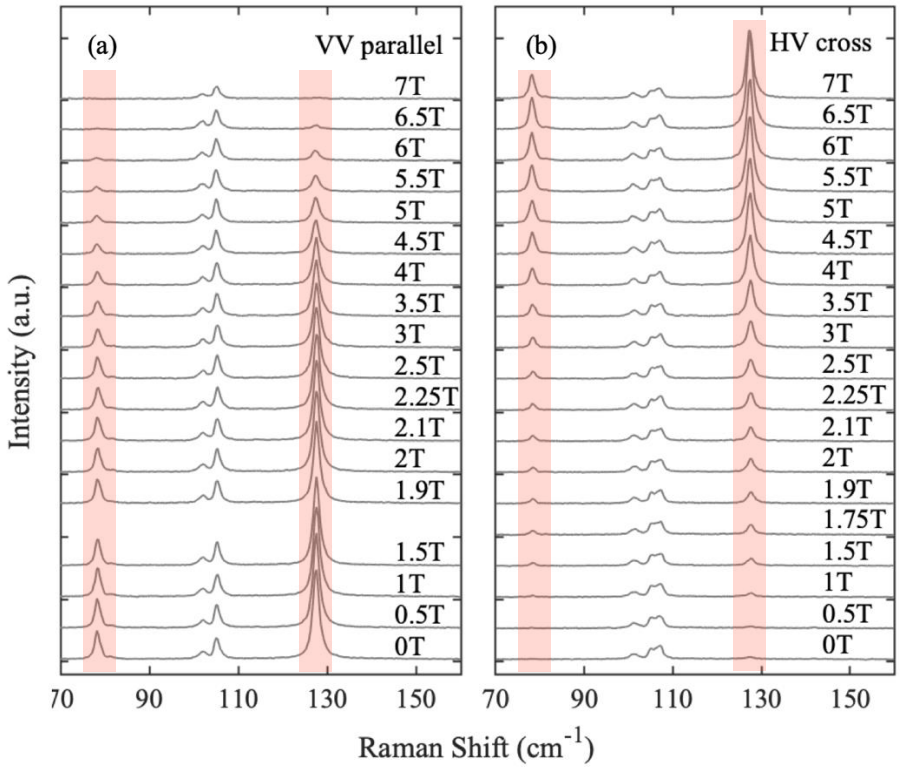

Figure 6.3 Magnetic field-dependent Raman data of bulk CrI_3 at room temperature with (a) VV parallel, and (b) HV cross polarization geometries. The A_g phonons are shaded in red for clarity. The varying intensities of A_g phonons in both parallel and cross channels are artifacts due to the field-induced Faraday effect.

We have quantitatively studied the field dependence of this Faraday rotation angle. Because we are using the lab frame instead of the crystal frame, it is necessary to check that the A_g Raman tensor keeps the same form. Setting the rotation angle between the lab frame and the crystal axes as α, the Raman tensor in the lab frame is given by

$$\chi'_{A_g} = Rot(-\alpha)\chi_{A_g}Rot(\alpha) = \chi_{A_g} \tag{6.3}$$

where $Rot(\alpha) = \begin{pmatrix} \cos\alpha & -\sin\alpha \\ \sin\alpha & \cos\alpha \end{pmatrix}$ is the rotation matrix. It is thus confirmed that the form of the A_g Raman tensor is independent of the reference frame.

We assume the Faraday rotation angles of both the incident and outgoing beam are β. The observed Raman intensity is

$$I_{VV/HV} = \left|\hat{e}_{V/H}Rot(\beta)\chi_{A_g}Rot(\beta)\hat{e}_V\right|^2 = \left|\hat{e}_{V/H}Rot(2\beta)\hat{e}_V\right|^2 = \cos/\sin^2 2\beta \tag{6.4}$$

Fitting the field-dependent mode intensities of the A_g phonons at 78 cm^{-1} and 128 cm^{-1} assuming a linear relation between β and external field B (Figure 6.4), we acquire β ~0.1 B where B is in tesla and β is in radian.

In reality, instead of correcting the mode intensities using the field-dependent Faraday angles we just unveiled, we choose to alter the experimental procedures, *i.e.* using circularly polarized light instead of linearly polarized light for selection rule measurements. The question naturally arises what the selection rules are of circularly polarized light of the C_{3i} point group. To solve this question, we can express the Raman intensity using circularly polarized light basis. The left and right circular polarizations are written as

$$\hat{L} = \frac{1}{\sqrt{2}}\begin{pmatrix} 1 \\ i \end{pmatrix} \text{ and } \hat{R} = \frac{1}{\sqrt{2}}\begin{pmatrix} 1 \\ -i \end{pmatrix} \tag{6.5}$$

in the Cartesian basis. Inserting Equation 6.5 into the Raman intensities given by $|\hat{e}_S^+ \cdot \chi \cdot \hat{e}_I|^2$, we find that A_g modes only show up in the symmetry channel with left and left circularly polarized light (LL) while E_g modes only show up in the symmetry channel with opposite circular polarizations of incident and scattered light (*i.e.* LR). In addition to the phonon modes with symmetric Raman tensors, we also find that the magnetic antisymmetric Raman tensor $\chi_M = \begin{pmatrix} \cdot & m \\ -m & \cdot \end{pmatrix}$ only show up in the LL channel. The selection rules in the circular polarization channels are summarized in Table 6.3. The validity of this result is confirmed with our data, which will be shown in the sections to follow.

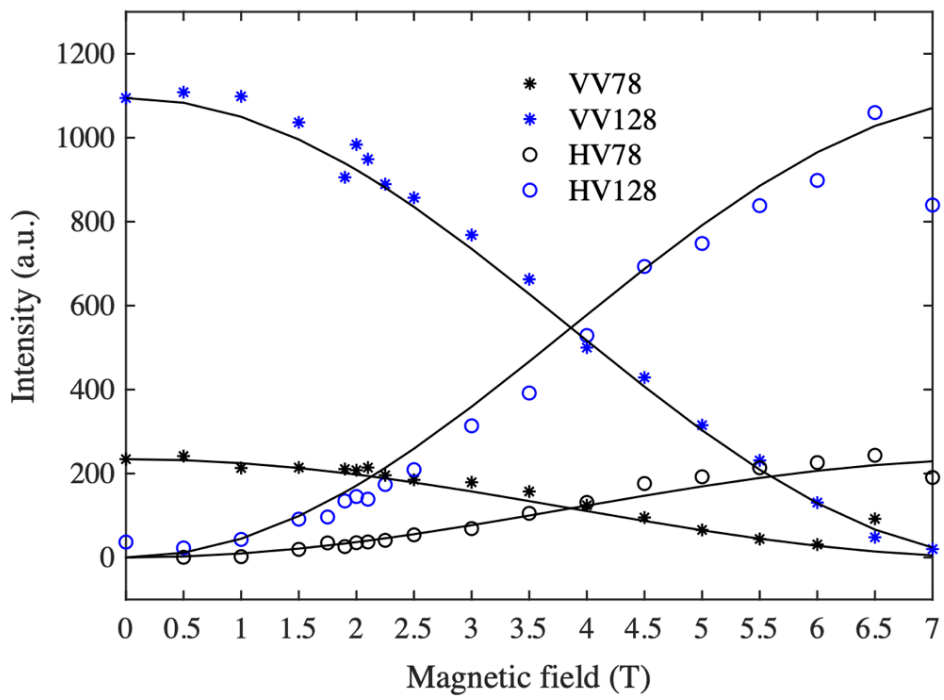

Figure 6.4 Fitting results (black solid lines) to the Raman intensities of the 78 cm^{-1} phonon in the VV/HV channel (black asterisk/circle) and the 128 cm^{-1} phonon in the VV/HV channel (blue asterisk/circle).

Table 6.3 The selection rules of the C_{3i} point group in the circular polarization channels

LL	LR
A_g, M	E_g

Our field-dependent Raman data at low temperature have unveiled a field-induced structural phase transition in CrI_3 from point group C_{3i} to C_{2h}. We thus also examine the selection rules of C_{2h}, which involve A_g and B_g modes. The Raman tensors and the selection rules in the circular polarization channels are summarized in Tables 6.4 and 6.5, respectively. The selection rules with linearly polarized light are irrelevant to our study, which is omitted here.

Table 6.4 Raman tensors of the point group C_{2h}

$$\begin{array}{cc} A_g & E_g \\ \begin{pmatrix} a_1 & b & \cdot \\ b & a_2 & \cdot \\ \cdot & \cdot & a_3 \end{pmatrix} & \begin{pmatrix} \cdot & \cdot & c_1 \\ \cdot & \cdot & c_2 \\ c_1 & c_2 & \cdot \end{pmatrix} \end{array}$$

Table 6.5 The selection rules of the C_{2h} point group in the circular polarization channels

LL	LR
A_g	A_g, B_g

6.2 Anomalous Magnetic Phonons in CrI_3

Having focused on the phonon modes with A_g and E_g symmetries, we move on to discuss two modes with an antisymmetric Raman tensor χ_M which are also present at 76 cm^{-1} and 125 cm^{-1} (M_1 and M_2 in Figure 6.2), as previously reported in CrI_3 thin layers [2]. Their integrated intensity and lifetime have been extracted whose turning points coincide with the AFM onset temperature T_N = 45 K (Figure 6.5). It has thus been proposed that both modes are long-lived magnons with rather high energies [2]. Our field-dependent study, however, provides direct evidence of the phononic nature of both modes.

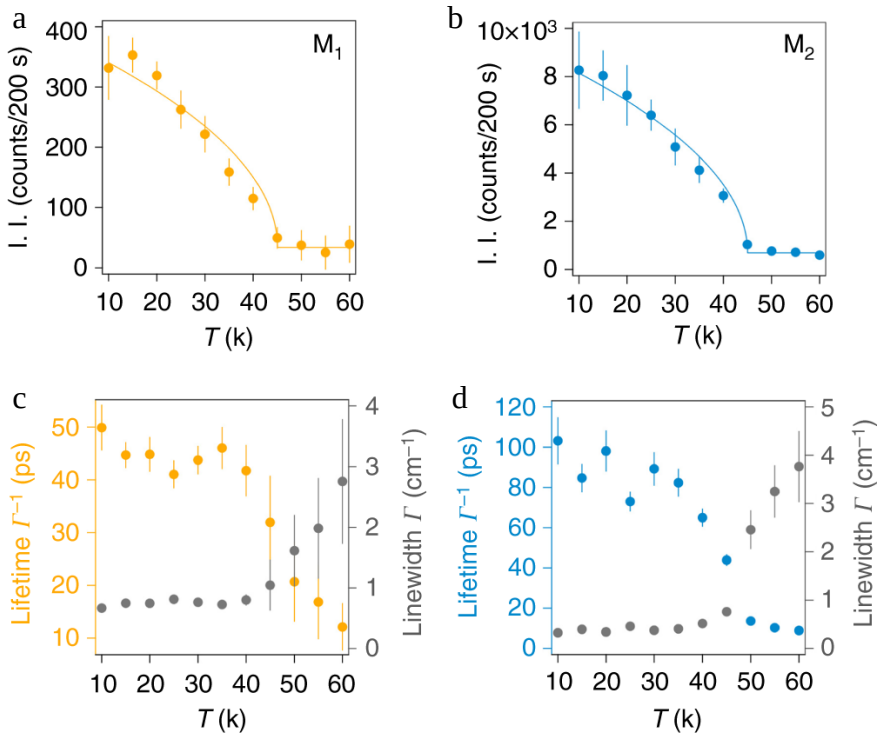

Figure 6.5 Extracted temperature-dependent integrated intensity (Panels a and b) and lifetime (Panels c and d) of magnetic modes M_1 (Panels a and c) and M_2 (Panels b and d), adapted from Reference [2].

Motived by this result, we have performed magnetic field-dependent Raman studies on bulk CrI_3. Figure 6.6 shows our circularly polarized Raman spectra acquired at zero magnetic field and low temperature, where M and A_g modes appear in the LL channel (yellow curves in Panels a and c) and E_g modes appear in the LR channel (blue curve in Panel b). The symmetry of the modes are fully consistent with the selection rules derived in Table 6.3.

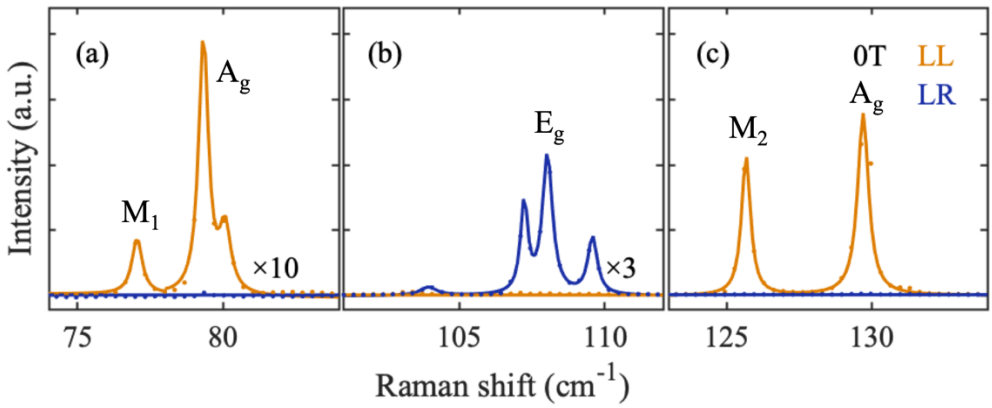

Figure 6.6 Raman spectra of bulk CrI_3 taken at 10 K and 0 T with circularly polarized light. LL (LR) channel is plotted in yellow (blue), adapted from Reference [14]. Panels a and c highlight modes with LL symmetry. Panel b highlights modes with LR symmetry.

Having established the validity of the selection rules of the circularly polarized light (Table 6.3), Raman measurements under finite magnetic field have been performed. Comparing with the large oscillatory intensities using linearly polarized light, circularly polarized light indeed significantly improves the fidelity of the spectrum. First, we focus on the selection rule of the A_g phonons. As shown in the third and fifth columns of Figure 6.7, the intensities of the A_g phonons remain in the LL channel albeit a small leakage to the LR channel, which will be explained in Section 6.3. Next, we examine the field response of M_1 and M_2. Although magnon energy (for example M_0 mode

shown in Fig 6.7) typically depends linearly on external field, the energies of M_1 and M_2 show no observable response from 0 T to 2 T, ruling out the magnonic nature of both modes.

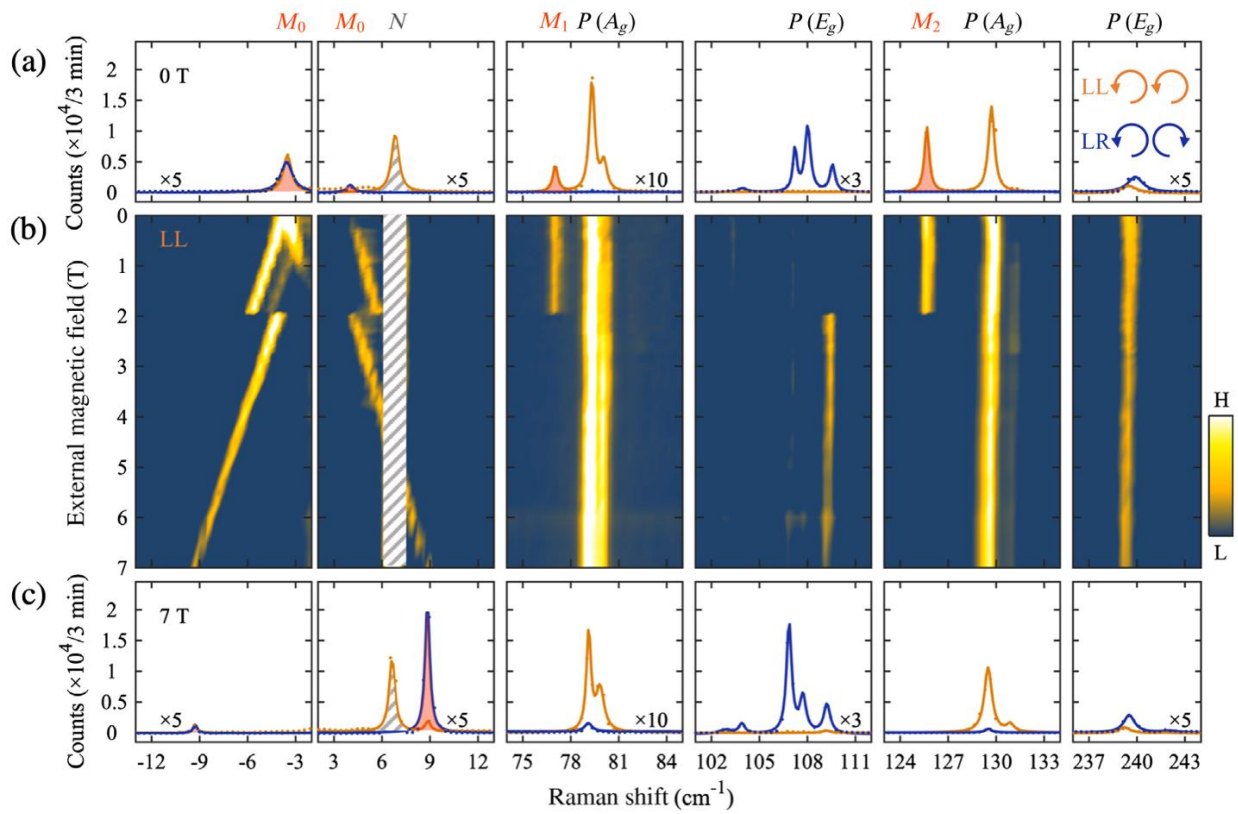

Figure 6.7 Magnetic field-dependent Raman data of bulk CrI_3 at 10 K, adapted from Reference [14]. Panel a and c display both LL and LR channels at 0 T and 7 T, respectively. Panel b is a colormap of the field dependence of the LL channel. The shaded area covers the laser artifact in the LL/parallel channel.

In Section 6.4, we will show that the low-field GS is a mixture of AFM and FM in bulk CrI_3, while the high-field GS is FM. Since both M_1 and M_2 disappear above B_C = 2 T, they are related to the AFM phase. Considering all the factors above, we bring up a new interpretation of the magnetic origin of M_1 and M_2, which will be discussed in the remaining part of this section.

We propose that M_1 and M_2 are originated from the paired excitations of c-axis zone-boundary phonons at $\vec{q} = (0, 0, k_c)$, $\Delta X_k^{\vec{q}}$, and the AFM order with momentum $-\vec{q}$, $M_l^{-\vec{q}}$, which has a zero total momentum to be a Raman-active mode. Note that the relevant zone-boundary phonons for M_1 and M_2 are two distinct phonon modes. The selection rule of this composite object ($\Delta X_k^{\vec{q}} M_l^{-\vec{q}}$) can be acquired by performing an expansion of the linear optical susceptibility (χ_{ij}) tensor with respect to both the phonon vibration and the magnetization. The induced change in linear optical susceptibility ($\Delta\chi_{ij}$) is

$$\Delta\chi_{ij} = \left.\frac{\partial^2 \chi_{ij}}{\partial X_k^{\vec{q}} \partial M_l^{-\vec{q}}}\right|_{\Delta X_k^{\vec{q}}=0, M_l^{-\vec{q}}=0} \Delta X_k^{\vec{q}} M_l^{-\vec{q}} = K_{ijkl} \Delta X_k^{\vec{q}} M_l^{-\vec{q}} \tag{6.6}$$

where K_{ijkl} is a polar tensor that is invariant under the symmetry operations of the lattice point group of C_{3i}, with 27 independent tensor elements [15],

$$K_{ijkl} =$$

$$\begin{pmatrix} \begin{pmatrix} K_{xxxx} & K_{xxxy} & K_{xxxz} \\ -K_{yyxy} & K_{xxyy} & -K_{yyyz} \\ K_{xxzx} & -K_{yyzy} & K_{yyzz} \end{pmatrix} & \begin{pmatrix} -K_{yxyy} & K_{xyxy} & -K_{yyyz} \\ K_{xyyx} & K_{xyyy} & -K_{xxxz} \\ -K_{yyzy} & -K_{xxzx} & K_{xyzz} \end{pmatrix} & \begin{pmatrix} K_{xzxx} & -K_{yzyy} & K_{xzxz} \\ -K_{yzyy} & -K_{xzxx} & K_{xzyz} \\ K_{yzzy} & K_{xzzy} & 0 \end{pmatrix} \\ \begin{pmatrix} -K_{xyyy} & K_{xyyx} & -K_{yyyz} \\ K_{xyxy} & K_{yxyy} & -K_{xxxz} \\ -K_{yyzy} & -K_{xxzx} & -K_{xyzz} \end{pmatrix} & \begin{pmatrix} K_{xxyy} & K_{yyxy} & -K_{xxxz} \\ -K_{xxxy} & K_{xxxx} & K_{yyyz} \\ -K_{xxzx} & K_{yyzy} & K_{yyzz} \end{pmatrix} & \begin{pmatrix} -K_{yzyy} & -K_{xzxx} & -K_{xzyz} \\ -K_{xzxx} & K_{yzyy} & K_{yzyz} \\ -K_{xzzy} & K_{yzzy} & 0 \end{pmatrix} \\ \begin{pmatrix} K_{zxxx} & -K_{zyyy} & K_{zyyz} \\ -K_{zyyy} & -K_{zxxx} & K_{zxyz} \\ K_{zyzy} & K_{zxzy} & 0 \end{pmatrix} & \begin{pmatrix} -K_{zyyy} & -K_{zxxx} & -K_{zxyz} \\ K_{zxxx} & K_{zyyy} & K_{zyyz} \\ -K_{zxzy} & K_{zyzy} & 0 \end{pmatrix} & \begin{pmatrix} K_{zzyy} & K_{zzxy} & 0 \\ -K_{zzxy} & K_{zzyy} & 0 \\ 0 & 0 & K_{zzzz} \end{pmatrix} \end{pmatrix}$$

(6.7)

The Onsager relation of $\Delta\chi_{ij}(\Delta\vec{X},\vec{M}) = \Delta\chi_{ji}(\Delta\vec{X},-\vec{M})$ [16,17] further constraints the form of Equation 6.7 and $\Delta\chi_{ij}(\Delta\vec{X},\vec{M})$ takes the following form

$$\begin{gathered}
\Delta\chi_{xx} = \Delta\chi_{yy} = \Delta\chi_{zz} = 0; \\
\Delta\chi_{yx} = -\Delta\chi_{xy} = -X_z M_z K_{xyzz} + \cdots \\
\frac{1}{2}\left[\left(X_y M_x - X_x M_y\right)\left(K_{xyxy} - K_{xyyx}\right) + \left(X_x M_x - X_y M_y\right)\left(K_{yxyy} - K_{xyyy}\right)\right]; \\
\\
\Delta\chi_{zx} = -\Delta\chi_{xz} = \frac{1}{2}\left[\left(X_x M_x - X_y M_y\right)(K_{zxxx} - K_{xzxx}) + \cdots\right. \\
\left(X_y M_x + X_x M_y\right)\left(K_{yzyy} - K_{zyyy}\right) + X_x M_z\left(K_{zyyz} - K_{xzxz}\right) + \cdots \\
\left. X_y M_z\left(K_{zxyz} - K_{xzyz}\right) + X_z M_x\left(K_{zyzy} - K_{yzzy}\right) + X_z M_y\left(K_{zxzy} - K_{xzzy}\right)\right]; \\
\Delta\chi_{zy} = -\Delta\chi_{yz} = \frac{1}{2}\left[\left(X_x M_x - X_y M_y\right)\left(K_{yzyy} - K_{zyyy}\right) + \cdots\right. \\
\left(X_y M_x + X_x M_y\right)(K_{xzxx} - K_{zxxx}) + X_x M_z\left(K_{xzyz} - K_{zxyz}\right) + \cdots \\
\left. X_y M_z\left(K_{zyyz} - K_{yzyz}\right) + X_z M_x\left(K_{xzzy} - K_{zxzy}\right) + X_z M_y\left(K_{zyzy} - K_{yzzy}\right)\right].
\end{gathered} \tag{6.8}$$

As shown in Equation 6.8, $\Delta\chi_{ij}$ is antisymmetric, so that the mode for such a composite object only shows up in the crossed channel with the linear polarization basis or the LL channel with the circular polarization basis.

6.3 Phonon Selection Rules: a Field-Induced Structural Phase Transition in CrI_3

Having analyzed the magnetic phonon modes at ~80 cm^{-1} and ~130 cm^{-1} in the third and fifth columns of Figure 6.7, we pay attention to the change of the phonon selection rules across B_C. The colormap of the LR channel is also shown in Figure 6.8. Firstly, we notice an E_g phonon at ~109 cm^{-1} which is present only in the LR channel under the C_{3i} point group also appears in the LL channel above B_C (the fourth panel of Figure 6.7 and Figure 6.9 b). Secondly, the A_g phonons at

~79 cm^{-1} and ~129 cm^{-1} appear in both LL and LR channel as well, in contrast to the low-field phase where only LL channel hosts A_g modes (the third and the fifth panels of Figure 6.8). For better illustrational purpose, we also extract and plot the intensity of the A_g phonons at ~129 cm^{-1} in Figure 6.9 a. Thirdly, the intensity of the E_g phonon at ~240 cm^{-1} decreases in the LR channel while remaining absent in the LL channel above B_C.

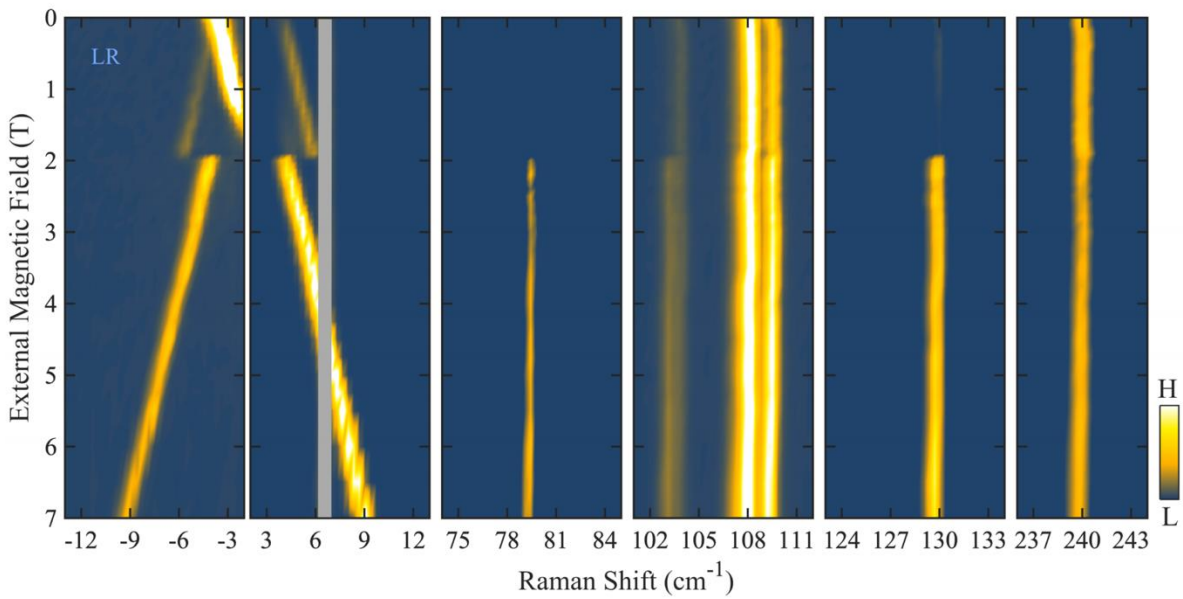

Figure 6.8 Magnetic field-dependent Raman spectra of bulk CrI_3 in LR channel at 10 K.

These results indicate the cooccurrence of a first-order structural phase transition and the AFM to FM magnetic phase transition at B_C. The leakage of the A_g phonons spectral weight from the LL into the LR channel suggests that the Raman tensor changes from $\begin{pmatrix} a_1 & \cdot \\ \cdot & a_1 \end{pmatrix}$ to $\begin{pmatrix} a_1 & \cdot \\ \cdot & a_2 \end{pmatrix}$ which is a result of breaking the three-fold rotational symmetry of the rhombohedral C_{3i} point group. The symmetry of CrI_3 thus shifts from the rhombohedral C_{3i} point group to the monoclinic C_{2h} point group, which also appears in the high-temperature phase [18]. Note that the Raman tensor

$\begin{pmatrix} a_1 & \cdot \\ \cdot & a_2 \end{pmatrix}$ is equivalent to the A_g Raman tensor $\begin{pmatrix} a_1 & b \\ b & a_2 \end{pmatrix}$ in Table 6.4 up to some rotational operations. A_g phonons in C_{3i} remain in the A_g symmetry in C_{2h} while the doubly degenerate E_g phonons transform to either A_g phonon or B_g phonon in C_{2h}. The three observations listed in the last paragraph correspond to different types of phonon transformations. Referring to Tables 6.3 and 6.5, the C_{3i} E_g phonons in the LR channel transform to either C_{2h} A_g phonon in both LL and LR channels, for example the 109 cm^{-1} phonon (Figure 6.9 b), or C_{2h} B_g phonon in the LR channel, for example the 240 cm^{-1} phonon (Figure 6.9 c).

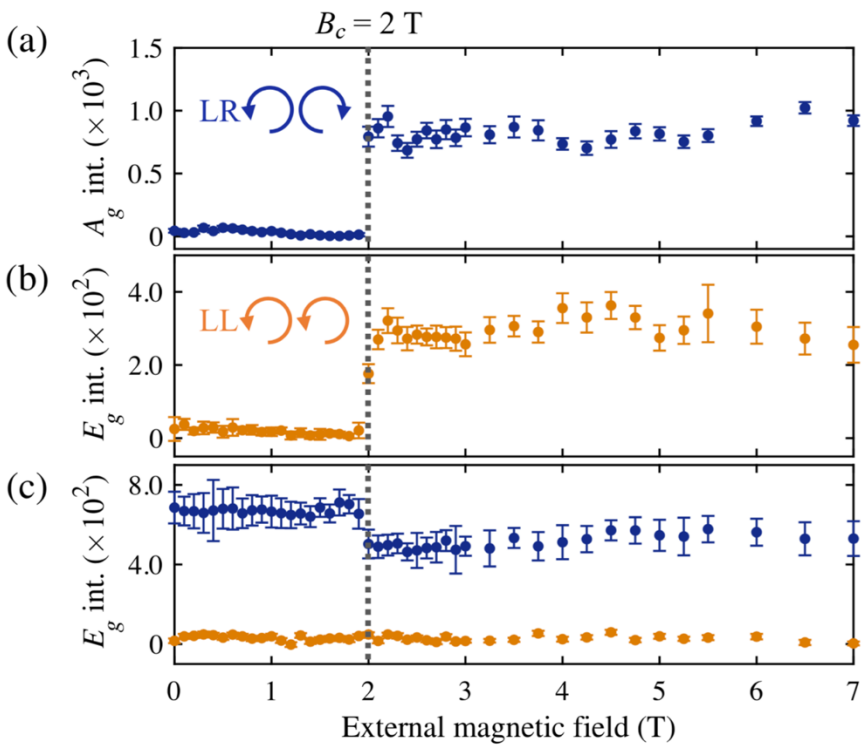

Figure 6.9 Field-dependent intensities of (a) A_g phonon at 129 cm^{-1} which leaks from the LL to LR channel, (b) E_g phonon at 109 cm^{-1} which leaks from the LR to LL channel, and (c) E_g phonon at 240 cm^{-1} showing a discontinuity in the LR channel but remaining absent in the LL channel. This figure is adapted from Reference [14].

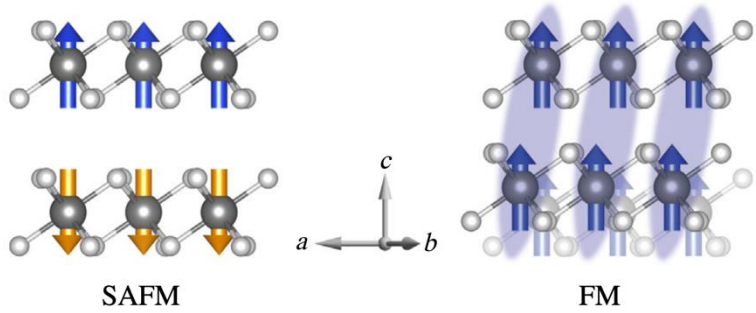

Figure 6.10 Schematics of the field-induced C_{3i} AFM to the C_{2h} FM phase transition: shearing of the layers, adapted from Reference [14]. SAFM refers to surface-AFM which will be discussed in Section 6.4.

We further propose that the structural phase transition from rhombohedral C_{3i} to monoclinic C_{2h} is due to a shearing between the layers away from the ABC stacking which breaks the three-fold rotational symmetry [18,19], as illustrated in Figure 6.10.

6.4 Field-Dependent Magnon Behavior: a Mixed SAFM and BFM in bulk CrI_3

As we have introduced in Chapter 2, CrI_3 has been considered to be an interlayer AFM in its few-layer form and an interlayer FM in its bulk [20-23], while our study shows the coexistence of AFM and FM magnons even in bulk CrI_3. We propose that this interlayer AFM resides at the surface (referred to as SAFM) of the FM CrI_3 bulk. In this section, we will discuss how we unveil this interesting result using the low-energy part of the field-dependent Raman data.

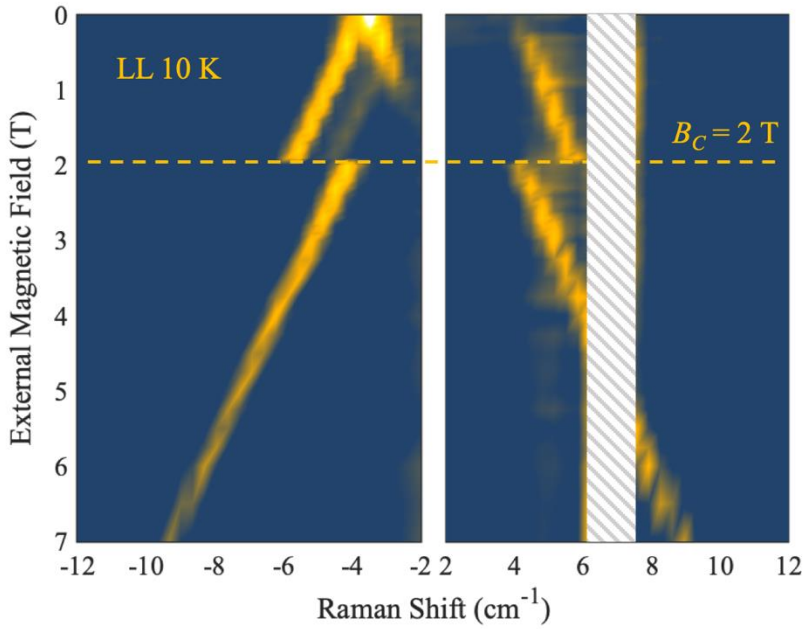

Figure 6.11 Field-dependent low-energy anti-Stokes and Stokes Raman data highlighting M_0 modes in the LL channel at 10 K. The shaded area blocks the laser artifact. The dashed line marks the transition field B_C = 2 T. Below B_C three magnon branches are clearly visible while only one magnon branch is present above B_C.

We zoom in the low-energy Raman data of Figure 6.7 and plot them in Figure 6.11. The energies of M_0 modes show clear linear dependence of the external magnetic field, typical of the magnons. More intriguingly three magnon branches are present below B_C, two of which harden with external field (spin +1) and one of which softens with external field (spin -1). Because a pair of magnons with spin ±1 must result from AFM GS, the presence of such three magnon branches is a clear signature of the coexistence of the interlayer AFM and FM within the bulk CrI_3. Above B_C, only one magnon branch remains with spin -1 indicating a transition to FM.

Temperature-dependent data shown in Figure 6.12 clearly shows that the energy of M_0 decreases with increasing temperature towards the magnetic critical temperature of T_C = 45 K, which is also

consistent with our assignment of M_0 being magnon excitations. Panel b plots the extracted magnon energies fitted with the mean-field scaling law $\sqrt{T_C - T}$, where T_C = 45 K.

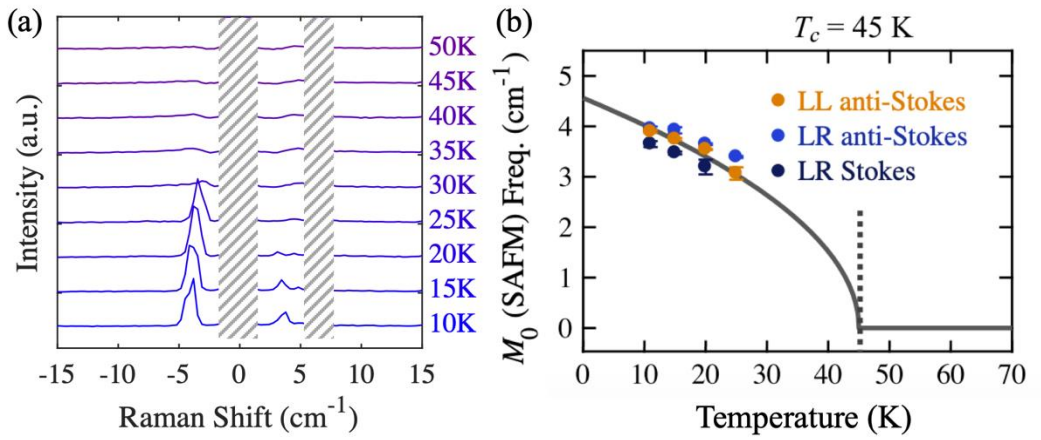

Figure 6.12 (a) Low-energy temperature-dependent Raman data of bulk CrI_3 in the LR channel. Shaded area blocks the Rayleigh scattering and the laser artifact. (b) Extracted zero-field M_0 frequencies fitted with the mean-field relation (solid line), adapted from Reference [14].

We propose that the AFM resides on the surface of the bulk CrI_3 because of surface reconstructions where a change in layer distance can result in this FM to AFM transition on the surface. We rule out the possibility of magnetic dipole-dipole interaction, because its energy scale of 1 μeV [24] is negligible compared with the exchange energies, although magnetic dipole-dipole interaction favors FM order. The mixed SAFM and BFM of the bulk CrI_3 gives a natural explanation to its thickness-dependent magnetic GS. Raman spectroscopy is ideal to probe this mixed state because of the finite penetration depth of optical techniques, which is estimated to be 30 layers at 633 nm excitation wavelength based on the optical absorption data of thin layers of CrI_3.

To gain a qualitative understanding of the field evolution of M_0, the field-dependent magnon energies have been extracted and plotted on the left panel of Figure 6.13, and the right panel shows the calculated energies using the standard spin-wave theory of a 3D magnet made of ABC-stacked 2D honeycomb magnetic lattices. The theory and experiment data show remarkable consistency. Details of the calculations are as follow.

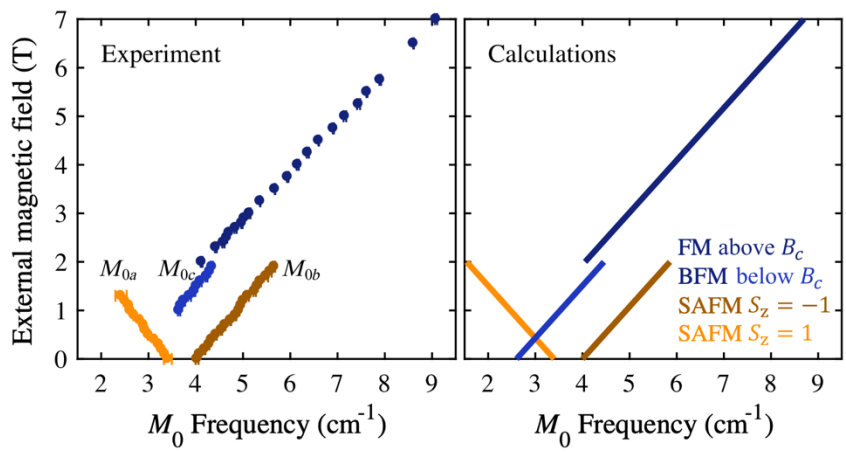

Figure 6.13 Experimental (left) and calculated (right) field-dependent magnon energies, adapted from Reference [14].

For the SAFM state, the spin Hamiltonian includes interlayer AFM exchange coupling and intralayer FM exchange coupling

$$
\begin{aligned}
H &= H_0 + H_C + H_Z \\
H_0 &= -\frac{1}{2}\sum_{l,<i,j>}[J_z S_{l,i}^z S_{l,j}^z + J_x(S_{l,i}^x S_{l,j}^x + S_{l,i}^y S_{l,j}^y)] \\
H_C &= \frac{1}{2}J_C \sum_{i,<l,l'>} \vec{S}_{l,i} \cdot \vec{S}_{l',j} \\
H_Z &= -g\mu_B B \sum_{l,i} S_{l,i}^z
\end{aligned}
\tag{6.9}
$$

where $J_{x,z} > 0$ and $J_C > 0$ are intra- and inter-layer exchange couplings, respectively, $S_{l,i}^{x(y,z)}$ is the x (y, z)-component of the spin at site i of layer l, B is the strength of the external magnetic field along the z-direction, and H_0, H_C, and H_Z are spin Hamiltonians for the intralayer FM interactions, intralayer AFM interactions, and Zeeman energy.

There are four different spin sites per magnetic unit cell in SAFM. After applying the Holstein-Primakoff transformation and the Bogoliubov transformation, the Γ-point magnon energies are acquired as

$$\begin{aligned} E_1 &= \frac{1}{2}S\sqrt{(J_z - J_x)z[4J_C + (J_z - J_x)z]} \pm g\mu_B B; \\ E_2 &= \frac{1}{2}S\sqrt{(J_z + J_x)z[4J_C + (J_z + J_x)z]} \pm g\mu_B B. \end{aligned} \tag{6.10}$$

where z = 3 is the number of NN. When B = 0 T, each branch is doubly degenerate with one magnon carrying spin +1 and the other spin -1. The presence of an external field lifts this degeneracy, and magnons with opposite spins undergo Zeeman shifts in opposite trends with the same rate (*i.e.*, the slope of $\pm g\mu_B$).

In the mixed SAFM and BFM state of 3D CrI_3, the BFM provides an effective magnetic field B_0 to the SAFM even when there is no external field. This results in the slight splitting of the two magnons per branch at 0 T. In our experimental data, the magnon branch we observed is the acoustic branch E_1 whose field dependence is shown in Figure 12 and labeled with the SAFM.

Considering the BFM below 2 T or the FM above 2 T, we calculation the magnon energy using FM interlayer coupling, and there are only two inequivalent spin sites. They correspond to one

acoustic and one optical branch at 0 T, but are both spin -1 without any degeneracy. Experimentally, we observed the acoustic branch labeled as BFM in Figure 6.12. The interlayer exchange coupling J_C is no longer the same as in Equation 6.9, but this has no impact on the magnetic field dependence of the acoustic branch which takes the following form

$$E_1' = \frac{1}{2}Sz(J_z - J_x) + g\mu_B B. \tag{6.11}$$

Comparing E_1' with E_1, the magnon with spin -1 of BFM has smaller energy than that of SAFM, which is indeed consistent with our experimental observation.

By comparing our calculated and experimental magnon energies, we have extracted the following important parameters:

- Below 2 T:

  Interlayer exchange coupling: J_C = 0.15 meV

  Intralayer exchange anisotropy: $J_z - J_x$ = 0.13 meV

  Effective magnetic field from the BFM at 0 T external field: B_0 = 0.32 T

- Above 2 T:

  Intralayer exchange anisotropy: $J_z - J_x$ = 0.11 meV.

Given the fact that only the acoustic magnon branch is probed experimentally, we can only extract the intralayer exchange anisotropy $J_z - J_x$, but not the individual values of J_x and J_z.

Apart from studying magnetic excitations, we can also estimate the interlayer exchange coupling J_C using the magnetic transition field of 2 T. The AFM interlayer exchange coupling favors spins

in adjacent layers aligning along opposite directions, whereas the external field favors all the spins aligning along the field direction. From Equation 6.9, the GS energies of SAFM and FM per spin are given in Table 6.6.

The magnetic phase transition happens when the total energy of FM becomes lower than that of the SAFM. With B_C = 2 T, we get J_C = 0.15 meV, which corroborates the previous result of J_C = 0.15 meV obtained using magnon energies.

Table 6.6 Analytic forms of the SAFM and FM interlayer energies H_C and Zeeman energies H_Z

	SAFM	FM
H_C	$-\frac{1}{2}S^2J_C$	$\frac{1}{2}S^2J_C$
H_Z	0	$-g\mu_B BS$

As a closing remark, we comment on the selection rule of M_0. Although M_0 modes are assigned as single magnon excitations, they show up in both LL and LR channels (Figure 6.12 b), in contrast to the selection rules in Table 6.3. As introduced in Section 3.2, the fact that M modes appear in the LL channel assumes that the change in electric susceptibility tensor is linear to magnon-induced magnetization. In CrI_3, however, a linear expansion is not sufficient so that we derive the Raman tensor of a quadratic expansion.

The response of the linear electric susceptibility tensor to the quadratic magnetization is a 4th rank tensor $\chi^{(2)}$. We impose the following constraints to $\chi^{(2)}$:

- $\chi^{(2)}$ is invariant under all the symmetry operations of the crystal point group C_{3i}.

- $\chi^{(2)}_{ijkl} = \chi^{(2)}_{ijlk}$ because the 3rd and 4th components are multiplied by the same vector of induced magnetization which obey permutation invariance.

- The Onsager relation requires that $\chi^{(2)}_{ij}(\vec{M},\vec{M}) = \chi^{(2)}_{ji}(-\vec{M},-\vec{M})$ where $\vec{M}$ is the induced magnetization.

We thus acquire the form of $\chi^{(2)}_{ij}(\vec{M},\vec{M})$, a 2nd rank tensor, following the constraints above. Because this matrix is too large, we write down each tensor element individually

$$\begin{gathered}
\chi^{(2)}_{xx}(\vec{M},\vec{M}) = M_y^2\chi^{(2)}_{xxyy} + 2M_xM_z\chi^{(2)}_{xxzx} + M_x^2\left(\chi^{(2)}_{xxyy} + 2\chi^{(2)}_{xyxy}\right) + M_z^2\chi^{(2)}_{yyzz} \\
\chi^{(2)}_{xy}(\vec{M},\vec{M}) = \chi^{(2)}_{yx}(\vec{M},\vec{M}) = 2M_y\left(M_x\chi^{(2)}_{xyxy} - M_z\chi^{(2)}_{xxzx}\right) \\
\chi^{(2)}_{yy}(\vec{M},\vec{M}) = M_x^2\chi^{(2)}_{xxyy} - 2M_xM_z\chi^{(2)}_{xxzx} + M_y^2\left(\chi^{(2)}_{xxyy} + 2\chi^{(2)}_{xyxy}\right) + M_z^2\chi^{(2)}_{yyzz} \\
\chi^{(2)}_{zy}(\vec{M},\vec{M}) = \chi^{(2)}_{yz}(\vec{M},\vec{M}) = M_y\left[M_z(\chi^{(2)}_{yzyz} + \chi^{(2)}_{zyzy}) - M_x(\chi^{(2)}_{xzxx} + \chi^{(2)}_{zxxx})\right] \\
\chi^{(2)}_{zz}(\vec{M},\vec{M}) = (M_x^2 + M_y^2)\chi^{(2)}_{zzyy} + M_z^2\chi^{(2)}_{zzzz} \\
\chi^{(2)}_{zx}(\vec{M},\vec{M}) = \chi^{(2)}_{xz}(\vec{M},\vec{M}) = \frac{1}{2}[(M_x^2 - M_y^2)(\chi^{(2)}_{xzxx} + \chi^{(2)}_{zxxx}) + 2M_xM_z(\chi^{(2)}_{yzyz} + \chi^{(2)}_{zyzy})]
\end{gathered} \tag{6.12}$$

Because CrI_3 is a z-axis Ising FM, its magnon excitation induces xy-plane magnetization. With $M_z = 0$, $\chi^{(2)}_{ij}(\vec{M},\vec{M})$ is reduced to

$$\begin{pmatrix}
M_y^2\chi^{(2)}_{xxyy} + M_x^2\left(\chi^{(2)}_{xxyy} + 2\chi^{(2)}_{xyxy}\right) & 2M_yM_x\chi^{(2)}_{xyxy} & \frac{1}{2}(M_x^2 - M_y^2)(\chi^{(2)}_{xzxx} + \chi^{(2)}_{zxxx}) \\
2M_yM_x\chi^{(2)}_{xyxy} & M_x^2\chi^{(2)}_{xxyy} + M_y^2\left(\chi^{(2)}_{xxyy} + 2\chi^{(2)}_{xyxy}\right) & -M_xM_y(\chi^{(2)}_{xzxx} + \chi^{(2)}_{zxxx}) \\
\frac{1}{2}(M_x^2 - M_y^2)(\chi^{(2)}_{xzxx} + \chi^{(2)}_{zxxx}) & -M_xM_y(\chi^{(2)}_{xzxx} + \chi^{(2)}_{zxxx}) & (M_x^2 + M_y^2)\chi^{(2)}_{zzyy}
\end{pmatrix} \tag{6.13}$$

Combining both linear and quadratic expansions in magnetization, it is not surprising that single magnons in CrI_3 show up in both LL and LR channels.

6.5 Calculations of the X-Dependent Magnetism in CrX_3 (X = Cl, Br, I)

In this last section, we present our study of the field-dependent magnon in atomically thin CrX_3 (X = Cl, Br, I) [25]. This is a highly collaborative work where Professor Adam Wei Tsen's group at the University of Waterloo performs inelastic electron tunneling measurements, and our group is responsible for the spin-wave calculations, which will be presented in detail below.

6.5.1 Spin Hamiltonian of a 2D Honeycomb FM

We perform spin-wave calculations with an external magnetic field for monolayer honeycomb magnets CrX_3. Here our spin Hamiltonian only considers a monolayer spin lattice because interlayer interactions (J_C = 0.15 meV as determined in Section 6.4) are negligible compared to intralayer exchange interactions (J ~1-2 meV). Although the Raman data shows clear signature of field-induced breaking of the two-fold degeneracy of AFM magnons, there is no evidence of interlayer AFM in the inelastic electron tunneling measurement.

We construct the anisotropic Heisenberg spin model

$$H = -J\sum_{<i,j>}\left(S_i^x S_j^x + S_i^y S_j^y + \alpha S_i^z S_j^z\right) - g\mu_B\left(B_z\sum_i S_i^z + B_x\sum_i S_i^x\right) \tag{6.14}$$

where J is the NN exchange energy, i and j denote the two inequivalent nearest Cr^{3+} site, and α scales the z-direction exchange strength. In particular, α is greater than, equivalent to, or smaller than 1 for Ising, isotropic Heisenberg, or XY magnets, respectively. g is the g-factor for Cr^{3+} magnetic moments, μ_B is the Bohr magneton, and $\vec{B}$ is external magnetic field. Depending on the experimental geometry, either B_z or B_x is nonzero, representing the magnetic field perpendicular to or parallel to the plane of CrX_3 layers.

Without external magnet field, the spins in CrX_3 align either along the z-axis or in the xy-plane depending on the magnitude of α. When a field is applied perpendicular to the easy axis or easy plane, it tilts the spins to a new direction that minimizes the energy (Equation 6.15). To keep it general for all three types of magnets, we characterize the spin orientation by its tilt angle from the z-axis, θ. $\theta = 0$ corresponds to the spins along the z-axis and $\theta = \pi/2$ for spins in the xy-plane. To determine θ for a given external magnetic field, a rotational transform is applied, where $\vec{\tilde{S}}$ is the spin orientation in the new ground state under the external field

$$\begin{aligned} S^x &= \tilde{S}^x cos\theta + \tilde{S}^z sin\theta \\ S^z &= -\tilde{S}^x sin\theta + \tilde{S}^z cos\theta \end{aligned} \tag{6.15}$$

After applying Holstein-Primakoff transform for both site i and site j

$$\begin{aligned} \tilde{S}^z &= S - a^\dagger a \\ \tilde{S}^+ &= \sqrt{2S}\left(1 - \frac{a^\dagger a}{2S}\right)a \\ \tilde{S}^- &= \sqrt{2S}a^\dagger \end{aligned} \tag{6.16}$$

we arrive at the following Hamiltonian where magnon interactions are ignored

$$H = H_{const} + H_1 + H_2 \tag{6.17}$$

$$H_{const} = -SN[JzS(\alpha \cos^2\theta + \sin^2\theta) + 2g\mu_B(sin\theta B_x + cos\theta B_z)]$$

$$H_1 = \left[\frac{1}{2}JSz(\alpha-1)sin2\theta + g\mu_B(B_z sin\theta - B_x cos\theta)\right]\sqrt{S/2}\sum_i (a_i^\dagger + a_i)$$

$$H_2 = -\frac{1}{2}JS(\alpha\sin^2\theta + \cos^2\theta - 1)\sum_{<i,j>}\left(a_i^\dagger b_j^\dagger + a_i b_j\right)$$

$$-\frac{1}{2}JS(\alpha\sin^2\theta + \cos^2\theta + 1)\sum_{<i,j>}\left(a_i^\dagger b_j + a_i b_j^\dagger\right)$$

$$+JS(\alpha\cos^2\theta + \sin^2\theta)\sum_{<i,j>}(a_i^\dagger a_i + b_j^\dagger b_j)$$

$$+g\mu_B(sin\theta B_x + cos\theta B_z)(\sum_i a_i^\dagger a_i + \sum_j b_j^\dagger b_j)$$

where N is the number of sublattices, and z is the number of NN spins. Minimizing H_{const} yields the new spin orientation θ and eliminates H_1. If $\vec{B}$ is parallel to the original spin orientation, the spin directions remain the same. If $\vec{B}$ is perpendicular, θ can be expressed as a function of $|\vec{B}|$. At low field,

$$\theta = \sin^{-1}\frac{g\mu_B B_x}{JSz(\alpha-1)}\ (B_z = 0, \alpha > 1) \tag{6.18}$$

and

$$\theta = \cos^{-1}\frac{g\mu_B B_z}{JSz(1-\alpha)}\ (B_x = 0, \alpha < 1) \tag{6.19}$$

A critical field strength B_C exists above which the spins are completely aligned along the external field direction.

To obtain the spin-wave dispersions under external magnetic field, Fourier and Bogoliubov transformations are applied to H_2. Fourier transform yields

$$H_2 = Q_1\sum_k\left(a_k^\dagger b_{-k}^\dagger\gamma_{-k} + a_k b_{-k}\gamma_k\right) + Q_2\sum_k\left(a_k^\dagger b_k\gamma_{-k} + a_k b_k^\dagger\gamma_k\right) + Q_3\sum_k\left(a_k^\dagger a_k + b_k^\dagger b_k\right) \tag{6.20}$$

where

$$\gamma_k = \frac{1}{z}\sum_{\delta} e^{ik\delta}$$
$$Q_1 = -\frac{1}{2}JSz(\alpha\sin^2\theta + \cos^2\theta - 1)$$
$$Q_2 = -\frac{1}{2}JSz(\alpha\sin^2\theta + \cos^2\theta + 1)$$
$$Q_3 = JSz(\alpha\cos^2\theta + \sin^2\theta) + g\mu_B(sin\theta B_x + cos\theta B_z)$$

a_k and b_k correspond to the Fourier-transformed spin-wave operators of real-space operators a_i and b_j, respectively. Bogoliubov transform for bosonic excitations is applied

$$\begin{pmatrix} \phi_{-k} \\ \psi_{-k} \\ \phi_k^\dagger \\ \psi_k^\dagger \end{pmatrix} = M \begin{pmatrix} a_{-k} \\ b_{-k} \\ a_k^\dagger \\ b_k^\dagger \end{pmatrix} \tag{6.21}$$

where

$$M = \begin{pmatrix} \frac{Q_3 - Q_2P_1 - P_2}{Q_1\gamma_k} & -\frac{Q_3 - Q_2P_1 - P_2}{Q_1P_1} & -\sqrt{\frac{\gamma_{-k}}{\gamma_k}} & 1 \\ \frac{Q_3 + Q_2P_1 - P_3}{Q_1\gamma_k} & \frac{Q_3 + Q_2P_1 - P_3}{Q_1P_1} & \sqrt{\frac{\gamma_{-k}}{\gamma_k}} & 1 \\ \frac{Q_3 - Q_2P_1 + P_2}{Q_1\gamma_k} & -\frac{Q_3 - Q_2P_1 + P_2}{Q_1P_1} & -\sqrt{\frac{\gamma_{-k}}{\gamma_k}} & 1 \\ \frac{Q_3 + Q_2P_1 - P_3}{Q_1\gamma_k} & \frac{Q_3 + Q_2P_1 - P_3}{Q_1P_1} & \sqrt{\frac{\gamma_{-k}}{\gamma_k}} & 1 \end{pmatrix}$$

and

$$P_1 = \sqrt{\gamma_k\gamma_{-k}}$$
$$P_2 = \sqrt{Q_3^2 - 2Q_3Q_2P_1 + (Q_2^2 - Q_1^2)P_1^2}$$
$$P_3 = \sqrt{Q_3^2 + 2Q_3Q_2P_1 + (Q_2^2 - Q_1^2)P_1^2}$$

M is the Bogoliubov transform matrix under which the new operators ϕ_k and ψ_k satisfy bosonic commutation relations up to a normalization factor. Finally, spin-wave dispersions as a function of external field strength can be obtained as

$$\begin{aligned} E_1 &= P_2 \\ E_2 &= P_3 \end{aligned} \tag{6.22}$$

If $\vec{B}$ is parallel to the original spin orientation, spin-wave energies increase by $g\mu_B|\vec{B}|$. If $\vec{B}$ is perpendicular, spin-wave energies show an anomaly at B_C, consistent with the inelastic electron tunneling results shown in Figure 6.14.

6.5.2 Comparison with Inelastic Electron Tunneling Measurements

Having acquired the functional forms of the field-dependent magnon dispersions, we compare them with the inelastic electron tunneling measurements to extract important spin-wave parameters in the family of CrX_3. Due to high spin-wave DOS at Γ- and M-points (because of the flat energy dispersions around Γ- and M-points, as evident from References [2,26]), the experimentally observed peaks (Panel A of Figure 6.14) are mainly related with two Γ-point excitations and two M-point excitations. The functional forms of field-dependent Γ- and M-point magnon energies and the transition fields B_C can be obtained from Equations 6.22, 6.18 and 6.19.

If $\alpha > 1$, the transition field is

$$B_C = \frac{JSz(\alpha - 1)}{g\mu_B} \tag{6.23}$$

and the zero-field magnon energies are

$$\begin{aligned} \Gamma_- &= JSz(\alpha - 1) \\ \Gamma_+ &= JSz(\alpha + 1) \\ M_- &= \frac{1}{3}JSz(3\alpha - 1) \\ M_+ &= \frac{1}{3}JSz(3\alpha + 1) \end{aligned} \tag{6.24}$$

If $\alpha < 1$, the transition field is

$$B_C = \frac{JSz(1-\alpha)}{g\mu_B} \tag{6.25}$$

and the zero-field magnon energies are

$$\begin{aligned} \Gamma_- &= 0 \\ \Gamma_+ &= JSz\sqrt{2(\alpha + 1)} \\ M_- &= \frac{2}{3}JSz\sqrt{\frac{3-\alpha}{2}} \\ M_+ &= \frac{2}{3}JSz\sqrt{3 + \alpha} \end{aligned} \tag{6.26}$$

For Cr^{3+}, the spin angular moment is $S = 3/2$. In the honeycomb lattice, the number of NN is $z = 3$. At large fields, the spin-wave energies increase by $g\mu_B B$. g-factor is then extracted from the slope of the spin-wave energies as a function of external field. g is taken to be 2.1788, which is the average of the slopes of all three compounds.

To acquire the values of the two free parameters J and α, we can further use the transition fields B_C and the zero-field magnon energies from the field-dependent inelastic electron tunneling

spectroscopy to identify their values by fitting experimental results. Table 6.7 summarizes B_C, J and α for all three compounds determined from experiments.

Table 6.7 Spin-wave parameters in CrX_3 compounds

Compound	B_C (T)	J (meV)	α
CrI_3	3.63	2.286	1.0445
$CrBr_3$	0.44	1.562	1.0079
$CrCl_3$	0.23	0.9208	0.9930

We can further compare the obtained spin-wave parameters of CrI_3 with previous Raman experiments. The intralayer exchange anisotropy determined from inelastic electron tunneling data is $J(1-\alpha)$ = 0.10 meV, consistent with $J_z - J_x$ = 0.13 meV calculated based on Raman results, as discussed in Section 6.4.

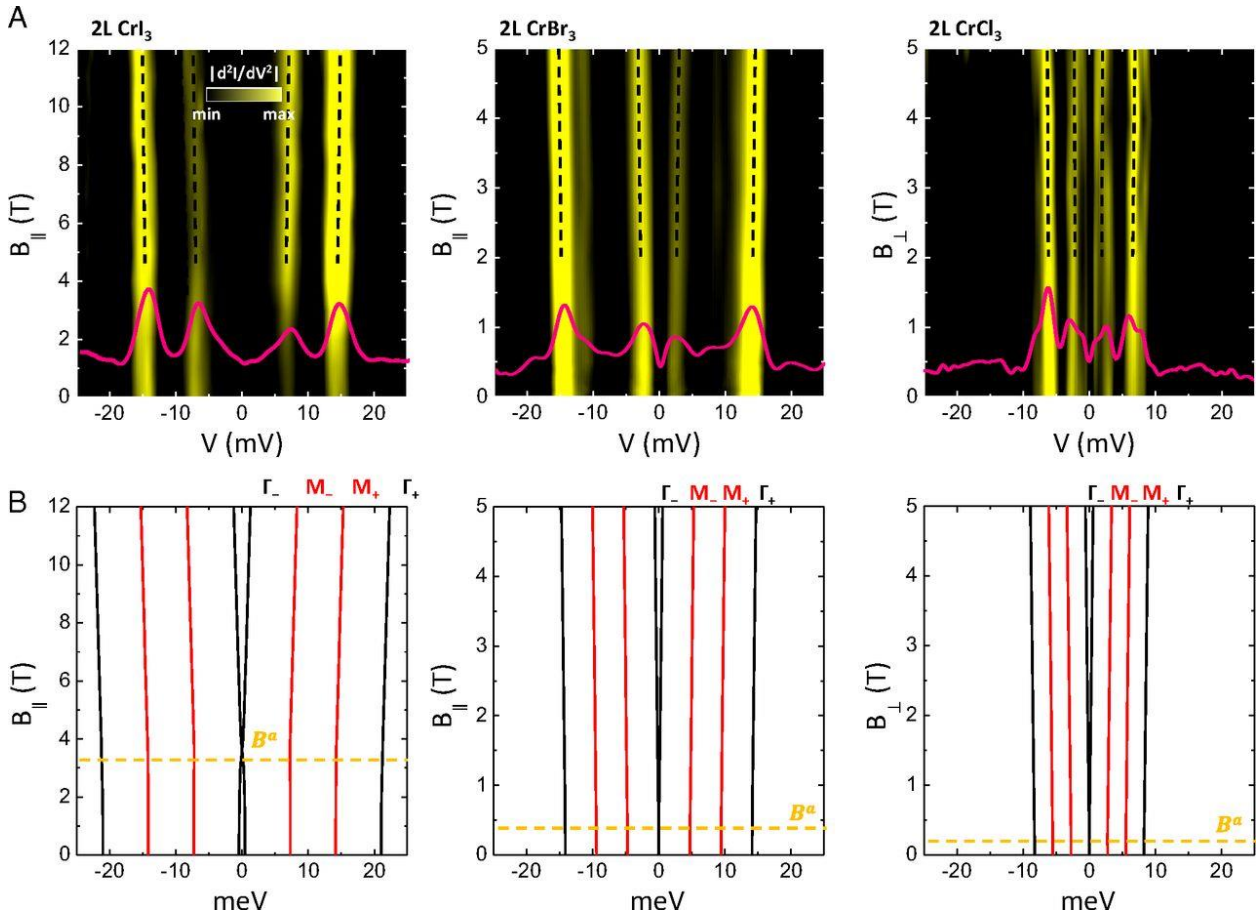

Figure 6.14 (A) Field-dependent inelastic tunneling data of bilayer CrX_3. (B) Spin-wave calculations of field-dependent *Γ*- and *M*-point magnon energies. This figure is adapted from Reference [25].

References

[1] N. Ubrig, Z. Wang, J. Teyssier, T. Taniguchi, K. Watanabe, E. Giannini, A. F. Morpurgo, and M. Gibertini, *Low-temperature monoclinic layer stacking in atomically thin CrI_3 crystals*, 2D Materials **7**, 015007 (2019).

[2] W. Jin *et al.*, *Raman fingerprint of two terahertz spin wave branches in a two-dimensional honeycomb Ising ferromagnet*, Nature communications **9**, 1 (2018).

[3] A. McCreary *et al.*, *Distinct magneto-Raman signatures of spin-flip phase transitions in CrI_3*, Nature communications **11**, 1 (2020).

[4] Y. Zhang *et al.*, *Magnetic order-induced polarization anomaly of Raman scattering in 2D magnet CrI_3*, Nano letters **20**, 729 (2019).

[5] B. Huang *et al.*, *Tuning inelastic light scattering via symmetry control in the two-dimensional magnet CrI_3*, Nature nanotechnology **15**, 212 (2020).

[6] W. Jin *et al.*, *Tunable layered-magnetism–assisted magneto-Raman effect in a two-dimensional magnet CrI_3*, Proceedings of the National Academy of Sciences **117**, 24664 (2020).

[7] Z. Liu *et al.*, *Observation of nonreciprocal magnetophonon effect in nonencapsulated few-layered CrI_3*, Science advances **6**, eabc7628 (2020).

[8] T. Li *et al.*, *Pressure-controlled interlayer magnetism in atomically thin CrI_3*, Nature materials **18**, 1303 (2019).

[9] D. T. Larson and E. Kaxiras, *Raman spectrum of CrI_3: An ab initio study*, Physical Review B **98**, 085406 (2018).

[10] M. Lei and S. Coh, *Large cross-polarized Raman signal in CrI_3: A first-principles study*, Physical Review Materials **5**, 025202 (2021).

[11] S. Djurdjić-Mijin, A. Šolajić, J. Pešić, M. Šćepanović, Y. Liu, A. Baum, C. Petrovic, N. Lazarević, and Z. Popović, *Lattice dynamics and phase transition in CrI_3 single crystals*, Physical Review B **98**, 104307 (2018).

[12] R. Loudon, *The Raman effect in crystals*, Advances in Physics **13**, 423 (1964).

[13] W. Hayes and R. Loudon, *Scattering of light by crystals* (Courier Corporation, 2012).

[14] S. Li *et al.*, *Magnetic-field-induced quantum phase transitions in a van der Waals magnet*, Physical Review X **10**, 011075 (2020).

[15] R. W. Boyd, *Nonlinear optics* (Elsevier, 2003).

[16] L. D. Landau, J. Bell, M. Kearsley, L. Pitaevskii, E. Lifshitz, and J. Sykes, *Electrodynamics of continuous media* (elsevier, 2013), Vol. 8.

[17] W. Wettling, M. Cottam, and J. Sandercock, *The relation between one-magnon light scattering and the complex magneto-optic effects in YIG*, Journal of Physics C: Solid State Physics **8**, 211 (1975).

[18] M. A. McGuire, H. Dixit, V. R. Cooper, and B. C. Sales, *Coupling of crystal structure and magnetism in the layered, ferromagnetic insulator* CrI_3, Chemistry of Materials **27**, 612 (2015).

[19] N. Sivadas, S. Okamoto, X. Xu, C. J. Fennie, and D. Xiao, *Stacking-dependent magnetism in bilayer* CrI_3, Nano letters **18**, 7658 (2018).

[20] B. Huang *et al.*, *Layer-dependent ferromagnetism in a van der Waals crystal down to the monolayer limit*, Nature **546**, 270 (2017).

[21] T. Song *et al.*, *Giant tunneling magnetoresistance in spin-filter van der Waals heterostructures*, Science **360**, 1214 (2018).

[22] D. R. Klein *et al.*, *Probing magnetism in 2D van der Waals crystalline insulators via electron tunneling*, Science **360**, 1218 (2018).

[23] H. H. Kim, B. Yang, S. Tian, C. Li, G.-X. Miao, H. Lei, and A. W. Tsen, *Tailored tunnel magnetoresistance response in three ultrathin chromium trihalides*, Nano letters **19**, 5739 (2019).

[24] D. C. Johnston, *Magnetic dipole interactions in crystals*, Physical Review B **93**, 014421 (2016).

[25] H. H. Kim *et al.*, *Evolution of interlayer and intralayer magnetism in three atomically thin chromium trihalides*, Proceedings of the National Academy of Sciences **116**, 11131 (2019).

[26] L. Chen, J.-H. Chung, B. Gao, T. Chen, M. B. Stone, A. I. Kolesnikov, Q. Huang, and P. Dai, *Topological spin excitations in honeycomb ferromagnet CrI_3*, Physical Review X **8**, 041028 (2018).

Chapter 7 Summary and Outlook

In summary we studied two types of quantum magnets, the SOC bilayer perovskite iridate $Sr_3Ir_2O_7$ and the 2D magnets CrX_3 (X = Cl, Br, I).

In $Sr_3Ir_2O_7$, we found that despite its novel SOC pseudospin moments, its interlayer coupling falls into the weak coupling regime so that its magnetic excitation can be well-described by the conventional spin wave theory rather than the dimer excitation. We reproduced both the puzzling A_{1g} magnetic excitation at 800 cm^{-1} together with the higher-energy two-magnon scattering at 1400 cm^{-1} in Raman data [1] with a unified theory of two-magnon scattering [2], which sheds light on the previous debate on the nature of the magnetic excitations in RIXS [3-6]. We revealed that the magnetism of $Sr_3Ir_2O_7$ is analogue to its single-layer counterpart Sr_2IrO_4 with comparable exchange energy scale [7].

As a follow-up of this work, we are also interested in studying the two-magnon Raman scattering in perovskite iridates with time-resolved Raman spectroscopy, which is under development in our lab. From the scientific point of view, ultrashort pulses are capable of inducing novel phenomena in materials, including MIT [8-10], superconductivity [11], and magnetic order [12]. A previous time-resolved Raman study on the two-magnon scattering in $KNiF_3$ has demonstrated optically induced modifications of its exchange energies [13]. The question thus arises whether optical pumping can induce novel magnetism in perovskite iridates. From the technical point of view,

time-resolved Raman spectroscopy is limited to probing excitations with a large linewidth, because the ultrashort probe pulse has a much larger linewidth compared to the CW pulses in conventional Raman spectroscopy. Two-magnon scatterings (FWHM ~100 cm^{-1}) in perovskite iridates are much broader than its phonon excitations (FWHM ~5 cm^{-1}), thus allowing for simple measurement with time-resolved Raman spectroscopy.

In CrX_3 (X = Cl, Br, I), we studied the X-evolution of various spin parameters including the anisotropy and exchange energies, using spin wave calculations to fit field-dependent electron tunneling data [14]. We found that the CrX_3 family displays increasing exchange energy with increasing X atom number, and that their magnetic GS evolve from in-plane moments in $CrCl_3$ to out-of-plane moments in $CrBr_3$ and CrI_3. Albeit their minor magnetic anisotropy (α is close to 1), their magnetic order can be stabilized down to the monolayer limit.

In a more focused field-dependent polarized Raman study on CrI_3, we uncovered the coexistence of SAFM and BFM in bulk CrI_3 which was thought to be entirely FM [15]. This result offers a natural explanation to the puzzling layer-dependent magnetism in CrI_3 from bulk FM to few-layer AFM [16-20]. We also found that below T_C = 45 K, external magnetic field induces a magnetic phase transition from AFM to FM concurrent with a structural phase transition from rhombohedral C_{3i} to monoclinic C_{2h} at B_C = 2 T. We were thus able to construct the phase diagram of bulk CrI_3.

My colleagues at the University of Michigan have further conducted extensive Raman studies on few-layer CrI_3, which are shown to remain in the monoclinic structure despite its magnetism [21]. The field-induced AFM to FM phase transition is accompanied by enhanced monoclinic distortion,

similar to bulk CrI_3 [21]. Raman technique have also unveiled a plethora of novel phenomena including magnetic phonons [22] and excitons [23].

References

[1] H. Gretarsson, N. Sung, M. Höppner, B. Kim, B. Keimer, and M. Le Tacon, *Two-magnon Raman scattering and pseudospin-lattice interactions in Sr_2IrO_4 and $Sr_3Ir_2O_7$*, Physical review letters **116**, 136401 (2016).

[2] S. Li *et al.*, *Symmetry-resolved two-magnon excitations in a strong spin-orbit-coupled bilayer antiferromagnet*, Physical Review Letters **125**, 087202 (2020).

[3] M. M. Sala *et al.*, *Evidence of quantum dimer excitations in $Sr_3Ir_2O_7$*, Physical Review B **92**, 024405 (2015).

[4] J. Kim *et al.*, *Large spin-wave energy gap in the bilayer iridate $Sr_3Ir_2O_7$: Evidence for enhanced dipolar interactions near the mott metal-insulator transition*, Physical review letters **109**, 157402 (2012).

[5] X. Lu, D. McNally, M. M. Sala, J. Terzic, M. Upton, D. Casa, G. Ingold, G. Cao, and T. Schmitt, *Doping Evolution of Magnetic Order and Magnetic Excitations in $(Sr_{1-x}La_x)_3Ir_2O_7$*, Physical review letters **118**, 027202 (2017).

[6] T. Hogan, R. Dally, M. Upton, J. Clancy, K. Finkelstein, Y.-J. Kim, M. Graf, and S. D. Wilson, *Disordered dimer state in electron-doped $Sr_3Ir_2O_7$*, Physical Review B **94**, 100401 (2016).

[7] J. Kim *et al.*, *Magnetic excitation spectra of Sr_2IrO_4 probed by resonant inelastic X-ray scattering: establishing links to cuprate superconductors*, Physical Review Letters **108**, 177003 (2012).

[8] M. Rini, N. Dean, J. Itatani, Y. Tomioka, Y. Tokura, R. W. Schoenlein, and A. Cavalleri, *Control of the electronic phase of a manganite by mode-selective vibrational excitation*, Nature **449**, 72 (2007).

[9] H. Ichikawa *et al.*, *Transient photoinduced 'hidden'phase in a manganite*, Nature materials **10**, 101 (2011).

[10] S. De Jong *et al.*, *Speed limit of the insulator–metal transition in magnetite*, Nature materials **12**, 882 (2013).

[11] D. Fausti *et al.*, *Light-induced superconductivity in a stripe-ordered cuprate*, science **331**, 189 (2011).

[12] A. Kirilyuk, A. V. Kimel, and T. Rasing, *Ultrafast optical manipulation of magnetic order*, Reviews of Modern Physics **82**, 2731 (2010).

[13] G. Batignani, D. Bossini, N. Di Palo, C. Ferrante, E. Pontecorvo, G. Cerullo, A. Kimel, and T. Scopigno, *Probing ultrafast photo-induced dynamics of the exchange energy in a Heisenberg antiferromagnet*, Nature Photonics **9**, 506 (2015).

[14] H. H. Kim *et al.*, *Evolution of interlayer and intralayer magnetism in three atomically thin chromium trihalides*, Proceedings of the National Academy of Sciences **116**, 11131 (2019).

[15] S. Li *et al.*, *Magnetic-field-induced quantum phase transitions in a van der Waals magnet*, Physical Review X **10**, 011075 (2020).

[16] B. Huang *et al.*, *Layer-dependent ferromagnetism in a van der Waals crystal down to the monolayer limit*, Nature **546**, 270 (2017).

[17] M. A. McGuire, H. Dixit, V. R. Cooper, and B. C. Sales, *Coupling of crystal structure and magnetism in the layered, ferromagnetic insulator CrI3*, Chemistry of Materials **27**, 612 (2015).

[18] J. Dillon Jr and C. Olson, *Magnetization, resonance, and optical properties of the ferromagnet* CrI_3, Journal of Applied Physics **36**, 1259 (1965).

[19] D. R. Klein *et al.*, *Probing magnetism in 2D van der Waals crystalline insulators via electron tunneling*, Science **360**, 1218 (2018).

[20] T. Song *et al.*, *Giant tunneling magnetoresistance in spin-filter van der Waals heterostructures*, Science **360**, 1214 (2018).

[21] X. Guo *et al.*, *Structural Monoclinicity and Its Coupling to Layered Magnetism in Few-Layer* CrI_3, ACS nano (2021).

[22] W. Jin *et al.*, *Tunable layered-magnetism–assisted magneto-Raman effect in a two-dimensional magnet* CrI_3, Proceedings of the National Academy of Sciences **117**, 24664 (2020).

[23] W. Jin *et al.*, *Observation of the polaronic character of excitons in a two-dimensional semiconducting magnet* CrI_3, Nature communications **11**, 1 (2020).